

**STUDY OF AN UNDEREXPANDED ANNULAR WALL JET
PAST AN AXISYMMETRIC BACKWARD-FACING STEP**

by
Pedro Iván Espina

Dissertation submitted to the Faculty of the Graduate School of the
University of Maryland at College Park in partial fulfillment
of the requirements for the degree of
Doctor of Philosophy
1997

Advisory Committee:

Associate Professor Ugo Piomelli, Chairman/Advisor
Professor John D. Anderson
Professor James H. Duncan
Assistant Professor Ken Kiger
Professor James M. Wallace
Dr. George E. Mattingly

Abstract

Title of Dissertation: Study of an Underexpanded Annular Wall Jet
Past an Axisymmetric Backward-Facing Step

Name of degree candidate: Pedro Ivan Espina

Degree and Year: Doctor of Philosophy, 1997

Dissertation directed by: Dr. Ugo Piomelli
Associate Professor
Department of Mechanical Engineering

Gas-metal atomization is a process by which liquid metal is transformed into a metal powder. The metal powders produced through gas-metal atomization exhibit chemical homogeneity and refined microstructures that cannot be obtained by conventional casting techniques. Given their enhanced properties, the products made from these powders find applications ranging from jet-engine parts to medical implants.

The heart of a gas-metal atomizer is a device known as the “atomization nozzle assembly”, which forces the interaction between a high-speed gas jet and a liquid stream of molten metal. Because the control of a molten stream of metal can be difficult, atomization control strategies have historically been focused on the gas-delivery-system of the atomizers. Thus, in this investigation, the gas-only flow in a close-coupled, gas-metal atomizer is studied to determine the influence of operational parameters on the structure of the flow field.

Both experimental and numerical results are presented. First, the numerical method used is evaluated by modeling flat-plate boundary layers at various free

stream velocities; further validation is conducted by modeling an axisymmetric base flow for which experimental and numerical data are available for comparison. Comparisons between the Schlieren images produced experimentally and numerical results are carried out, focusing on the evaluation of turbulence model parameters.

The same methodology was then used to model the gas-only atomization flow produced at conventional operational conditions. A parametric study was conducted to determine the effects of jet exit pressure ratio, jet temperature ratio, and base mass injection (to model, at least approximately, some of the effects of the liquid phase).

Based on the results obtained in the validation stage, it is concluded that the Chien k - ϵ turbulence model yields excessively high production of turbulence kinetic energy dissipation rate in this type of flow. It is shown that a 10% reduction in the production of dissipation rate leads to good agreement with the experimental data. Results from the pressure ratio study led to a description of the observed base pressure behavior (*i.e.*, aspiration) on the basis of the resulting jet structure. The temperature ratio results hinted that the common industrial practice of gas-heating may be detrimental to the atomization process due to a global reduction in the momentum of the gas flow field. The flow fields obtained with base mass injection (brought through the liquid metal conduit), exhibited base flow structures similar in shape to those seen in high-speed studies of the liquid metal disruption process. It is shown that the introduction of mass at the base of the flow has little impact on the flow structure of the surrounding gas flow field. It is concluded that, with some experimental verification, parameterization studies such as this can be a very cost-effective way to optimize this industrial process.

Dedication

To the Memory of Prof. D. W. Sallet

Acknowledgments

I would like to express my deepest appreciation to my advisor Prof. Ugo Piomelli for his guidance and his insurmountable patience throughout the course of this work.

Thanks are also due to Dr. George E. Mattingly for sharing his love of fluid mechanics with me; his support during the bad times and his joy during the good times was given with a paternal spirit for which I will always be indebted to him. I would also like to thank professors John D. Anderson, James H. Duncan, Ken Kiger, and James M. Wallace for serving on my Advisory Committee, and Dr. Gregory J. Rosasco and Dr. Hratch G. Semerjian for supporting this work.

I am also indebted to friends and colleagues. In particular, I wish to thank Francis S. Biancaniello, Paul A. Boyer, Dr. Stephen A. Osella, Robert L. Parke, and Dr. Stephen D. Ridder of NIST for their collaboration on the atomization project; C. Jenny Mu of Johns Hopkins University for the careful editing of this document; James M. Allingham, Dr. Vern E. Bean, Aaron N. Johnson, John F. Houser, John D. Wright, and Dr. T. T. Yeh of NIST for the everyday exchange of ideas; Drs. G. K. Copper and Greg D. Power of Sverdrup Technology, Inc., Carol B. Davies of Sterling Software, and Mr. Denis A. Lehane of the High Performance Systems and Services Division of NIST for their technical collaborations without which this work would not have reached this point at this time; Dr. Elias Balaras, Peter Chang, Dr. Alan Folz, Dr. Xiaoli Huai, Chandrasekhar Kannepalli, Dr. Junhui Liu, Dr. Luca Massasso, Biren M. Mowli, Joseph Murray, Jim Thomas, and Dr. Fabrizio Sarghini for their friendship and help which made my experience at the University of Maryland a enjoyable one. Finally, enlightening discussions with Dr. Jeff L. Herrin of NASA-Langley, Nicholas J. Georgiadis of NASA-Lewis, and John

J. Conway and William B. Eisen of Crucible Metals are gratefully acknowledged.

Last, but certainly not least, I would like to thank my wife, Monika Hirschbichler, my parents, and Eduardo for their enormous support and understanding. Without their love and encouragement, finishing this work would have been all but impossible.

Financial support for this research was provided by the Process Measurements Division of the Chemical Science and Technology Laboratory of NIST. Computer resources were supplied by the NIST High Performance Systems and Service Division.

Table of Contents

List of Tables	vii
List of Figures	viii
1 Introduction	1
1.1 Overview of gas-metal atomization	1
1.2 Previous investigations	6
1.3 Objectives of the present study	12
2 Mathematical Formulation	14
2.1 Governing equations	14
2.2 Turbulence models	17
2.2.1 Baldwin-Lomax model	17
2.2.2 Chien k - ϵ model	19
2.2.3 Grasso-Falconi k - ϵ model	21
2.3 Numerical method	25
2.3.1 Solution of the governing equations	25
2.3.2 Solution of the turbulence equations	32
2.3.3 Grid adaptation algorithm	34
3 Evaluation of Turbulence Models	37
3.1 Physical domain and boundary conditions	37
3.2 Subsonic boundary-layer	39

3.3	Supersonic boundary-layer	47
3.4	Summary	50
4	Supersonic Base Flow	52
4.1	Physical domain and boundary conditions	55
4.2	The nozzle flow	57
4.3	Effects of turbulence modeling	60
4.4	Effects of pressure ratio	68
4.5	Summary	74
5	Close-Coupled, Gas-Metal Atomizer Gas-Only Flow	76
5.1	Physical domain and boundary conditions	78
5.2	Effects of turbulence dissipation production	82
5.3	Effects of jet pressure ratio	88
5.4	Effects of jet temperature ratio	98
5.5	Effects of base mass injection	102
5.6	Summary	105
6	Conclusions	109
	Bibliography	114

List of Tables

I	Parameter ranges used during the operation of the gas-metal atom- izer in Figure 5.1.	78
---	--	----

List of Figures

1.1	Process of gas-metal atomization. The downward flowing black stream is liquid metal which has been disrupted by high energy gas jets surrounding it.	2
1.2	Schematic of a typical gas-metal atomizer.	4
1.3	Types of atomization nozzle assemblies.	5
2.1	Schematic comparison between an elliptic, four-spring and a parabolic, three-spring grid adaptation method.	36
3.1	Computational domain used for the simulation of the boundary-layer (vertical axis not shown to scale; $L = 0.5\ m$).	38
3.2	Computational meshes used for the simulation of the boundary-layer. TOP: for $M_{inf} = 0.2$; BOTTOM: for $M_{inf} = 1.2$ and 4.0 (vertical scale shown at four times its original size).	38
3.3	Effect of turbulence model on the streamwise velocity distribution of a boundary layer, $R_\theta = 1410$, $M_{inf} = 0.2$. — : law of the wall, equation (3.2.1); \circ : Spalart's DNS (1988); --- : Baldwin-Lomax model; -·-· : Chien's k - ϵ model; ····· : Grasso-Falconi's k - ϵ model. .	40

3.4 Effect of turbulence model on the eddy-viscosity distribution of a boundary layer, $R_\theta = 1410$, $M_{\text{inf}} = 0.2$. \circ : Spalart's DNS (1988), $\nu_t = \overline{u'v'}/d\bar{u}/dy$; --- : Baldwin-Lomax model; - - - : Chien's k - ϵ model; \cdots : Grasso-Falconi's k - ϵ model. 41

3.5 Effect of turbulence model on the turbulent kinetic energy distribution of a boundary layer, $R_\theta = 1410$, $M_{\text{inf}} = 0.2$. \circ : Spalart's DNS (1988); - - - : Chien's k - ϵ model; \cdots : Grasso-Falconi's k - ϵ model. . . 42

3.6 Effect of turbulence model on the near-wall turbulent kinetic energy dissipation rate distribution of a boundary layer, $R_\theta = 1410$, $M_{\text{inf}} = 0.2$. \circ : Spalart's DNS (1988); - - - : Chien's k - ϵ model (ϵ only); — : Chien's k - ϵ model ($\epsilon + D$); \cdots : Grasso-Falconi's k - ϵ model. . . . 43

3.7 Performance of the Chien k - ϵ model near-wall of a boundary layer, $R_\theta = 1410$, $M_{\text{inf}} = 0.2$. TOP LEFT, turbulent kinetic energy distribution (square power), \circ : Spalart's DNS (1988); — : Chien's k - ϵ model. TOP RIGHT, distribution of turbulent kinetic energy dissipation rate, \circ : Spalart's DNS (1988); — : Chien's k - ϵ model. BOTTOM CENTER, eddy-viscosity distribution, \circ : Spalart's DNS (1988), $\nu_t = \overline{u'v'}/d\bar{u}/dy$; + : Spalart's DNS (1988), $\nu_t = C_\mu f_\mu k^2/\epsilon$; — : Chien's k - ϵ model. 44

3.8 Effect of turbulence model on the streamwise velocity distribution of a boundary layer, $R_\theta = 14000$; LEFT: $M_{\text{inf}} = 1.2$; RIGHT: $M_{\text{inf}} = 4.0$. — : law of the wall; --- : Baldwin-Lomax model; - - - : Chien's k - ϵ model; \cdots : Grasso-Falconi's k - ϵ model. 47

3.9 Effect of turbulence model on the eddy-viscosity distribution of a boundary layer, $R_\theta = 14000$; LEFT: $M_{\text{inf}} = 1.2$; RIGHT: $M_{\text{inf}} = 4.0$. --- : Baldwin-Lomax model; - - - : Chien's k - ϵ model; \cdots : Grasso-Falconi's k - ϵ model. 48

3.10	Effect of turbulence model on the turbulent kinetic energy distribution of a boundary layer, $R_\theta = 14000$; LEFT: $M_{\text{inf}} = 1.2$; RIGHT: $M_{\text{inf}} = 4.0$. - - - : Chien's $k-\epsilon$ model; \cdots : Grasso-Falconi's $k-\epsilon$ model.	49
3.11	Effect of turbulence model on the near-wall turbulent kinetic energy dissipation rate distribution of a boundary layer, $R_\theta = 14000$; LEFT: $M_{\text{inf}} = 1.2$; RIGHT: $M_{\text{inf}} = 4.0$. - - - : Chien's $k-\epsilon$ model (ϵ only); — : Chien's $k-\epsilon$ model ($\epsilon + D$); \cdots : Grasso-Falconi's $k-\epsilon$ model.	50
4.1	Schematic of the axisymmetric base flow produced by the flow of a supersonic annular jet over the end of a circular cylinder (labeled Base in the figure).	53
4.2	Schematic diagram of the computational domain used in the base flow problem.	56
4.3	Computational mesh adapted for simulation of base flow at the design pressure ratio (only every fourth grid line is shown for clarity).	57
4.4	Annular nozzle profiles near the end-corner of the circular cylinder. (Top) streamwise velocity distribution, — : present work; - - - : law of the wall; \circ : Herrin and Dutton's data; + : corrected Herrin and Dutton's data. (Bottom) turbulent kinetic energy distribution.	58
4.5	Base pressure distribution. — : Chien's $k-\epsilon$; \cdots : Chien's $k-\epsilon$, (high resolution); - - - : original Baldwin-Lomax ; + : Sahu; \times : Tucker and Shyy; \circ : Herrin and Dutton.	61
4.6	Mach number distribution in the wake of the circular cylinder. (Top half) original Baldwin-Lomax model. (Bottom half) Chien's $k-\epsilon$ model.	63

4.7	Mean axial velocity distribution in the test section ($u_e = 569 \text{ m/s}$). — : Chien's $k-\epsilon$; : Chien's $k-\epsilon$, (high resolution); --- : original Baldwin-Lomax; o : Herrin and Dutton.	64
4.8	Effect of the reduction in turbulence dissipation production on the mean axial velocity distribution in the test section ($u_e = 569 \text{ m/s}$). — : Chien's $k-\epsilon$ model, $C_{\epsilon 1} = 1.35$ (original); -.- : Chien's $k-\epsilon$ model, $C_{\epsilon 1} = 1.215$ (10% reduction in the production of ϵ); o : Herrin and Dutton.	66
4.9	Effect of the reduction in turbulence dissipation production on the base pressure distribution. — : Chien's $k-\epsilon$ model, $C_{\epsilon 1} = 1.35$ (original model); -.- : Chien's $k-\epsilon$ model, $C_{\epsilon 1} = 1.215$ (10% reduction in the production of ϵ); + : Sahu; \times : Tucker and Shyy; o : Herrin and Dutton.	67
4.10	Effect of the reduction in turbulence dissipation production on the Mach number distribution in the wake of the circular cylinder. [Top half] Chien's $k-\epsilon$ model, $C_{\epsilon 1} = 1.215$ (10% reduction in the production of ϵ); [Bottom half] Chien's $k-\epsilon$ model, $C_{\epsilon 1} = 1.35$ (original model).	68
4.11	Effect of jet pressure ratio on base pressure distribution. -.- : Overexpanded, $P_e/P_r = 0.96$; — : Design, $P_e/P_r = 1.01$; --- : Underexpanded, $P_e/P_r = 1.07$	69
4.12	Effect of jet pressure ratio on pressure (P/P_o , upper halves) and Mach number (lower halves) distributions in the wake of the circular cylinder. (Top) overexpanded, $P_e/P_r = 0.96$; (Center) design, $P_e/P_r = 1.01$; (Bottom) underexpanded, $P_e/P_r = 1.07$	71

4.13	Density distribution in the wake of a circular cylinder at design pressure ratio (ρ/ρ_{ref} , $\rho_{ref} = 1.293 \text{ kg/m}^3$).	72
4.14	Effect of jet pressure ratio on mean axial velocity distribution in the test section ($u_e = 569 \text{ m/s}$). -·-· : Overexpanded, $P_e/P_r = 0.96$; — : Design, $P_e/P_r = 1.01$; - - - : Underexpanded, $P_e/P_r = 1.07$. . .	73
5.1	Schematic diagram of annular jet, close-coupled atomization nozzle assembly studied in this investigation (geometry rotated 90° ccw from its normal operational orientation).	77
5.2	Schlieren image of the gas-only flow in a close-coupled gas-metal atomizer operating at baseline settings (flow from left to right). . .	79
5.3	Schematic diagram of the computational domain used to model the gas-only flow in a close-coupled atomizer.	80
5.4	Typical computational mesh adapted for simulation of gas-only flow in a close-coupled gas-metal atomizer (only every fourth grid line is shown for clarity).	81
5.5	Detail of the base region of the computational mesh (only every fourth grid line is shown for clarity).	81
5.6	Schlieren image of the gas-only flow (base region detail) produced by the selected close-coupled atomization nozzle assembly when operated at baseline settings. Mesh with unit element R^2 , superimposed for dimensional reference.	83
5.7	Effect of the turbulence dissipation production level on the density distribution of the gas-only atomization flow (baseline settings): $\rho^* = \rho/\rho_r$, $\rho_r = 1.66 \text{ kg/m}^3$; $\Delta\rho^* = 0.5$. Top: original Chien's $k-\epsilon$ model ($C_{\epsilon 1} = 1.35$); Center: 10% global reduction in \mathcal{P}_ϵ ($C_{\epsilon 1} = 1.215$); Bottom: 20% global reduction in \mathcal{P}_ϵ ($C_{\epsilon 1} = 1.08$).	84

5.8 Effect of turbulence dissipation production level on axial Mach number distribution of the gas-only atomization flow (baseline settings).
— : original Chien’s k - ϵ model ($C_{\epsilon 1} = 1.35$); --- : 10% global reduction in \mathcal{P}_ϵ ($C_{\epsilon 1} = 1.215$); -·-· : 20% global reduction in \mathcal{P}_ϵ ($C_{\epsilon 1} = 1.08$). 86

5.9 Effect of turbulence dissipation production level on base pressure distribution of the gas-only atomization flow (baseline settings).
— : original Chien’s k - ϵ model ($C_{\epsilon 1} = 1.35$); --- : 10% global reduction in \mathcal{P}_ϵ ($C_{\epsilon 1} = 1.215$); -·-· : 20% global reduction in \mathcal{P}_ϵ ($C_{\epsilon 1} = 1.08$); ■ : experimental data (averaged value only), $P_{r_{exp}} = 98.574 \text{ kPa}$ 87

5.10 Effect of jet pressure ratio, P_e/P_r , on aspiration pressure, P_{dt}/P_r , for the selected close-coupled atomization nozzle assembly (baseline settings except as noted). \ominus : experimental data, $P_{r_{exp}} = 98.574 \text{ kPa}$; \times : numerical results. 89

5.11 Effects of jet pressure ratio on the topology of gas-only atomization flows (baseline settings except as noted): experimental Schlieren pictures (upper images), numerical density distributions (lower images). TOP LEFT: $P_e/P_r \simeq 6.6$; BOTTOM LEFT: $P_e/P_r \simeq 20$; TOP RIGHT: $P_e/P_r \simeq 33$; BOTTOM RIGHT: $P_e/P_r \simeq 46$ 91

5.12 Effects of jet pressure ratio on the axisymmetric stream function distribution of gas-only atomization flows (baseline settings except as noted): $\psi^* = \psi/(\rho_r a_r R)$, $a_r = 319 \text{ m/s}$, $\Delta\psi^* = 0.2$ (upper images), $\Delta\psi^* = 0.005$ (lower images). TOP LEFT: $P_e/P_r \simeq 6.6$; BOTTOM LEFT: $P_e/P_r \simeq 20$; TOP RIGHT: $P_e/P_r \simeq 33$; BOTTOM RIGHT: $P_e/P_r \simeq 46$ 92

5.13 Effects of jet pressure ratio on static pressure and Mach number distributions of gas-only atomization flows (baseline settings except as noted): $P^* = P/P_r$, $\Delta P^* = 0.2$ (upper images), $\Delta M = 0.5$ (lower images). TOP LEFT: $P_e/P_r \simeq 6.6$; BOTTOM LEFT: $P_e/P_r \simeq 20$; TOP RIGHT: $P_e/P_r \simeq 33$; BOTTOM RIGHT: $P_e/P_r \simeq 46$ 93

5.14 Effect of jet pressure ratio on flow separation over the liquid-delivery tube (baseline settings except as noted): $C_f = 2\tau_w/\rho_r a_r^2$: $P_e/P_r \simeq 6.6$; - · - · : $P_e/P_r \simeq 20$; — : $P_e/P_r \simeq 33$; - - - : $P_e/P_r \simeq 46$. 96

5.15 Schematic diagram of the separation phenomenon at the end of the liquid-delivery tube. 97

5.16 Effects of jet temperature ratio on the density distribution of gas-only atomization flows (baseline settings except as noted): $\Delta\rho^* = 0.5$. TOP: $T_e/T_r = 0.65$; BOTTOM: $T_e/T_r = 1.31$ 99

5.17 Effects of jet temperature ratio on the axisymmetric stream function distribution of gas-only atomization flows (baseline settings except as noted): $\Delta\psi^* = 0.2$ (upper images), $\Delta\psi^* = 0.005$ (lower images). LEFT: $T_e/T_r = 0.65$; RIGHT: $T_e/T_r = 1.31$ 100

5.18 Effect of jet temperature ratio on flow separation over the liquid-delivery tube (baseline settings except as noted): $C_f = 2\tau_w/\rho_r a_r^2$. — : $T_e/T_r = 0.65$; - - - : $T_e/T_r = 1.31$ 101

5.19 Effect of jet temperature ratio on the liquid-delivery tube surface temperature (baseline settings except as noted). — : $T_e/T_r = 0.65$; - - - : $T_e/T_r = 1.31$ 102

5.20 Effects of liquid-delivery tube mass injection on the axisymmetric stream function distribution of gas-only atomization flows (baseline settings except as noted): $\Delta\psi^* = 0.2$ (left images), $\Delta\psi^* = 0.005$ (right images). TOP: $\dot{m}_{dt}/\dot{m}_{jet} = 0$; CENTER: $\dot{m}_{dt}/\dot{m}_{jet} = 0.13\%$; BOTTOM: $\dot{m}_{dt}/\dot{m}_{jet} = 0.41\%$ 104

Chapter 1

Introduction

1.1 Overview of gas-metal atomization

Gas-Metal Atomization (GMA) is a process by which liquid metal is transformed into metal powder. The metal powders produced by GMA exhibit chemical homogeneity and refined microstructure that cannot be obtained by conventional casting techniques. Given their enhanced properties, the products made from these powders find applications ranging from jet engine parts to medical implants (Lawley 1985). The annual production of gas atomized metal powders in America for 1996 is estimated to be valued at 75 million dollars; this level of production and the low yields associated with powder metallurgy processes makes them prime candidates for process optimization.

Typically, the GMA process (see Figure 1.1) starts with a stream of molten metal that is forced to interact with high speed gas jets. During this interaction, momentum is transferred from the gas jets to the liquid stream. The momentum transfer increases the velocity of the liquid metal stream and eventually makes it unstable. The instabilities in the liquid stream promote the formation of liquid ligaments

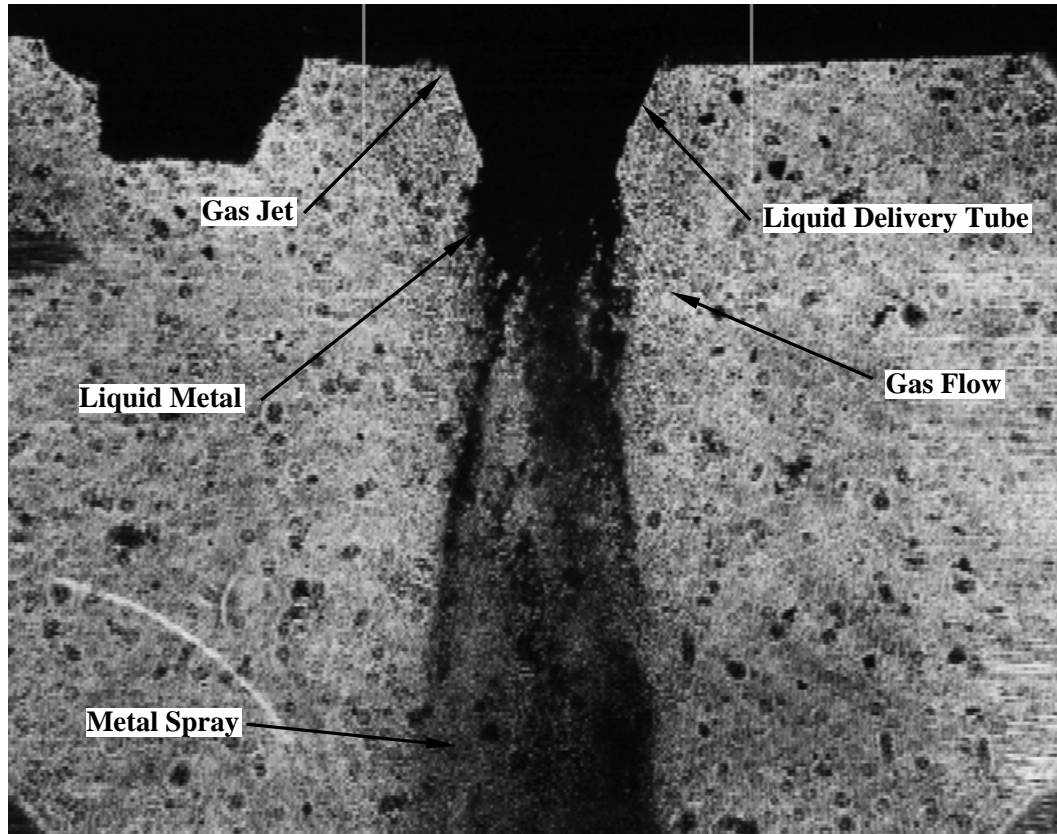


Figure 1.1: Process of gas-metal atomization. The downward flowing black stream is liquid metal which has been disrupted by high energy gas jets surrounding it.

that then break into liquid droplets. If the droplets are too big to be stable, they break into smaller droplets; otherwise, they solidify in flight and are collected at the end of the process as metal powder.

GMA is one of a number of processes commonly referred to as **powder metallurgy** processes. Two other processes contained in this group are **metal spray deposition** and **metal spray forming**. Their common denominator is the formation of liquid metal droplets by atomization. As mentioned before, in GMA the droplets are allowed to solidify in flight and are then collected as metal powder. In spray deposition, the liquid droplets are sprayed onto a substrate until the buildup creates a billet. For spray forming, a preform, in the shape of the part desired, is sprayed upon until enough metal is accumulated to create the required product.

Alternatively, metal spray can be sprayed onto a substrate and allowed to build up until an ingot-like shaped billet is formed.

The powder produced by GMA needs to undergo a stage of near net-shape forming in which a powder cake of the desired part is formed with the help of a bonding agent. Alternatively, the powder can be deposited in a near net-shape container in preparation for consolidation by hot isostatic pressing. Analogously, in spray deposition, the shape of the desired part is machined from the billet previously made. For spray forming, no such shape forming process is required. All three processes may require a densification stage for the product to obtain its final working strength and, once the densification stage is completed, final machining is performed to obtain desired dimensional tolerances.

The machine in which the metal atomization process takes place is known as a **gas-metal atomizer** or simply as an **atomizer**. Typically, atomizers (Figure 1.2) contain a melting furnace, an atomization chamber, and a gas-powder separation stage. The heart of the atomizer is the structure that forces the interaction between the metal stream and the gas jets. This structure, which is located in the atomization chamber, is known as the **atomization nozzle assembly**, or **atomization die**.

Atomization dies can be of two types: **free-fall**, or **close-coupled**. In free-fall atomizers (Figure 1.3 – left) the liquid metal stream is allowed to fall, unconstrained, until it interacts with the gas jets. Conversely, in close-coupled atomizers (Figure 1.3 – right) the liquid stream remains confined by a ceramic **liquid-delivery tube** at the end of which the interaction between the liquid and the gas jets takes place.

Conceptually, the operation of free-fall atomizers is simpler than that of close-

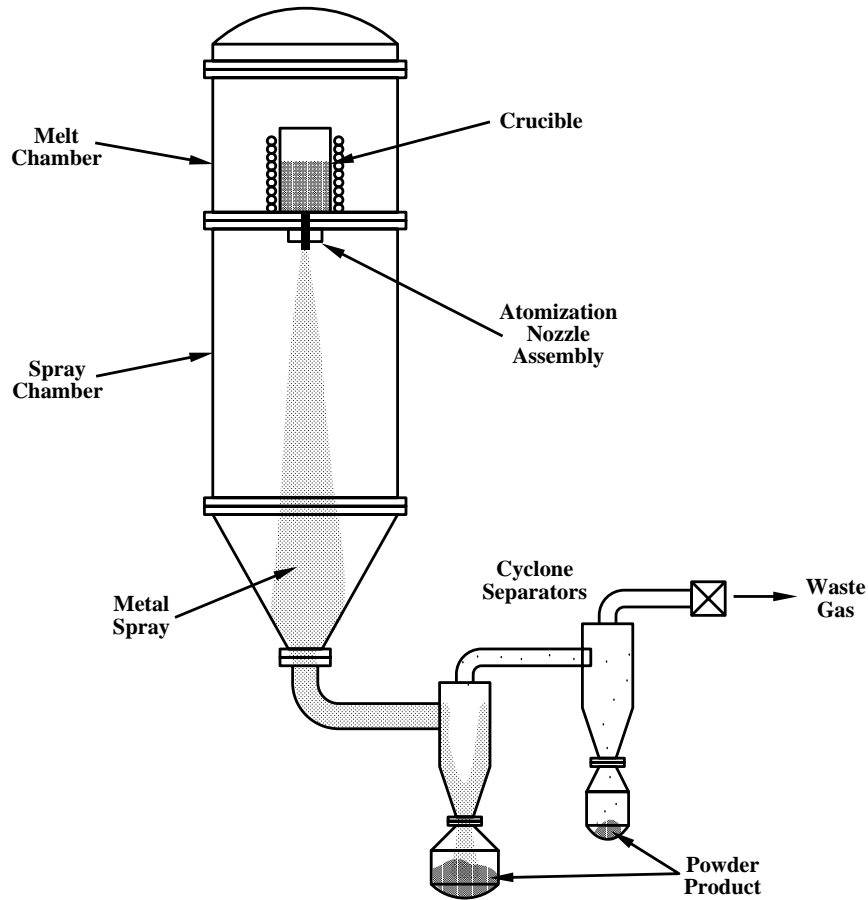
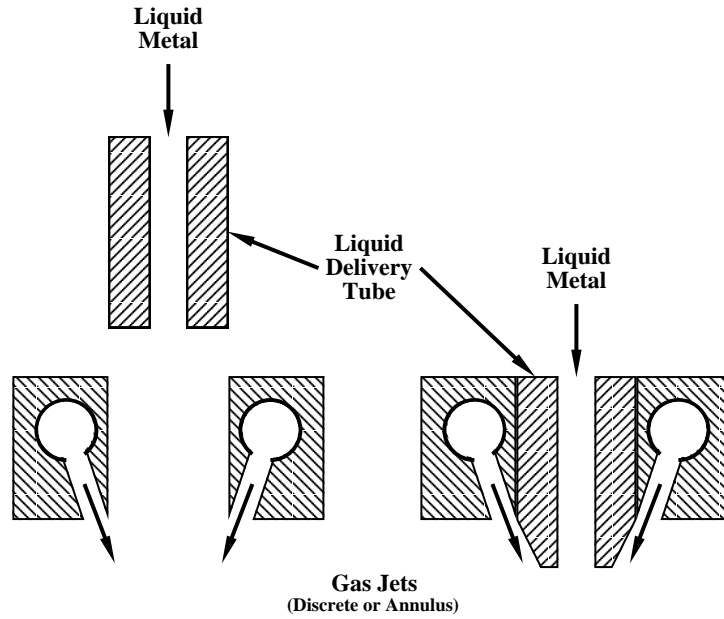


Figure 1.2: Schematic of a typical gas-metal atomizer.

coupled atomizers and traditionally, this has led to the prevalent usage of free-fall atomizers by industry. However, the properties of metal powders have been shown to be closely related to particle size; the finer the particles, the better their properties tend to be (Boettinger and Bendersky 1986). This tendency benefits close-coupled atomizers, which are known to produce smaller droplets than free-fall atomizers (Beddow 1978); in turn, this has spawned a significant industrial interest in the use of closed-coupled atomizers during the last decade.

Traditionally, the design of atomizers has been *ad hoc*, mostly due to a deficiency in design objectives and criteria (Beddow 1978). This practice has proven to be particularly problematic with close-coupled atomizers, whose operation is highly



Free-Fall **Close-Coupled**
 Figure 1.3: Types of atomization nozzle assemblies.

sensitive to geometrical details and operational conditions (Ayers and Anderson 1985; Ridder and Biancaniello 1988). Moreover, the lack of agreement between users on what constitutes “good” metal powder product, makes the design of close-coupled atomizers all the more difficult.

The objective of this investigation is to study a number of geometrical arrangements and operational conditions that influence the performance of close-coupled atomizers. It is the intended goal that the results obtained can help in the development of guidelines and specifications for the design and operation of gas-metal atomizers.

The next section of this chapter presents a review of the previous investigations conducted in the area of flow modeling of close-coupled gas metal atomization. This is followed by the last section of this chapter, in which the objectives of this investigation are expanded and suggestions are given for the potential benefits of

these results in improving industrial powder metallurgy.

1.2 Previous investigations

Experimental evidence presented by Couper and Singer (1985) suggested that the disruption efficiency in close-coupled gas atomization is directly related to the low pressure region created at the exit of the liquid-delivery tube by the overflow of the gas jet. They determined that the local pressure at the exit of the liquid-delivery tube is a function of the gas jet stagnation pressure. Following the work of Couper and Singer (1985), Ayers and Anderson (1985) reported evidence of a direct relationship between gas jet stagnation pressure and particle size distribution using close-coupled atomization nozzle assemblies. They found that the finest powder was produced when the stagnation pressure was set at the value that yielded the minimum static pressure at the exit of the liquid-delivery tube. Ayers and Anderson (1985) also studied the dependence of this pressure at the end of the liquid-delivery tube (which they named **aspiration**) with respect to jet stagnation pressure, gas specie, and liquid-delivery tube geometry. In a similar investigation, Ting and Grant (1986) studied the dependence of the aspiration pressure with respect to the liquid-delivery tube extension and investigated the atomization of 7075 aluminum alloy while varying a number of process parameters. Ridder and Biancaniello (1988) also studied the aspiration phenomena and proposed a particle-size control scheme based on it.

The studies described previously established the foundation for the characterization of close-coupled atomization nozzle assemblies. In the following years the focus of the gas-metal atomization research switched to the development of predictive models based on the study of the fluid mechanics controlling the process.

Espina *et al.* (1989) made use of the two-dimensional, region-to-region method-of-characteristics (John 1984) to describe the gas flow over the liquid-delivery tube. These calculations, although only approximate due to the two-dimensional approximation of an axisymmetric flow field, led to a model for the aspiration pressure as a function of the location of the end-corner of the liquid-delivery tube with respect to the shape of the first shock structure in the underexpanded wall jet. Independently, Ünal (1989) studied the use of annular underexpanded jets in close-coupled gas metal atomization and made use of two-dimensional wave theory to describe the structures seen in Schlieren images. He also proposed a model for the aspiration pressure based on the location of the liquid-delivery tube end with respect to the structure of the initial gas wall jet.

In the same year, Anderson *et al.* (1989), made use of analogy between the Froude number (in open channel flow) and the Mach number (in compressible flow) to study the structure of the gas jet for various close-coupled atomizer geometries. Their quantitative results were erroneous due to the lack of validity of the Froude-Mach number analogy for specific heat ratios, γ , other than 2, and because of the difference between the two-dimensional and the axisymmetric wave phenomena. However, their qualitative results led them to recognize the similarities between the gas-only flow in close-coupled gas-metal atomizer and the flow in axisymmetric truncated plug nozzles.

The tools previously described lacked however the quantitative accuracy needed to become predictive tools for the design of new gas-metal atomizers. From these investigations on, the state-of-the-art in gas flow modeling for atomizers became computational fluid dynamics.

Piomelli (1992) modeled the gas-only flow in a number of close-coupled atomizer

geometries using the averaged Navier-Stokes equations. He studied the flow field from the beginning of the annular channel to the end-corner of the liquid-delivery tube and his results detailed the effects of: turbulence, stagnation pressure, and liquid-delivery tube angle, on the topography of the gas flow field. For these simulations, Piomelli divided the computational domain in two blocks: an annular channel, and the region over the liquid-delivery tube. He concluded that turbulence has a considerable effect on the jet structure of this type of flow and his results predicted the existence of a separation region at the end-corner of the liquid-delivery tube for a number of geometries and stagnation pressures. He hypothesized that this separation could lead to the adverse effect of metal-freeze-up which is a common occurrence during atomization. Metal-freeze-up – that is, the uncontrolled accumulation and solidification of metal at the end of the liquid-delivery tube – typically leads to the failure of the atomization process by disrupting the flow of gas and stopping the flow of liquid metal.

Figliola and Anderson (1993) presented numerical results for the gas-only flow field produced by the geometry they had previously studied experimentally, and gave particle paths and cooling rates based on a Lagrangian particle tracking scheme. Their gas-only simulations, which made use of the averaged Navier-Stokes equations in conjunction with Baldwin-Lomax or $k-\epsilon$ turbulence models, calculated the flow inside a computational domain that extended 5 liquid-delivery tube diameters downstream of the end of the annular channel, and two diameters radially from the axis of symmetry. As in their previous investigation (Anderson *et al.* 1989), discrepancies between their experimental and modeling data resulted from their selection of a two-dimensional approximation to represent a fundamentally axisymmetric flow field. Furthermore, these simulations were conducted using

96 × 56 mesh points (in the radial and axial direction, respectively), which were insufficient to ensure an accurate description of the features of the flow field. Nevertheless, based on their combined data, they were able to give a description of the gas-only flow field and proposed an “umbrella” break-up phenomenological model for the initial liquid disruption dynamics during gas-metal atomization.

Espina *et al.* (1993) presented numerical results for the gas-only flows produced by an annular jet version of the discrete jet geometry studied by Figliola and Anderson (1993). In their investigation, Espina *et al.* (1993) discretized the computational domain making use of three blocks: the annular channel, the section over the liquid-delivery tube, and the wake region after the liquid-delivery tube. They studied the effects of grid adaptation, viscosity, and extension of the liquid-delivery tube. Based on their findings they reached several conclusions. First, grid adaptation is essential if one hopes to capture the flow features with a reasonable number of mesh points. Second, the viscous stresses are of considerable magnitude and therefore cannot be ignored. Espina *et al.* (1993) went on to hypothesize that the same was probably true of the Reynolds stresses and therefore the selection of a turbulence model in this type of simulation would be of utmost importance. Finally, they concluded that the liquid-delivery tube should be as long as possible to allow for the maximum expansion of the underexpanded wall jet, which increases the amount of momentum available for transfer into the liquid stream. However, they pointed out that this effect rapidly degrades with the appearance of flow separation at the end of the liquid-delivery tube.

In the same year, Crucible Compaction Metals, became the first metal powder producer to apply CFD technology to the design of a commercial close-coupled gas-metal atomizer. Using technology developed by Espina *et al.* (1993), Con-

way and Lizzi (1993) designed an atomizer for the processing of the nickel-based superalloy – René 95. In trial runs, they found that the new atomizer yielded 27% more powder in the sub-106 μm particle size range than its predecessor. Their work represents a landmark in this field because they demonstrated that CFD results could be successfully transitioned from the research environment to the production floor, and that there were financial benefits to be obtained from such a transfer.

Kuntz and Payne (1995) developed the first numerical model that predicted particle size distributions in a close-coupled gas metal atomizer. In this research, they followed a decoupled approach to the problem by modeling the gas-only flow first and then using a particle disruption-tracking algorithm to calculate the resulting particle size distribution. Their gas-only simulations modeled the flow from the annular channel to a distance of 5 liquid-delivery tube diameters downstream of its end-corner and benefitted from high mesh resolution (52,893 points), grid adaptation, and turbulence modeling (using the Baldwin-Barth 1990 one-equation model). Their disruption model made use of a collection of semi-empirical models to characterize six disruption regimes: shear breakup, multi-mode breakup, bag breakup, oscillatory breakup, non-oscillatory breakup, and no deformation. Following this approach, Kuntz and Payne (1995) obtained particle size distributions with mass-median-diameter and Sauter-mean-diameter within 9 to 27% of the experimental values; they attributed this difference to the lack of droplet collision and droplet coalescence in their model.

Kuntz and Payne (1995) also reported their attempt to make use of the $k-\epsilon$ model in their investigation, which they expected would yield more accurate results than those obtained using the Baldwin-Barth model. However, they reported problems with the convergence of the solution using the $k-\epsilon$ model and eventually abandoned

it. Espina *et al.* (1993) had experienced similar problems. This is significant because both Kuntz and Payne (1995) and Espina *et al.* (1993) integrated the k - ϵ equations all the way to the wall, while, Figliola and Anderson (1993) reported no such problems with the use of k - ϵ models in their less resolved meshes, making use of wall functions.

Mi *et al.* (1996) presented new numerical results for the gas only flow in their gas metal atomizer (see Figliola and Anderson 1993). As part of this research, they tested their numerical method by simulating a simple underexpanded jet and found differences between the numerical and experimental results that ranged from 1.3 to 14.3%. For the atomization gas-only flow simulations they choose a computational domain that extended 5 liquid-delivery tube diameters downstream from the exit of the gas nozzle and made use of 400×70 mesh points. Although this time they used an axisymmetric algorithm to calculate the atomizer flow field, the resulting calculations predicted a flow different than the one intended due to a fundamental error in the problem formulation. In their experiments, in fact, Figliola and Anderson (1993) made use of an 18 discrete-jet atomization die, each nozzle having a diameter of ≈ 0.813 mm with a total critical area of approximately 9.34 mm^2 . However, in their axisymmetric simulations Mi *et al.* (1996) chose to use an annular slit with a gap of 0.813 mm, which, for their geometry, yielded a critical area of 53.70 mm^2 . This resulted in a 475% increase in the mass flux, and comparable amounts in the momentum and energy fluxes, considered in the calculation.

Finally, Miller *et al.* (1996) presented an analysis of the flow of liquid-metal, which made use of the numerical results of an inviscid simulation for the gas-only flow in one of General Electric's close-coupled atomization dies. However, they

chose not to disclose any of the details of their research due to GE proprietary restraints.

By no means does the preceding discussion encompass all the research in the area of close-coupled gas-metal atomization, since it concentrates on the work in the area on gas-only flow modeling. The interested reader is encouraged to review the additional literature in process control (Ando *et al.* 1990, Ridder *et al.* 1992, Hariprasad and Sastryand 1995), experimental flow studies (Mates and Settles 1995, 1996), and modeling of liquid-only flows (Liu *et al.* 1995, Liu and Dandy 1995).

1.3 Objectives of the present study

The objectives of this investigation are:

1. To determine the methodology needed to model gas-only flows in close-coupled atomizers using low Reynolds number k - ϵ models.
2. To validate this methodology by simulating a well documented flow that encompasses all the physical elements present in the atomizer gas-only flow – the supersonic base flow.
3. To compare and contrast the numerical predictions for the atomization gas-only flow with available experimental data.
4. To use both experiments and numerical simulations to study the effects of the stagnation pressure, the stagnation temperature, and liquid-delivery tube mass injection on the atomization gas-only flow field.
5. Make recommendations for the design and operation of future close-coupled atomizers based on the data presented.

Chapter 2 will describe the governing equations, physical models, and numerical methods used in this investigation. Chapter 3 will present an evaluation of the performance of the turbulence models introduced in Chapter 2, by comparing their results for an incompressible boundary layer against the direct numerical simulation data of Spalart (1988), and the results for a compressible boundary layer against the compressible law of the wall. In Chapter 4 the numerical methods will be put to the test by comparing the numerical results for a supersonic base flow with experimental measurements obtained by Herrin and Dutton (1994). Chapter 5 will present an analysis of the gas-only flow fields produced by the close-coupled atomizers studied by Espina *et al.* (1993). The numerical results will be compared with experimental measurements, while the critical details used during the simulation of these flows will be given as guidelines for future industrial research. In addition, the results will be used in the evaluation of the effects of various process parameters on the topography of the flow fields. Finally, in Chapter 6, conclusions and recommendations for the design of a new generation of close-coupled gas-metal atomizers will be drawn from the obtained data.

It is expected that the results of this investigation will enable metal-powder producers to make use of CFD tools accurately in the design of a new generation of close-coupled gas metal atomizers. It is anticipated that these atomizers will benefit from geometries that, for selected process parameters, will produce flow fields in which the energy and momentum transfers are maximized. This should lead to reduced operational cost (*i.e.*, smaller gas flow rates and lower stagnation pressures and temperatures), improved fine metal-powder yields, and scalability of the process, which up to this day has been optimized by trial and error.

Chapter 2

Mathematical Formulation

2.1 Governing equations

The flows of interest to this investigation are governed by the nonreacting, compressible Navier-Stokes equations. For a two-dimensional domain, and in nondimensionalized-vector form, these equations are given by

$$\frac{\partial Q}{\partial t} + \frac{\partial F_j}{\partial x_j} = \frac{1}{Re} \frac{\partial G_j}{\partial x_j}. \quad (2.1.1)$$

where $Q = (\rho, \rho u_1, \rho u_2, E)^T$ is the dependent variable vector containing the conservation variables, and the inviscid flux vector, F_j , and the viscous flux vector, G_j , are defined as

$$F_j = \begin{pmatrix} \rho u_j \\ \rho u_1 u_j + p \delta_{1j} \\ \rho u_2 u_j + p \delta_{2j} \\ (E + p)u_j \end{pmatrix}, \quad G_j = \begin{pmatrix} 0 \\ \tau_{1j} \\ \tau_{2j} \\ u_k \tau_{jk} - q_j \end{pmatrix}. \quad (2.1.2)$$

In the above equation, the index $j = 1, 2$, and summation is implied over repeated indices; Re is the reference Reynolds number, ρ is the dimensionless fluid density, and u_j is the dimensionless velocity component in the x_j direction; p is the dimensionless static pressure, δ_{ij} is the Kronecker delta, and $E = \rho(e + u_k u_k/2)$

is the dimensionless total energy per unit volume. If the fluid is assumed to be a thermally and calorically perfect gas, the dimensionless internal energy $e = p/\rho(\gamma - 1) = T/\gamma(\gamma - 1)$, where T is the dimensionless static temperature, and γ is the specific heat ratio which is taken to be constant.

In equation (2.1.1) the length scales were nondimensionalized by a reference length, x_{ref} and the velocities by a reference speed of sound, a_{ref} , the pressure by $\rho_{ref}a_{ref}^2$. All other quantities were nondimensionalized by their reference values. The reference Reynolds is given by

$$Re = \frac{\rho_{ref}a_{ref}x_{ref}}{\mu_{ref}}. \quad (2.1.3)$$

Assuming the fluid to be Newtonian, the viscous stresses are given by

$$\tau_{ij} = \mu \left(\frac{\partial u_i}{\partial x_j} + \frac{\partial u_j}{\partial x_i} \right) + \lambda \frac{\partial u_i}{\partial x_i} \delta_{ij} \quad (2.1.4)$$

where μ and λ are the first and second coefficients of molecular viscosity, respectively. The dimensionless Sutherland viscosity law is used to obtain the value of μ as a function of T :

$$\mu = T^{3/2} \frac{1 + S}{T + S} \quad (2.1.5)$$

where S is the nondimensional Sutherland constant (White 1991), and $\lambda = -2/3 \mu$, by Stokes' hypothesis.

The heat flux vector is modeled using Fourier's heat-conduction law

$$q_j = -\frac{k}{\beta Pr} \frac{\partial T}{\partial x_j} \quad (2.1.6)$$

where k is the dimensionless thermal conductivity, $\beta = a_{ref}^2/(c_{p,ref}T_{ref})$ is the reference Eckert number, and $Pr = c_{p,ref}\mu_{ref}/k_{ref}$ is the reference Prandtl number. Given that the fluid is assumed to be calorically perfect, the dimensionless thermal

conductivity can be expressed as

$$k = \mu \tag{2.1.7}$$

provided that the Prandtl number is taken to be constant.

If the system (2.1.1) is transformed into a curvilinear coordinate system $\xi_j = \xi_j(x_i, t)$, it can be written as

$$\frac{\partial \hat{Q}}{\partial t} + \frac{\partial \hat{F}_j}{\partial \xi_j} = \frac{1}{Re} \frac{\partial \hat{G}_j}{\partial \xi_j}, \tag{2.1.8}$$

with

$$\hat{Q} = \frac{1}{J} Q, \quad \hat{F}_j = \frac{1}{J} \left(\frac{\partial \xi_j}{\partial t} Q + \frac{\partial \xi_j}{\partial x_k} F_k \right), \quad \hat{G}_j = \frac{1}{J} \frac{\partial \xi_j}{\partial x_k} G_k, \tag{2.1.9}$$

where J is the Jacobian of the transformation (Pulliam and Steger 1980).

The specification of a problem governed by equation (2.1.8) is completed by assigning boundary and initial conditions. At solid boundaries, adiabatic, no-slip boundary conditions are imposed on the velocity; homogeneous Neumann boundary conditions apply for p and T . At inlets, the flow is assumed to be normal to the boundary and the stagnation pressure, P_o , and temperature, T_o , are prescribed. The normal velocity, u_n , is then obtained using a characteristic equation by Newton iteration (Cooper and Sirbaugh 1989). At outlets, the flow normal to the boundary is first determined to be either subsonic or supersonic. In the case of subsonic outflow, the static pressure is prescribed, and first-order extrapolation is used for the density and the velocity. In the case of supersonic flow, all variables are extrapolated using first-order extrapolation.

The initial condition is taken to be a flow solution obtained from a previous calculation using similar conditions. Where no previous calculations existed, an initial guess was used.

2.2 Turbulence models

In this investigation, the effects of turbulence are accounted for by making use of an eddy-viscosity model, in which the molecular viscosity in the stress tensor expression (2.1.4) is replaced by an effective viscosity that contains both the molecular and the eddy contributions.

$$\mu_{eff} = \mu + \mu_t. \quad (2.2.10)$$

Three different eddy-viscosity type turbulence models were used: the Baldwin-Lomax model, Chien's k - ϵ model, and Grasso-Falconi's k - ϵ model.

2.2.1 Baldwin-Lomax model

The Baldwin-Lomax model (1978) is a two-layer, algebraic, eddy-viscosity formulation that was patterned after a model by Cebeci (1970). The Baldwin-Lomax model differs from the Cebeci model in that the vorticity is used to determine the mixing length scale, thus avoiding the need to find the edge of boundary layers (or wakes), which extends its generality.

In this model, the flow above a wall is divided into inner and outer layers based on a crossover-distance criterion. Depending on the outcome of this selection, the eddy-viscosity, μ_t , is then calculated using one of two models

$$\mu_t = \begin{cases} \mu_{t_{inner}} & \text{for } y \leq y_{crossover} \\ \mu_{t_{outer}} & \text{for } y > y_{crossover} \end{cases} \quad (2.2.11)$$

In the above definition, y is the wall-normal distance and $y_{crossover}$ is the shortest distance from the wall at which both models yield the same result.

For the **inner** model, the Prandtl-van Driest formulation is used to determine the

eddy-viscosity

$$\mu_t = \rho \ell^2 |\omega| Re. \quad (2.2.12)$$

In this expression, the mixing length is given by

$$\ell = \kappa y [1 - \exp(-y^+/A^+)] \quad (2.2.13)$$

where $y^+ = \rho u_\tau y / \mu$ is the viscous length scale, $\kappa = 0.4$ is the von Kármán constant, $A^+ = 26$, $|\omega|$ is the magnitude of the vorticity vector, and u_τ is the friction velocity.

For the **outer** model, the eddy-viscosity is obtained using a modified Clauser formulation:

$$\mu_t = \rho K_c C_{cp} F_{wake} F_{kleb}(y) Re. \quad (2.2.14)$$

In this expression, $K_c = 0.0168$ is the Clauser constant, $C_{cp} = 1.6$, and

$$F_{wake} = \min \begin{cases} y_{\max} F(y)_{\max} \\ C_{wk} y_{\max} u_{dif}^2 / F(y)_{\max} \end{cases} \quad (2.2.15)$$

where $y_{\max} F(y)_{\max}$ replaces $\delta^* u_e$ in the original Clauser formulation and $y_{\max} u_{dif}^2 / F(y)_{\max}$ replaces δu_{dif} in the wake formulation (Cebeci 1970). In the above, $F(y) = y |\omega| [1 - \exp(-y^+/A^+)]$, $C_{wk} = 0.25$, and $u_{dif} = |u|_{\max} - |u|_{\min}$ along a given wall-normal location. The Klebanoff intermittency factor is given by

$$F_{kleb} = \left[1 + 5.5 \left(\frac{y C_{kleb}}{y_{\max}} \right)^6 \right]^{-1} \quad (2.2.16)$$

where $C_{kleb} = 0.3$. In the case of free flows, $F(y) = y |\omega|$, where y is measured from the line of symmetry of the free flow.

In this investigation, the Baldwin-Lomax model was integrated normal to each computational domain boundary until another boundary was encountered along the integration path. In the case that a grid point would have contributions of more than one boundary (*i.e.*, an concave corner), the eddy-viscosity was averaged over

the contributions of all boundaries involved. At the axis of symmetry, only the outer formulation of the Baldwin-Lomax model was used and y was taken to be zero at the axis.

Homogeneous Dirichlet boundary conditions were applied at the wall for μ_t , while zeroth-order extrapolation was used on the other boundaries.

2.2.2 Chien k - ϵ model

In this work, we made use of a compressible version of Chien's (1982) k - ϵ model as implemented by Georgiadis *et al.* (1994) in the NPARC code. The original model was first proposed as an extension of the Jones and Launder (1972) k - ϵ model that allowed for the integration of the k and ϵ equations all the way down to solid walls.

In this compressible version of the original incompressible model, the k and ϵ equations are given by

$$\frac{D\rho k}{Dt} = \frac{1}{Re} \left\{ \frac{\partial}{\partial x_j} \left[\left(\mu + \frac{\mu_t}{\sigma_k} \right) \frac{\partial k}{\partial x_j} \right] + \mathcal{P}_k - \mathcal{D}_k - \frac{2\mu k}{y^2} \right\} \quad (2.2.17)$$

$$\frac{D\rho\epsilon}{Dt} = \frac{1}{Re} \left\{ \frac{\partial}{\partial x_j} \left[\left(\mu + \frac{\mu_t}{\sigma_\epsilon} \right) \frac{\partial \epsilon}{\partial x_j} \right] + \mathcal{P}_\epsilon - \mathcal{D}_\epsilon - \frac{\epsilon}{k} \left[\frac{2\mu k}{y^2} e^{-0.5y^+} \right] \right\} \quad (2.2.18)$$

where k is the Favre-averaged turbulence kinetic energy, $k = 1/2 \overline{\rho u'_i u'_i} / \rho$ (u'_i representing the fluctuating component of the instantaneous u_i velocity component), and ϵ is the turbulence kinetic energy dissipation rate. D/Dt represents the substantial derivative based on the averaged velocity, and σ_k and σ_ϵ are the turbulent Prandtl numbers. The production terms, \mathcal{P}_k and \mathcal{P}_ϵ , and the dissipation terms, \mathcal{D}_k and \mathcal{D}_ϵ , are given by

$$\begin{aligned} \mathcal{P}_k &= 2\mu_t \frac{\partial u_i}{\partial x_j} S_{ij} & \mathcal{D}_k &= \rho\epsilon(1 + \alpha_1 M_t^2) Re \\ \mathcal{P}_\epsilon &= C_{\epsilon 1}(\epsilon/k)\mathcal{P}_k & \mathcal{D}_\epsilon &= C_{\epsilon 2} f_2 \rho(\epsilon^2/k) Re \end{aligned} \quad (2.2.19)$$

where

$$S_{ij} = \frac{1}{2} \left(\frac{\partial u_i}{\partial x_j} + \frac{\partial u_j}{\partial x_i} \right), \quad (2.2.20)$$

is the strain-rate tensor, and $\epsilon \alpha_1 M_t^2$ is a compressible dissipation correction proposed by Sarkar and Balakrishnan (1991) with $\alpha_1 = 1.0$. The turbulence Mach number is defined as $M_t = \sqrt{2k/(\gamma RT)}$, and f_2 is a damping function given by

$$f_2 = 1 - 0.22 \exp(-Re_t/6)^2 \quad (2.2.21)$$

where the turbulence Reynolds number is defined as $Re_t = Re \rho k^2/(\mu \epsilon)$.

The last terms on the right-hand sides of equations (2.2.17) and (2.2.18) are the “wall” dissipation terms added by Chien (1982) to the Jones and Launder (1972) model to balance the addition of the viscous dissipation terms (*i.e.*, $\partial/\partial x_j(\mu \partial k/\partial x_j)$ and $\partial/\partial x_j(\mu \partial \epsilon/\partial x_j)$). Chien (1982) explains that the “wall” dissipation terms are needed because near the wall, $k \sim y^2$, and this leads to a finite viscous dissipation of k at the wall, rendering the k equation non-homogeneous at the wall. With the addition of the “wall” dissipation terms, ϵ is considered to be the “isotropic” dissipation rate, while $\epsilon + 2\nu k/y^2$ is the “true” kinetic energy dissipation rate. The effects of these terms will be discussed in more detail in the next chapter as we evaluate their contribution to the wall turbulence in a boundary layer over a flat plate.

When integrated, the dependent variables in equations (2.2.17) and (2.2.18) can be related to the eddy-viscosity by the following expression (see Chien 1982),

$$\mu_t = C_\mu f_\mu \rho \ell_m k^{1/2} Re \quad (2.2.22)$$

where C_μ is a proportionality constant with a value of 0.09, f_μ is a wall function defined in terms of the viscous length scale as

$$f_\mu = 1 + \exp(-0.0115y^+) \quad (2.2.23)$$

and ℓ_m is a characteristic turbulence length scale given by

$$\ell_m = \frac{k^{3/2}}{\epsilon}. \quad (2.2.24)$$

In this model, the values for the turbulence Prandtl numbers proposed by Jones and Launder (1972) are used: $\sigma_k = 1.0$, $\sigma_\epsilon = 1.3$. However, a value of $C_{\epsilon 2} = 1.8$ was used which was deduced from the decay of high-Reynolds-number grid turbulence data by Hanjalic and Launder (1976). The value of $C_{\epsilon 1} = 1.35$ was obtained by keeping the difference between $C_{\epsilon 1}$ and $C_{\epsilon 2}$ as prescribed in the Jones and Launder (1972) model. This difference results from the observation that the production and dissipation rates of turbulence energy are nearly in balance in wall bounded flows.

Finally, homogeneous Dirichlet boundary conditions were used at the wall for all turbulence quantities. As seen before, the non-physical declaration of homogeneous Dirichlet boundary conditions for ϵ is enabled by the use of the “wall” dissipation term in equation (2.2.18). Zeroth-order extrapolation was used at outlets. At inlets, the eddy-viscosity was set to, $\mu_t = 100\mu$, while the turbulence intensity (assuming the inlet turbulence field to be isotropic),

$$I = \left(\frac{\overline{u'^2}}{V^2} \right)^{\frac{1}{2}} = \left(\frac{\overline{v'^2}}{V^2} \right)^{\frac{1}{2}} = \left(\frac{\overline{w'^2}}{V^2} \right)^{\frac{1}{2}} = \left(\frac{2}{3} \frac{k}{V^2} \right)^{\frac{1}{2}}, \quad (2.2.25)$$

was set to 0.005.

2.2.3 Grasso-Falconi k - ϵ model

This model was developed by Grasso and Falconi (1993) to parameterize the effects of turbulence in complex flows characterized by strong streamwise curvature, adverse pressure gradients, separated flows, etc. Their model differs from Chien’s (1982) in that it was directly conceived as a compressible formulation.

In this model the k and ϵ equations are given by

$$\begin{aligned} \frac{Dk}{Dt} = & \frac{1}{Re} \left\{ \frac{\partial}{\partial x_j} \left[\left(\mu + \frac{\mu_t}{\sigma_k} \right) \frac{\partial k}{\partial x_j} \right] + \mathcal{P}_k - \mathcal{D}_k \right. \\ & \left. + \Pi_{c,1} + \Pi_{c,2} + \Pi_{c,3} \right\} \end{aligned} \quad (2.2.26)$$

$$\frac{D\epsilon}{Dt} = \frac{\partial}{\partial x_j} \left[\left(\mu + \frac{\mu_t}{\sigma_\epsilon} \right) \frac{\partial \epsilon}{\partial x_j} \right] + \mathcal{P}_\epsilon - \mathcal{D}_\epsilon. \quad (2.2.27)$$

where the turbulent Prandtl number, σ_k , was assigned a value of 1.55 based on a heat transfer study of separated flows performed by Spalding (1967), and σ_ϵ was given a value of 2.0, obtained by assuming the same proportionality as the Chien k - ϵ model (1982) turbulent Prandtl numbers. The production terms, \mathcal{P}_k and \mathcal{P}_ϵ , and the dissipation terms, \mathcal{D}_k and \mathcal{D}_ϵ , are given by

$$\begin{aligned} \mathcal{P}_k &= [2\mu_t S_{ij} - {}^{2/3}\mu_t S_{ll} \delta_{ij} - {}^{2/3}\rho k \delta_{ij} Re] S_{ij} & \mathcal{D}_k &= \rho \epsilon Re \\ \mathcal{P}_\epsilon &= C_{\epsilon 1} (\epsilon/k) \mathcal{P}_k & \mathcal{D}_\epsilon &= C_{\epsilon 2} f_2 \rho (\epsilon^2/k) Re \end{aligned} \quad (2.2.28)$$

where the damping function f_2 is given by

$$f_2 = [1 - \exp(-y^+/A)]^2 \quad (2.2.29)$$

following the work of Speziale *et al.* (1992). The constant A was assigned a value of 4.9, on the basis of direct numerical simulations of planar channel flow. For this model, Grasso and Falconi (1993) chose a turbulent Reynolds number dependence of the constant $C_{\epsilon 2}$ proposed by Vandromme (1983) and given by

$$C_{\epsilon 2} = 1.83[1 - ({}^{2/9}) \exp(-Re_t^2/36)], \quad (2.2.30)$$

while $C_{\epsilon 1} = 1.60$ was obtained from the equilibrium relation.

The additional compressible terms in equation (2.2.26) represent the pressure-dilatation $-\Pi_{c,1}$, the Favre-velocity contribution $-\Pi_{c,2}$, and the dilatation-dissipation

– $\Pi_{c,3}$. These terms are defined and modeled as follows:

$$\Pi_{c,1} = \overline{p'u'_{i,i}} \simeq (-\alpha_2 \mathcal{P}_k + \alpha_3 \rho \epsilon Re) M_t^2 \quad (2.2.31)$$

$$\Pi_{c,2} = \frac{\overline{\rho'u'_i}}{\rho} \frac{\partial p}{\partial x_i} \simeq -\frac{\mu_t}{\rho^2} \frac{1}{\sigma_p} \frac{\partial \rho}{\partial x_j} \frac{\partial p}{\partial x_j} \quad (2.2.32)$$

$$\Pi_{c,3} = -\rho \left[\frac{4}{3} (\nu \overline{S'_{ll} S'_{ll}}) \right] \simeq -0.4 \rho \epsilon Re \left\{ 1 - \exp \left[- \left(\frac{M_t - 0.3}{0.8} \right)^2 \right] \right\}. \quad (2.2.33)$$

The pressure-dilatation model (2.2.31) results from the assumption that the pressure fluctuations can be decomposed into incompressible and compressible fluctuations of which the incompressible part only contributes to the pressure-dilatation (Erlebacher *et al.* 1990, Sarkar *et al.* 1991, and Sarkar 1992). Grasso and Falconi selected $\alpha_2 = 0.40$ and $\alpha_3 = 0.20$. It is worth mentioning that this selection of a positive value of α_3 makes the compressible dissipation contribution a production term in the turbulence kinetic energy equation, which is contrary to the description of the contribution given by Sarkar and Balakrishnan (1991).

The Favre-velocity contribution (2.2.32) follows from the observation of large pressure fluctuations in high-speed flows, and therefore, it is argued that the scalar product of the Favre-velocity and the mean pressure gradient may contribute to the turbulence energy balance. This contribution is modeled using a gradient law, as suggested by Speziale and Sarkar (1989). The turbulent Prandtl number, σ_p , is given a value of 0.5.

The dilatation-dissipation term (2.2.33) is modeled according to the work of Zeman (1990), which attributes the dilatational contribution to the Reynolds stress to shock-like eddy structures embedded within energy-containing eddies. Zeman expressed this contribution in terms of an exponential function of the turbulent

Mach number that is activated at a given threshold. Based on work by Wilcox (1991), Grasso and Falconi increased the turbulent Mach number threshold to 0.3 in their model.

In this k - ϵ model the eddy-viscosity is given by

$$\mu_t = C_\mu f_\mu \rho \ell_m k^{1/2} \quad (2.2.34)$$

where $C_\mu = 0.09$, and the wall function f_μ (Speziale *et al.* 1992)

$$f_\mu = \left[1 + (3.45/\sqrt{Re_t}) \right] \tanh(y^+/80). \quad (2.2.35)$$

Under certain circumstances, (2.2.35) can lead to values of f_μ larger than 1.0, reversing its desired damping behavior. To prevent this, f_μ should be limited to a maximum value of 1.0 (Grasso 1997). The turbulent length scale, ℓ_m , is bounded by the following equation

$$\ell_m = \min \left(C_\ell y, \frac{k^{3/2}}{\epsilon} \right) \quad (2.2.36)$$

to prevent the overprediction of peak heating near the wall. In equation (2.2.36), y is the distance from the wall and C_ℓ is a proportionality constant that is a function of the von Kármán constant. C_ℓ is given a value of 2.25.

Finally, homogeneous Dirichlet boundary conditions are applied at the wall for the turbulence kinetic energy, and homogeneous Neumann boundary conditions are applied normal to the wall for the turbulence dissipation rate. First-order extrapolation is used at outlets. At inlets the eddy-viscosity was set to, $\mu_t = 100\mu$, while the turbulence intensity was set to $I = 0.005$.

2.3 Numerical method

In this investigation, the governing equations (2.1.8) were solved using two computer programs: NPARC, Version 2.1, and SAGE, Version 2.

The NPARC code is an ADI compressible flow solver which is maintained by the NPARC Alliance — NASA Lewis Research Center/Arnold Engineering Development Center — (Cooper and Sirbaugh 1989, Sirbaugh *et al.* 1994). The solver is derived from the AIR and ARC codes produced at NASA Ames Research Center (Pulliam and Steger 1980, Pulliam 1984).

In the NPARC code, the solution to the turbulence equations (2.2.17 and 2.2.18, or 2.2.26 and 2.2.27) is time-lagged with respect to the solution to the governing equations (2.1.8). This simplifies the algorithm and allows for the implementation of different schemes for the solution of the governing and turbulence equations. Section 2.3.1 describes the numerical scheme used to solve the governing equations, while Section 2.3.2 describes the scheme used to solve the turbulence equations.

The second computer program used in this investigation is a structured grid-adaptation program named SAGE (Davies and Venkatapathy 1992). The program makes use of the self-adaptive-grid method developed by Nakahashi and Deiwert (1985) and is briefly described in Section 2.3.3.

2.3.1 Solution of the governing equations

In the NPARC code, equation (2.1.8) is solved numerically using the Beam and Warming (1976) approximate factorization algorithm. Making use of Euler backward time-differencing, and assuming locally constant transport coefficients, the

Beam and Warming algorithm can be written as

$$\Delta\widehat{Q}^n + \Delta t^n \left(\frac{\partial\widehat{F}_j^{n+1}}{\partial\xi_j} - \frac{1}{Re} \frac{\partial\widehat{G}_j^{n+1}}{\partial\xi_j} \right) = 0 \quad (2.3.37)$$

where $\Delta\widehat{Q}^n = \widehat{Q}^{n+1} - Q^n$. Equation (2.3.37) cannot be readily solved because the flux vectors are expressed as nonlinear functions of the dependent variables. This can be alleviated by time linearization of the flux vectors as

$$\begin{aligned} \widehat{F}_j^{n+1} &= \widehat{F}_j^n + A_j^n \Delta\widehat{Q}^n + \mathcal{O}[(\Delta t^n)^2] \\ \widehat{G}_j^{n+1} &= \widehat{G}_j^n + R_j^n \Delta\widehat{Q}^n + \mathcal{O}[(\Delta t^n)^2] \end{aligned} \quad (2.3.38)$$

where \mathcal{O} is the order of the error in the linearization, and the Jacobians, A_j and R_j , are given by

$$A_j = \frac{\partial\widehat{F}_j}{\partial\widehat{Q}}, \quad R_j = \frac{\partial\widehat{G}_j}{\partial\widehat{Q}}. \quad (2.3.39)$$

In the NPARC code, only the inviscid flux vector is treated implicitly (Pulliam and Chaussee 1981), thus allowing for the diagonalization of the algorithm without the use of approximate viscous eigenvalues and eigenvectors. It can be shown (Hirsch 1990) that this approximation introduces an error of $\mathcal{O}[(\Delta t^n)^2]$, not degrading the overall accuracy of the algorithm. With this in mind, the version of the Beam and Warming algorithm used in the NPARC code is

$$\left(I + \Delta t^n \frac{\partial}{\partial\xi_j} A_j^n \right) \Delta\widehat{Q}^n = -\Delta t^n \left(\frac{\partial\widehat{F}_j^n}{\partial\xi_j} - \frac{1}{Re} \frac{\partial\widehat{G}_j^n}{\partial\xi_j} \right) \quad (2.3.40)$$

where I denotes the identity matrix of appropriate rank.

The above algorithm results in a sparse block system of equations whose solution is computationally expensive. One way of reducing this expense is by approximately factoring the left-hand side operator in equation (2.3.40) into a series of one dimensional diagonal operators. For example, in two dimensions this approx-

imate factorization yields,

$$\begin{aligned} & \left(I + \Delta t^n \left[\frac{\partial}{\partial \xi} \widehat{A}_1^n + \frac{\partial}{\partial \eta} \widehat{A}_2^n \right] \right) \Delta \widehat{Q}^n \\ & = \left(I + \Delta t \frac{\partial}{\partial \xi} \widehat{A}_1^n \right) \left(I + \Delta t \frac{\partial}{\partial \eta} \widehat{A}_2^n \right) \Delta \widehat{Q}^n - \mathcal{O} [(\Delta t^n)^2] \end{aligned} \quad (2.3.41)$$

where as seen, the error in the approximation remains within $\mathcal{O}[(\Delta t^n)^2]$, not degrading the overall accuracy of the algorithm.

In this work, the governing equations are solved in an axisymmetric domain (i.e, $j = 1, 2$). If the axis of symmetry is allowed to coincide with the x -axis, equation (2.1.8) can be written as

$$\frac{\partial \widehat{Q}}{\partial t} + \frac{\partial \widehat{F}_1}{\partial \xi} + \frac{\partial \widehat{F}_2}{\partial \eta} = \widehat{H} + \frac{1}{Re} \left(\frac{\partial \widehat{G}_1}{\partial \xi} + \frac{\partial \widehat{G}_2}{\partial \eta} \right) \quad (2.3.42)$$

where \widehat{H} is the axisymmetric source term given by

$$\widehat{H} = \left(0, 0, \frac{1}{J_{2D}} \left[p - \frac{1}{Re} \left\{ 2\mu \frac{J}{J_{2D}} v + \lambda \nabla_a \cdot \vec{V} \right\} \right], 0 \right)^T \quad (2.3.43)$$

and

$$J_{2D} = \xi_x \eta_y - \xi_y \eta_x, \quad \nabla_a \cdot \vec{V} = \frac{J}{J_{2D}} v + u_x + v_y. \quad (2.3.44)$$

On the right-hand side of equation (2.3.42), all appearances of the two-dimensional divergence, $\nabla \cdot \vec{V}$, are replaced by its axisymmetric counterpart, $\nabla_a \cdot \vec{V}$. The metrics of the transformation are given by (Cooper and Sirbaugh 1989)

$$\begin{aligned} J^{-1} &= (x_\xi y_\eta - x_\eta y_\xi) y, \\ \xi_x &= y y_\eta J, & \xi_y &= -y x_\eta J, \\ \eta_x &= -y y_\xi J, & \eta_y &= y x_\xi J. \end{aligned} \quad (2.3.45)$$

For this domain, the algorithm in equation (2.3.40) reduces to

$$\begin{aligned}
& \left(I + \Delta t^n \left[\frac{\partial}{\partial \xi} \hat{A}_1^n + \frac{\partial}{\partial \eta} \hat{A}_2^n \right] \right) \Delta \hat{Q}^n \\
& = -\Delta t^n \left(\frac{\partial \hat{F}_1^n}{\partial \xi} + \frac{\partial \hat{F}_2^n}{\partial \eta} - \hat{H}^n - \frac{1}{Re} \left[\frac{\partial \hat{G}_1^n}{\partial \xi} + \frac{\partial \hat{G}_2^n}{\partial \eta} \right] \right)
\end{aligned} \tag{2.3.46}$$

where the axisymmetric source term is treated explicitly following the same reasoning used for the viscous flux vector. Making use of approximate factorization, the above system can be replaced by a series of block diagonal operators as follows:

$$\begin{aligned}
& \left(I + \Delta t \frac{\partial}{\partial \xi} \hat{A}_1^n \right) \left(I + \Delta t \frac{\partial}{\partial \eta} \hat{A}_2^n \right) \Delta \hat{Q}^n \\
& = -\Delta t \left(\frac{\partial \hat{F}_1^n}{\partial \xi} + \frac{\partial \hat{F}_2^n}{\partial \eta} - \hat{H}^n - \frac{1}{Re} \left[\frac{\partial \hat{G}_1^n}{\partial \xi} + \frac{\partial \hat{G}_2^n}{\partial \eta} \right] \right)
\end{aligned} \tag{2.3.47}$$

The block operators on the left-hand side of equation (2.3.47) can be decomposed into scalar operators following the diagonalization method proposed by Pulliam and Chaussee (1981), according to which the Jacobian matrices, \hat{A}_j , are decomposed into a complete set of real eigenvectors and real eigenvalues as (no summation applies to repeated indices in the following)

$$\hat{A}_j = \hat{T}_j \hat{\Lambda}_j \hat{T}_j^{-1} \tag{2.3.48}$$

where Λ_j is the diagonal matrix of eigenvalues of A_j , T_j is the matrix of right eigenvectors, and T_j^{-1} is its inverse. Making use of (2.3.48), the block operators in (2.3.47) can be diagonalized as follows:

$$\left(I + \Delta t \frac{\partial}{\partial \xi} \hat{A}_1 \right) = \left(\hat{T}_j \hat{T}_j^{-1} + \Delta t \frac{\partial}{\partial \xi} \hat{T}_j \hat{\Lambda}_j \hat{T}_j^{-1} \right) \approx \hat{T}_j \left(I + \Delta t \frac{\partial}{\partial \xi} \hat{\Lambda}_j \right) \hat{T}_j^{-1} \tag{2.3.49}$$

leading to the following diagonalized form of the factored algorithm

$$\begin{aligned}
& (\hat{T}_1)^n \left(I + \Delta t \frac{\partial}{\partial \xi} \hat{\Lambda}_1^n \right) (\hat{T}_1^{-1} \hat{T}_2)^n \left(I + \Delta t \frac{\partial}{\partial \eta} \hat{\Lambda}_2^n \right) (\hat{T}_2^{-1})^n \Delta \hat{Q}^n \\
& = RHS_{(2.3.47)}.
\end{aligned} \tag{2.3.50}$$

The closed-form expressions for Λ_j , T_j , and T_j^{-1} can be found in Cooper and Sirbaugh (1989).

If central finite differences are used to approximate the spatial differential operators in equation (2.3.50), the solution can contain oscillations due to discontinuities in the conservation variables (*i.e.*, shock waves) and/or the decoupling of the even-odd modes. These oscillations can be removed by adding a controlled amount of numerical dissipation to the scheme. In the NPARC code, this is done following a model proposed by Jameson *et al.* (1981), in which second-order artificial dissipation is used to smooth discontinuities associated with shock waves, and fourth-order dissipation is used to couple the even and odd modes of the solution. The artificial dissipation is added implicitly, modifying the diagonalized form of the factored algorithm (2.3.50) as follows:

$$\begin{aligned}
(\hat{T}_1)^n \left[I(1 + \mathcal{D}_1^n) + \Delta t \frac{\partial}{\partial \xi} \hat{\Lambda}_1^n \right] (\hat{T}_1^{-1} \hat{T}_2)^n \left[I(1 + \mathcal{D}_2^n) + \Delta t \frac{\partial}{\partial \eta} \hat{\Lambda}_2^n \right] (\hat{T}_2^{-1})^n \Delta \hat{Q}^n \\
= RHS_{(2.3.47)}^n
\end{aligned} \tag{2.3.51}$$

where \mathcal{D}_1 and \mathcal{D}_2 are the implicit artificial dissipation operators given by

$$\begin{aligned}
\mathcal{D}_1 &= \nabla_\xi \left[C_\xi \left(\varepsilon^{(2)} \Delta_\xi - \varepsilon^{(4)} \Delta_\xi \nabla_\xi \Delta_\xi \right) \right] J \\
\mathcal{D}_2 &= \nabla_\eta \left[C_\eta \left(\varepsilon^{(2)} \Delta_\eta - \varepsilon^{(4)} \Delta_\eta \nabla_\eta \Delta_\eta \right) \right] J.
\end{aligned} \tag{2.3.52}$$

In the above expressions, $\varepsilon^{(2)}$ and $\varepsilon^{(4)}$ are the second- and fourth-order artificial dissipation coefficients, respectively, given by

$$\begin{aligned}
\varepsilon^{(2)} &= K_2 \Delta t f \\
\varepsilon^{(4)} &= \max(0, K_4 \Delta t - \varepsilon^{(2)})
\end{aligned} \tag{2.3.53}$$

where K_2 and K_4 are control constants used to regulate the amount of artificial dissipation introduced into the algorithm, and f is a switch function, that takes the form

$$f = \max(f_\xi, f_\eta) \quad (2.3.54)$$

where

$$f_\xi = \frac{|p(\xi + 1, \eta) - 2p(\xi, \eta) + p(\xi - 1, \eta)|}{|p(\xi + 1, \eta) + 2p(\xi, \eta) + p(\xi - 1, \eta)|} \quad (2.3.55)$$

$$f_\eta = \frac{|p(\xi, \eta + 1) - 2p(\xi, \eta) + p(\xi, \eta - 1)|}{|p(\xi, \eta + 1) + 2p(\xi, \eta) + p(\xi, \eta - 1)|}.$$

In actual usage, the function f is smoothed over immediately neighboring points.

For the control constants, Jameson *et al.* (1981) suggest values of K_2 between 0 and 0.25, and of K_4 between 0 and 0.64; however, a minimal amount of fourth-order artificial dissipation is recommended to ensure the coupling of the even-odd modes in the solution.

In equation (2.3.52), Δ and ∇ are the first-order forward and backwards difference operators, respectively. The C_{ξ_i} 's are the nonlinear coefficients, are given by

$$C_\xi = C(\xi + 1, \eta) + C(\xi, \eta) \quad (2.3.56)$$

$$C_\eta = C(\xi, \eta + 1) + C(\xi, \eta)$$

where C is the summation of the spectral radii of the inviscid flux vector Jacobian, A_j , *i.e.*,

$$C = \left[(|U| + a\sqrt{\xi_x^2 + \xi_y^2}) + (|V| + a\sqrt{\eta_x^2 + \eta_y^2}) \right] J^{-1}, \quad (2.3.57)$$

where U and V are the contravariant velocities defined as

$$U_j = \frac{\partial \xi_j}{\partial t} + u_k \frac{\partial \xi_j}{\partial x_k}, \quad (2.3.58)$$

and a is the nondimensional local speed of sound. Since the artificial dissipation appears only in the left-hand-side of the equations, it only affects the transient part of the solution. At steady state the Navier-Stokes equations are satisfied, as the right-hand-side of equation (2.3.47) approaches zero.

If the spatial derivatives are replaced by finite differences, equation (2.3.51) yields the following algorithm:

$$\begin{aligned}
(\widehat{T}_1)^n \Big|_{j,k} \Delta \widehat{Q}^{(4)} \Big|_{j,k} &= -\Delta t \left[(\delta_\xi \widehat{F}_1^n + \delta_\eta \widehat{F}_2^n) - \widehat{H}^n - \frac{1}{Re} (d_\xi \widehat{G}_1^n + d_\eta \widehat{G}_2^n) \right] \Big|_{j,k} \\
\left[I(1 + \mathcal{D}_1^n) + \Delta t \delta_\xi \widehat{\Lambda}_1^n \right] \Big|_{j,k} \Delta \widehat{Q}^{(3)} \Big|_{j,k} &= \Delta \widehat{Q}^{(4)} \Big|_{j,k} \\
(\widehat{T}_1^{-1} \widehat{T}_2)^n \Big|_{j,k} \Delta \widehat{Q}^{(2)} \Big|_{j,k} &= \Delta \widehat{Q}^{(3)} \Big|_{j,k} \\
\left[I(1 + \mathcal{D}_2^n) + \Delta t \delta_\eta \widehat{\Lambda}_2^n \right] \Big|_{j,k} \Delta \widehat{Q}^{(1)} \Big|_{j,k} &= \Delta \widehat{Q}^{(2)} \Big|_{j,k} \\
(\widehat{T}_2^{-1})^n \Big|_{j,k} \Delta \widehat{Q}^n \Big|_{j,k} &= \Delta \widehat{Q}^{(1)} \Big|_{j,k} \\
\widehat{Q}^{n+1} \Big|_{j,k} &= \widehat{Q}^n \Big|_{j,k} + \Delta \widehat{Q}^n \Big|_{j,k}
\end{aligned} \tag{2.3.59}$$

where δ_ξ and δ_η are the second-order central difference operators in the ξ and η directions, defined as

$$\delta_\xi f = \frac{1}{2} [f_{j+1,k} - f_{j-1,k}], \quad \delta_\eta f = \frac{1}{2} [f_{j,k+1} - f_{j,k-1}], \tag{2.3.60}$$

since, in the transformed coordinates, $\Delta\xi = \Delta\eta = 1$. Similarly, d_ξ and d_η are the half-point central difference operators in the ξ and η directions, defined as

$$d_\xi f = [f_{j+1/2,k} - f_{j-1/2,k}], \quad d_\eta f = [f_{j,k+1/2} - f_{j,k-1/2}]. \tag{2.3.61}$$

In the NPARC code, the two scalar pentadiagonal systems that result from (2.3.59) are solved using a scalar pentadiagonal version of the Thomas algorithm (Cooper and Sirbaugh, 1989).

As mentioned before, this implicit algorithm is second-order accurate in space and first-order accurate in time. However, the NPARC code makes use of explicit boundary conditions to prevent changes in the structure of the pentadiagonal matrices in (2.3.59). This improves the generality of the code at the expense of more restrictive limitations in the stability bound of the algorithm.

2.3.2 Solution of the turbulence equations

In vector form, for a stationary curvilinear coordinate system, the nondimensional, conservative, compressible k - ϵ equations are given by

$$\frac{\partial \hat{Q}}{\partial t} + \frac{\partial \hat{F}_j}{\partial \xi_j} = \frac{1}{Re} \left(\frac{\partial \hat{G}_j}{\partial \xi_j} + \hat{S} \right) \quad (2.3.62)$$

where

$$\hat{Q} = J^{-1} \begin{bmatrix} \rho k \\ \rho \epsilon \end{bmatrix}, \quad \hat{F}_j = J^{-1} \begin{bmatrix} \rho k u_j \\ \rho \epsilon u_j \end{bmatrix}, \quad (2.3.63)$$

$$\hat{G}_j = J^{-1} \begin{bmatrix} (\mu + \mu_t/\sigma_k) \frac{\partial \xi_j}{\partial x_k} \frac{\partial k}{\partial x_k} \\ (\mu + \mu_t/\sigma_\epsilon) \frac{\partial \xi_j}{\partial x_k} \frac{\partial \epsilon}{\partial x_k} \end{bmatrix}$$

and \hat{S}_C and \hat{S}_{G-F} are the source terms in the Chien (2.2.17, 2.2.18) and Grasso-Falconi (2.2.26, 2.2.27) models:

$$\hat{S}_C = J^{-1} \begin{bmatrix} \mathcal{P}_k - \mathcal{D}_k - \frac{2\mu k}{y^2} \\ \mathcal{P}_\epsilon - \mathcal{D}_\epsilon - \frac{2\mu \epsilon}{y^2} \exp(-0.5y^+) \end{bmatrix}; \quad (2.3.64)$$

$$\hat{S}_{G-F} = J^{-1} \begin{bmatrix} \mathcal{P}_k - \mathcal{D}_k + \Pi_{c,1} + \Pi_{c,2} + \Pi_{c,3} \\ \mathcal{P}_\epsilon - \mathcal{D}_\epsilon \end{bmatrix}.$$

Equation (2.3.62) can be solved numerically using the implicit algorithm proposed by Sahu and Danberg (1986) and implemented into the NPARC code by Nichols (1990). Making use of Euler backward time-differencing, and assuming locally constant transport coefficients, the Beam-Warming algorithm can be written as

$$\begin{aligned} \left(I + \Delta t^n \left[\frac{\partial}{\partial \xi_j} \hat{A}_j^n - \frac{\partial}{\partial \xi_j} \hat{R}_j^n - \hat{T}^n \right] \right) \Delta \hat{Q}^n = \\ -\Delta t^n \left(\frac{\partial \hat{F}_j^n}{\partial \xi_j} - \frac{1}{Re} \left[\frac{\partial \hat{G}_j^n}{\partial \xi_j} + \hat{S}^n \right] \right) \end{aligned} \quad (2.3.65)$$

where

$$\Delta \hat{Q}^n = \hat{Q}^{n+1} - Q^n, \quad \hat{A}_j = \frac{\partial \hat{F}_j}{\partial \hat{Q}}, \quad \hat{R}_j = \frac{\partial}{\partial \hat{Q}} \left(\frac{\hat{G}_j}{Re} \right), \quad \hat{T} = \frac{\partial}{\partial \hat{Q}} \left(\frac{\hat{S}}{Re} \right). \quad (2.3.66)$$

If first-order backward differences (based on the sign of the eigenvalues of the flux terms) are used to estimate the convective spatial derivatives, and second-order central-differences are used to approximate the viscous spatial derivatives in equation (2.3.65), the resulting algorithm is second-order accurate in space and first-order accurate in time.

In the axisymmetric domain equation (2.3.65) can be written as

$$\frac{\partial \hat{Q}}{\partial t} + \frac{\partial \hat{F}_1}{\partial \xi} + \frac{\partial \hat{F}_2}{\partial \eta} = \frac{1}{Re} \left(\frac{\partial \hat{G}_1}{\partial \xi} + \frac{\partial \hat{G}_2}{\partial \eta} + \hat{S} \right) \quad (2.3.67)$$

and the algorithm in equation (2.3.65) reduces to,

$$\begin{aligned} \left(I + \Delta t^n \left[\frac{\partial}{\partial \xi} \hat{A}_1^n + \frac{\partial}{\partial \eta} \hat{A}_2^n - \frac{\partial}{\partial \xi} \hat{R}_1^n - \frac{\partial}{\partial \eta} \hat{R}_2^n - \hat{T}^n \right] \right) \Delta \hat{Q}^n \\ = -\Delta t^n \left(\frac{\partial \hat{F}_1^n}{\partial \xi} + \frac{\partial \hat{F}_2^n}{\partial \eta} - \frac{1}{Re} \left[\frac{\partial \hat{G}_1^n}{\partial \xi} + \frac{\partial \hat{G}_2^n}{\partial \eta} + \hat{S}^n \right] \right). \end{aligned} \quad (2.3.68)$$

Equation (2.3.68) yields a sparse block-pentadiagonal system whose inversion is extremely expensive. Making use of approximate factorization, the above system

can be replaced by a series of block-tridiagonal operators as follows:

$$\begin{aligned} & \left(I + \Delta t \left[\frac{\partial}{\partial \xi} \hat{A}_1^n - \frac{\partial}{\partial \xi} \hat{R}_1^n \right] \right) \left(\{I - \Delta t \hat{T}^n\} + \Delta t \left[\frac{\partial}{\partial \eta} \hat{A}_2^n - \frac{\partial}{\partial \eta} \hat{R}_2^n \right] \right) \Delta \hat{Q}^n \\ & = -\Delta t \left(\frac{\partial \hat{F}_1^n}{\partial \xi} + \frac{\partial \hat{F}_2^n}{\partial \eta} - \frac{1}{Re} \left[\frac{\partial \hat{G}_1^n}{\partial \xi} + \frac{\partial \hat{G}_2^n}{\partial \eta} + \hat{S}^n \right] \right). \end{aligned} \quad (2.3.69)$$

If the spatial derivatives are replaced by finite differences, equation (2.3.69) yields the following algorithm:

$$\begin{aligned} & \left(I + \Delta t \left[\nabla_\xi \hat{A}_1^n - \delta_\xi \hat{R}_1^n \right] \right) \Big|_{j,k} \Delta \hat{Q}^* \Big|_{j,k} = \widehat{RHS}_{(2.3.69)}^n \Big|_{j,k} \\ & \left(\{I - \Delta t \hat{T}^n\} + \Delta t \left[\nabla_\eta \hat{A}_2^n - \delta_\eta \hat{R}_2^n \right] \right) \Big|_{j,k} \Delta \hat{Q}^n \Big|_{j,k} = \Delta \hat{Q}^* \Big|_{j,k} \end{aligned} \quad (2.3.70)$$

$$\hat{Q}^{n+1} \Big|_{j,k} = \hat{Q}^n \Big|_{j,k} + \Delta \hat{Q}^n \Big|_{j,k}$$

where the $\widehat{RHS}_{(2.3.69)}^n \Big|_{j,k}$ is discretized using an upwind scheme proposed by Gorski *et al.* (1985), δ is the central difference operator, and ∇ is the first-order backward difference operator based on the sign of the eigenvalue of the flux terms. In the NPARC code, the block tridiagonal systems that result from (2.3.70) are solved using a block version of the Thomas algorithm.

2.3.3 Grid adaptation algorithm

The need to describe numerous flow features (some characterized by discontinuous distributions of the conservation variables) with the least number of grid points led to the use of grid adaptation methods in this investigation. In particular, we made use of the Self-Adapting-Grid Evolution method (SAGE) developed by Nakahashi and Deiwert (1985) and expanded by Davies and Venkatapathy (1992).

The method is based on a three-sided, spring system analogy, that sets the distance between consecutive points inversely proportional to the gradient of some flow variable. For example,

$$\frac{1}{\Delta x_{i,j}} \sim K_{i,j} \sim \frac{\partial \rho}{\partial x_{i,j}}. \quad (2.3.71)$$

The one-sided contribution of a torsional spring, $T_{i,j}$, enforces smoothness and orthogonality constraints (see Figure 2.1). Given that the method is based on a three-sided spring system, the adaptation can be advanced in one index (e.g., i) along lines of constant value for the other index (e.g., j). This leads to a scalar parabolic system that avoids the computational expense that results from the elliptic, four-spring systems (see Figure 2.1).

In this investigation, $\partial \rho / \partial r$ was used as the adaptation gradient to cluster points in the r -direction, and $\partial \rho / \partial x$ or $\partial p / \partial x$ were used to cluster points in the x -direction. For a simulation, the process of grid adaptation took several steps:

1. A solution was obtained on a poorly distributed mesh starting from a poor initial guess.
2. Based on the computed solution, the first line of points off a solid boundary was clustered at $y^+ \simeq 1$. This was followed by two adaptation passes over the mesh — the first in the x -direction (adapting the y location of the points) followed by a second pass in the y -direction (adapting the x location of the points).
3. The available solution was interpolated into the newly adapted mesh.
4. A new solution was computed in the new mesh using the interpolated, old solution as the initial guess.
5. The process was repeated starting from step 2.

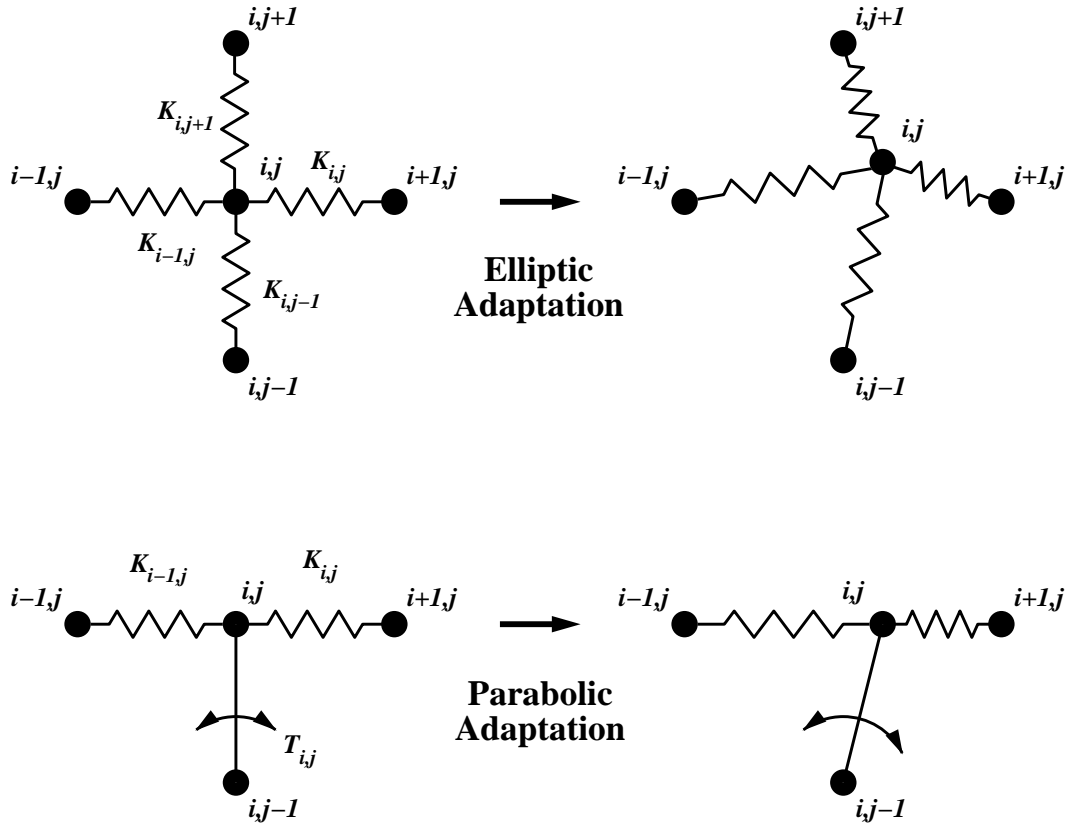


Figure 2.1: Schematic comparison between an elliptic, four-spring and a parabolic, three-spring grid adaptation method.

This cycle of flow-computation \Leftrightarrow grid-adaptation was repeated (typically about three times) until no noticeable change was observed between consecutive grids.

Chapter 3

Evaluation of Turbulence Models

As an initial step in this investigation, the performance of the turbulence models presented in the previous chapter was evaluated by simulating the boundary layer over a flat plate with zero pressure gradient at free-stream Mach numbers of 0.2, 1.2, and 4.0. The data obtained for the $M_{\text{inf}} = 0.2$ case was compared to the direct numerical simulation (DNS) data of Spalart (1988) for a momentum thickness based Reynolds number, $R_\theta = 1410$. For the simulations at $M_{\text{inf}} = 1.2$ and 4.0, results at $R_\theta = 14000$ are compared with the compressible law of the wall.

3.1 Physical domain and boundary conditions

The computational domain used in these simulations is schematically shown in Figure 3.1. This domain was discretized, depending on the free-stream Mach number, into one of two meshes: one that used 111×81 points (in the streamwise and spanwise directions, respectively) for $M = 0.2$, or one with 206×81 points for $M = 1.2$ and 4.0. Inside the computational domain, the placement of the mesh points was stretched both in the streamwise and spanwise directions, using

hyperbolic tangent distributions that increased the size of the grid spacing away from the leading edge of the flat plate (see Figure 3.2). Over the flat plate, the first line of points parallel to the wall was forced to be located at $y^+ = y u_\tau / \nu_{wall} \sim 0.5$ to obtain accurate resolution of the wall layer.

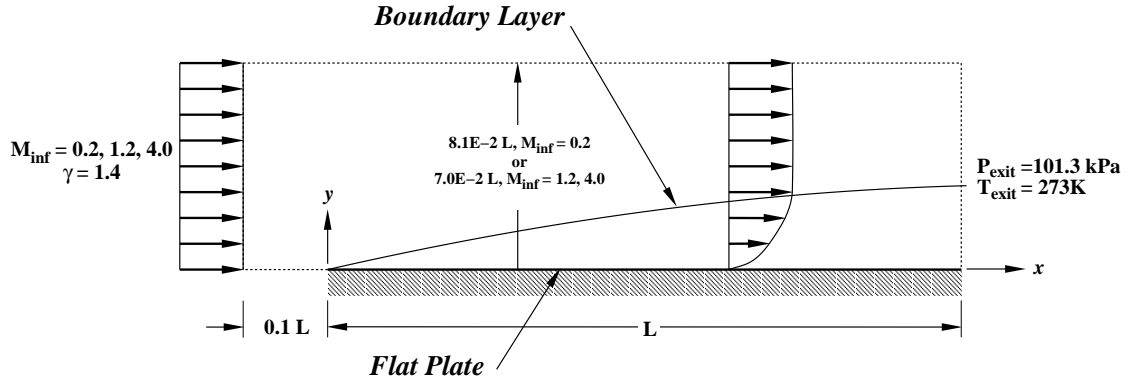


Figure 3.1: Computational domain used for the simulation of the boundary-layer (vertical axis not shown to scale; $L = 0.5\text{ m}$).

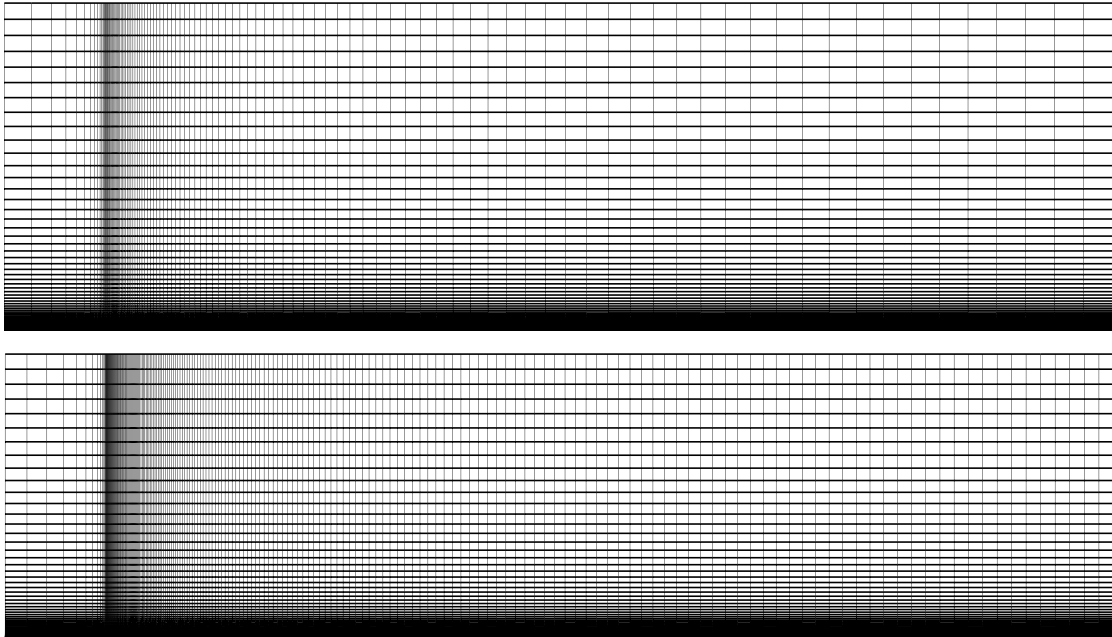


Figure 3.2: Computational meshes used for the simulation of the boundary-layer. TOP: for $M_{inf} = 0.2$; BOTTOM: for $M_{inf} = 1.2$ and 4.0 (vertical scale shown at four times its original size).

Characteristic-type boundary conditions were used at the inlet of the computa-

tional domain for the subsonic free-stream case (P_o, T_o specified), whereas inlet conditions were fixed for the supersonic free-stream cases. At the outlet, characteristic type boundary conditions were used (P_{exit}, T_{exit} specified) in all cases. The top end of the computational domain was treated as a slip-wall for the subsonic case, while homogeneous Neumann boundary conditions were applied for the supersonic cases. At $y = 0$, slip-wall boundary conditions were used before the leading edge of the flat plate (*i.e.*, $x < 0$), and adiabatic no-slip boundary conditions over the plate ($x \geq 0$).

3.2 Subsonic boundary-layer

The first test of the performance of the turbulence models described in Chapter 2 was conducted by modeling the subsonic flow over a flat plate for $R_\theta = 1410$. Figure 3.3 compares the compressible law of the wall

$$u^+ = \begin{cases} y^+ & \text{for } y^+ \leq 5 \\ \log y^+ / 0.41 + 5 & \text{for } y^+ > 10 \end{cases} \quad (3.2.1)$$

with the streamwise velocity predictions obtained using DNS (Spalart 1988), and the results of the three eddy-viscosity turbulence models. As seen in the figure, the Baldwin-Lomax model (1978) predicted the DNS streamwise velocity distribution with satisfactory accuracy, yielding a value of wall friction velocity, $u_\tau = \sqrt{\tau_{wall} / \rho_{wall}}$, only 2.7% lower than its DNS counterpart despite a discontinuity in the first derivative of the eddy-viscosity distribution at $y/\delta \approx 0.155$ (or $y^+ \approx 85$, see Figure 3.4). This discontinuity results from the switching between the inner and outer formulations of the model as seen in equation (2.2.11).

The Chien k - ϵ model (1982) predicted the velocity distribution of this boundary layer extremely well, as seen in Figure 3.3, with its prediction of friction velocity

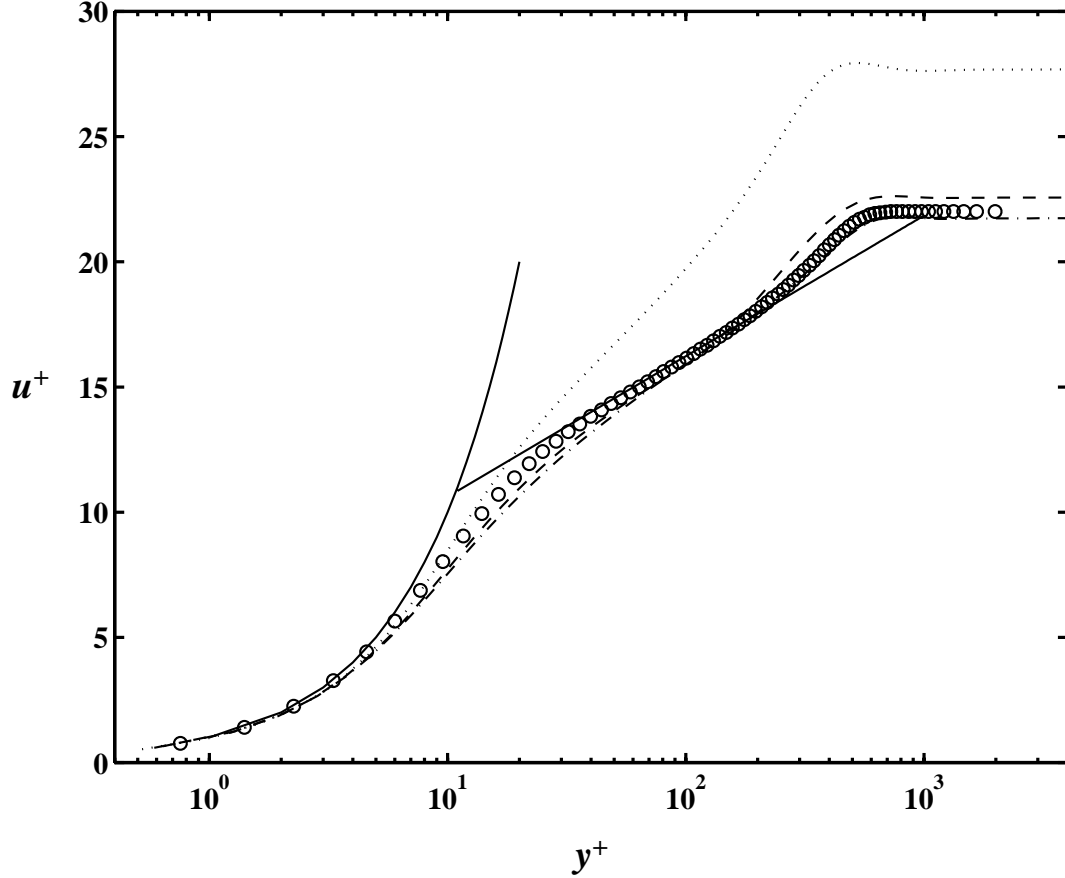


Figure 3.3: Effect of turbulence model on the streamwise velocity distribution of a boundary layer, $R_\theta = 1410$, $M_{\text{inf}} = 0.2$. — : law of the wall, equation (3.2.1); \circ : Spalart's DNS (1988); --- : Baldwin-Lomax model; -.-.- : Chien's k - ϵ model; : Grasso-Falconi's k - ϵ model.

deviating only 0.9% from the DNS results. Figure 3.4 shows that the Chien k - ϵ model yields a smooth distribution of eddy-viscosity which is very similar, for $y/\delta < 1$, to the one calculated using the distributions of $\overline{u'v'}$ and $d\bar{u}/dy$ obtained from the DNS. The DNS and the Chien k - ϵ results deviate from each other for $y/\delta > 1$. This deviation is mostly due to the fact that in this range, the DNS data for $d\bar{u}/dy$ tends to zero, making small contributions in $\overline{u'v'}$ lead to large contributions in the eddy-viscosity. The prediction of turbulent kinetic energy is almost identical to that of the DNS (see Figure 3.5) with the peak in the distribution being underpredicted by 7% and its location moving away from the wall by about 5 wall units (see insert

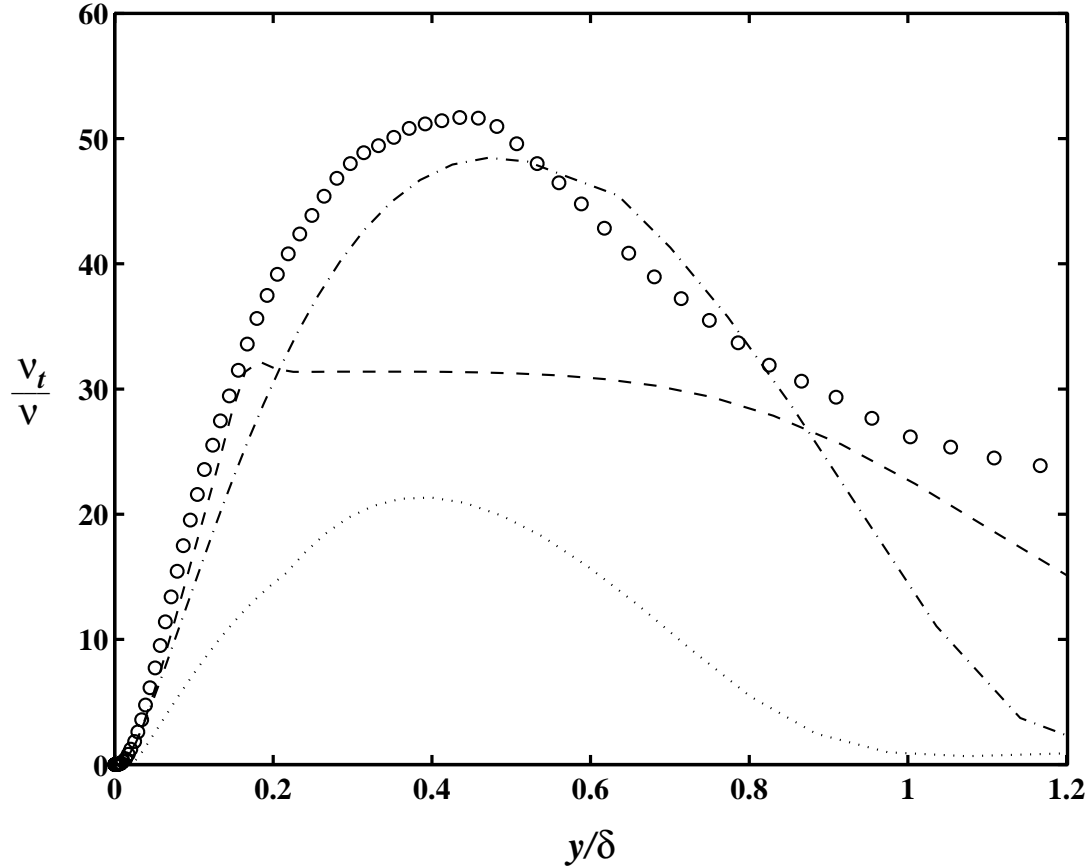


Figure 3.4: Effect of turbulence model on the eddy-viscosity distribution of a boundary layer, $R_\theta = 1410$, $M_{\text{inf}} = 0.2$. \circ : Spalart’s DNS (1988), $\nu_t = \overline{u'v'}/d\bar{u}/dy$; --- : Baldwin-Lomax model; -.-.- : Chien’s $k-\epsilon$ model; : Grasso-Falconi’s $k-\epsilon$ model.

in Figure 3.5).

The prediction of the modified turbulent kinetic energy dissipation rate, ϵ ,¹ obtained by the Chien $k-\epsilon$ model (—·—· line in Figure 3.6), appears to be in agreement with the DNS predictions of Spalart (1988) for $y^+ \gtrsim 40$. Closer to the wall, the prediction deviates from the DNS results in order to satisfy the homogeneous Dirichlet boundary conditions applied to ϵ at the wall by this model (see section 2.2.2 in Chapter 2). However, due to the contribution of the “wall” dissipation, $D = 2\nu k/y^2$, the true turbulent kinetic energy dissipation rate ($\epsilon + D$, — line in

¹Termed “isotropic” dissipation by Chien (1982).

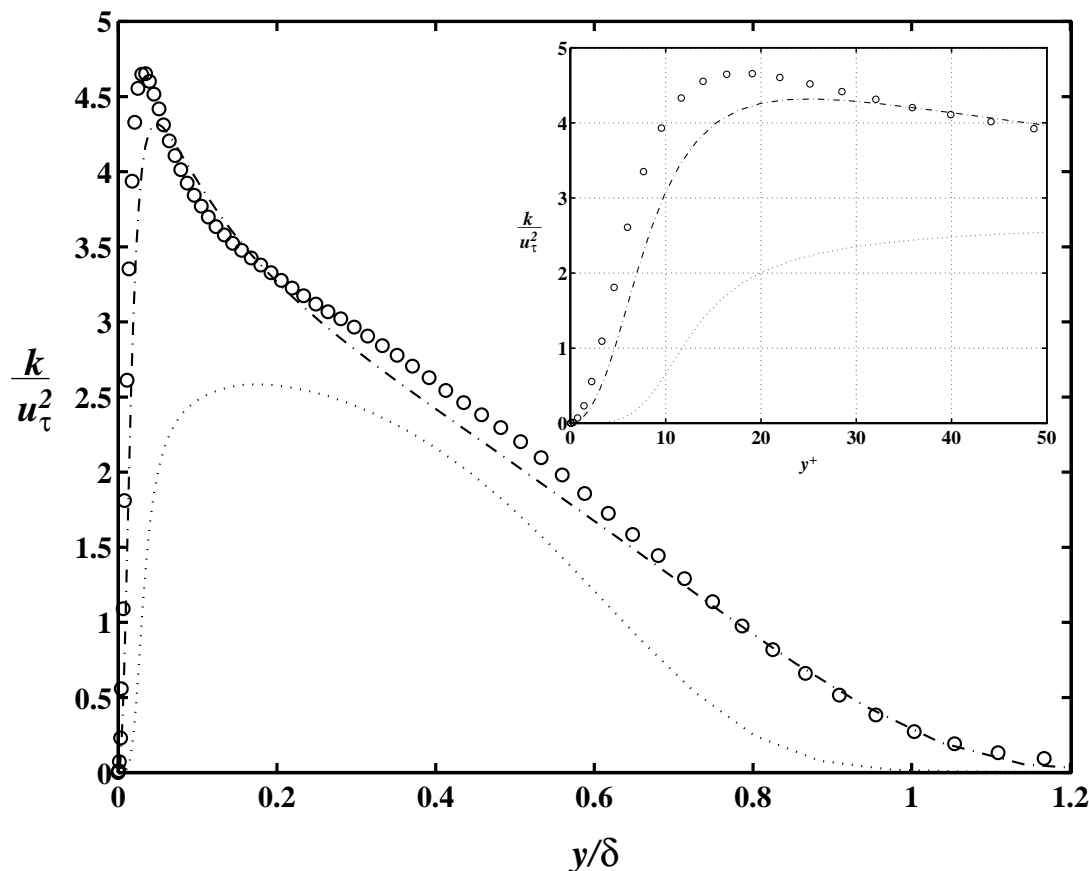


Figure 3.5: Effect of turbulence model on the turbulent kinetic energy distribution of a boundary layer, $R_\theta = 1410$, $M_{\text{inf}} = 0.2$. \circ : Spalart's DNS (1988); $-\cdot-\cdot-$: Chien's k - ϵ model; \cdots : Grasso-Falconi's k - ϵ model.

INSERT: near-wall detail.

Figure 3.6), is in agreement with the DNS data for $y^+ \gtrsim 7$. Very close to the wall, $y^+ \lesssim 7$, the prediction of the true dissipation rate exhibits a slope of opposite sign to that seen in the Spalart (1988) results. This deviation indicates that the “wall” dissipation model used by Chien (1982) needs refinement to describe the physics of the flow in the viscous sublayer.

The viscous sublayer deviation in the prediction of dissipation rate by the Chien k - ϵ model raises the question of why the prediction of eddy-viscosity is in good agreement in this region. The answer can be found in the error in the prediction of k near the wall. Figure 3.7 compares the near-wall results of the Chien k - ϵ

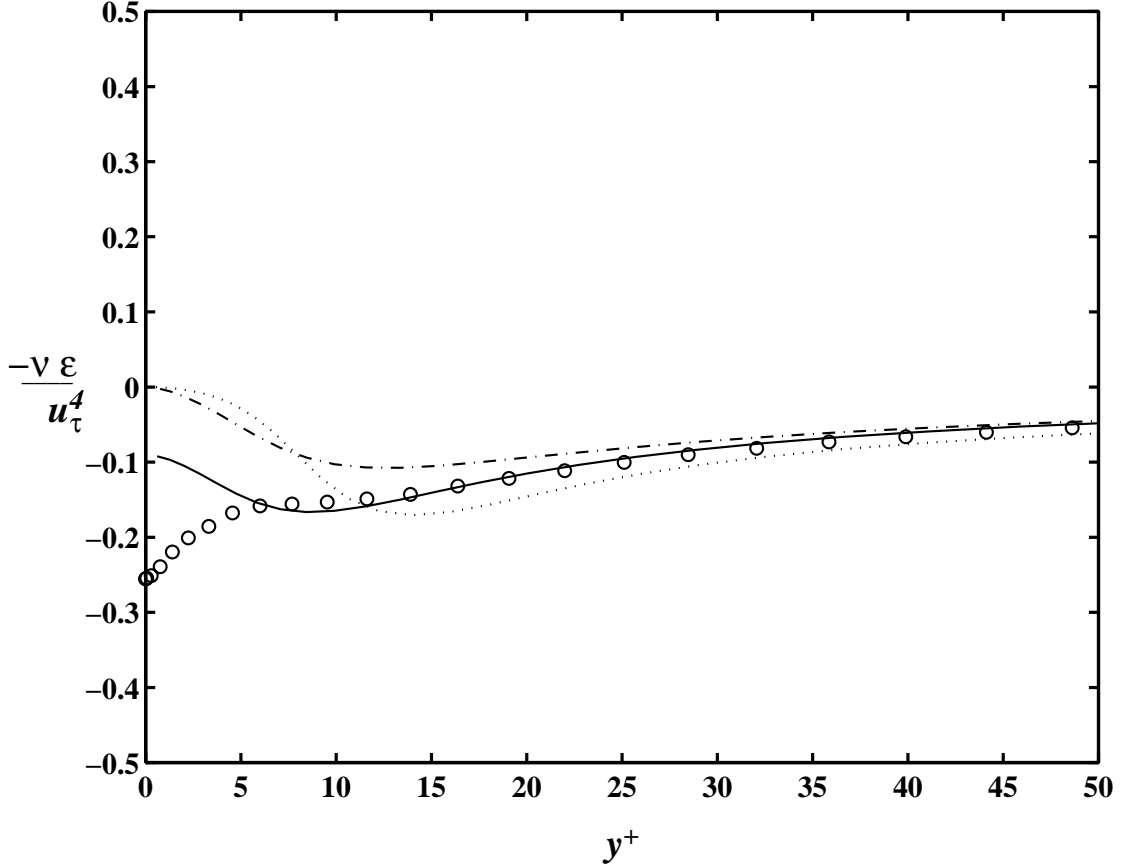


Figure 3.6: Effect of turbulence model on the near-wall turbulent kinetic energy dissipation rate distribution of a boundary layer, $R_\theta = 1410$, $M_{\text{inf}} = 0.2$. \circ : Spalart's DNS (1988); $-\cdot-\cdot-$: Chien's k - ϵ model (ϵ only); $—$: Chien's k - ϵ model ($\epsilon + D$); \cdots : Grasso-Falconi's k - ϵ model.

model for k^2 , ϵ , and ν_t , with data from Spalart (1988). As seen in the figure, for $2 < y^+ < 10$, the error in the prediction of the dissipation rate, ϵ , is nearly inversely proportional to the square of the error in the prediction of turbulent kinetic energy, k^2 . Thus, in equation (2.2.22), the two errors cancel and this leads to a good prediction of eddy-viscosity by the Chien k - ϵ model. Very close to the wall, $y^+ < 2$, k vanishes, making the error in the prediction of ϵ of little significance to the prediction of eddy-viscosity.

The trends here described appear to hold true regardless of the definition of eddy-viscosity used to process the DNS data. Figure 3.7 (BOTTOM CENTER) also

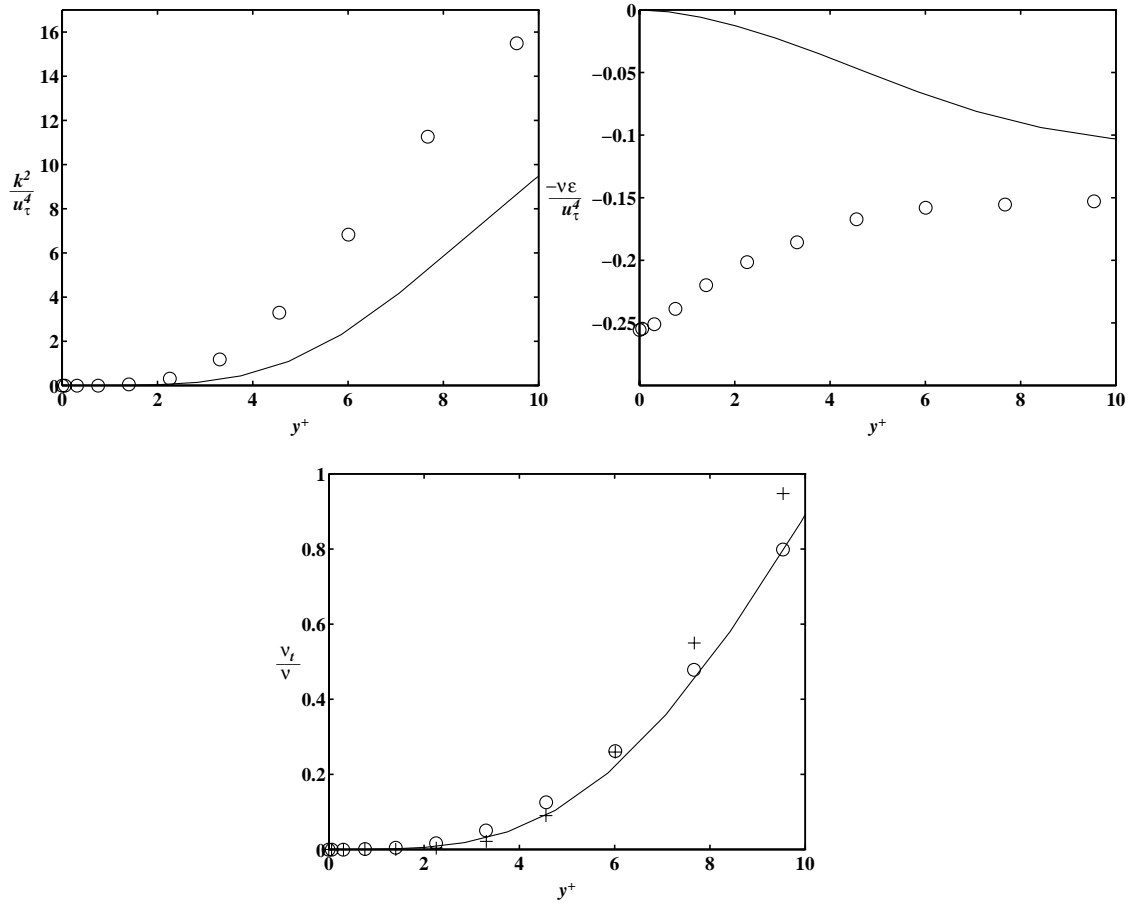


Figure 3.7: Performance of the Chien $k-\epsilon$ model near-wall of a boundary layer, $R_\theta = 1410$, $M_{\text{inf}} = 0.2$. TOP LEFT, turbulent kinetic energy distribution (square power), \circ : Spalart's DNS (1988); --- : Chien's $k-\epsilon$ model. TOP RIGHT, distribution of turbulent kinetic energy dissipation rate, \circ : Spalart's DNS (1988); --- : Chien's $k-\epsilon$ model. BOTTOM CENTER, eddy-viscosity distribution, \circ : Spalart's DNS (1988), $\nu_t = \overline{u'v'}/d\bar{u}/dy$; $+$: Spalart's DNS (1988), $\nu_t = C_\mu f_\mu k^2/\epsilon$; --- : Chien's $k-\epsilon$ model.

shows the prediction of eddy-viscosity that is obtained if one processes the DNS k and ϵ data using the Chien definition for ν_t (*i.e.*, equation 2.2.22; see +’s in the figure). As seen in the figure, the data computed using the Chien model and the distribution obtained using $\nu_t = \overline{u'v'}/d\bar{u}/dy$ are in good agreement, the Chien model yielding slightly lower values of ν_t for $y^+ < 6$ and slightly higher values for $y^+ > 6$. This leads us to believe that the definition of ν_t used by the Chien k - ϵ model (equations 2.2.22 and 2.2.23) provides a good description of the dynamics in the near-wall region.

In contrast to the Chien k - ϵ model results, the results obtained using the Grasso-Falconi model (1993) were less than desirable for this subsonic boundary layer. The model underpredicted the friction velocity by 21.3%, increasing the slope of the log region as seen in Figure 3.3. Problems with the model are also apparent in the eddy-viscosity distribution (see Figure 3.4), where the distribution peaks at a value 59% lower than the DNS prediction and 56% lower than the Chien k - ϵ model estimate. The distribution of turbulence kinetic energy, Figure 3.5, is also grossly underpredicted with the peak having a magnitude of only 55% of the DNS result. Furthermore, the shape of the k distribution is in disagreement with the DNS data, smoothing the sharp peak near the wall into a hump. Finally, the problems seen above extend into the turbulent dissipation rate distribution (Figure 3.6), where the Grasso-Falconi results are slightly larger in magnitude than the Spalart results for $y^+ \lesssim 12$, while they grossly underpredict the magnitude of ϵ near the wall.

The near-wall deviation of ϵ in the Grasso-Falconi model can be explained by the absence of “wall” dissipation terms in equations (2.2.26 and 2.2.27), which leads to an erroneous near-wall estimation of k (see line in Figure 3.5 insert for $y^+ \lesssim 5$). As explained by Chien (1982), the molecular dissipation of k is finite at

$y = 0$ given that near the wall, $k \sim y^2$, and thus

$$\frac{\partial}{\partial y} \left(\mu \frac{\partial k}{\partial y} \right) > 0. \quad (3.2.2)$$

The lack in the Grasso-Falconi model of a term that represents the true finite rate of dissipation at the wall prevents the homogeneity of the k equation at the wall, given that ϵ vanishes at the wall for all initial conditions. Thus, the k equation is arranged to yield a non-homogeneous value of k at the wall which is then forced to be homogeneous by its boundary condition. This leads to an erroneous description of the physics of the viscous sublayer by this model.

A study of the reasons why the Grasso-Falconi model fails to accurately predict the flow features of this subsonic boundary layer is beyond the scope of this work. Among other things, the Chien and Grasso-Falconi models differ in:

- Turbulent Prandtl numbers — σ_k : 1.0 *vs.* 1.55; σ_ϵ : 1.3 *vs.* 2.0.
- Turbulent dissipation rate, production and dissipation constants — $C_{\epsilon 1}$: 1.35 *vs.* 1.60; $C_{\epsilon 2}$: 1.8 *vs.* $1.83[1 - (2/9) \exp(-Re_t^2/36)]$.
- Wall damping functions — f_2 : (2.2.21) *vs.* (2.2.29); f_μ : (2.2.23) *vs.* (2.2.35).
- Pressure dilatation contribution — $(-\rho \epsilon M_t^2 Re)$ *vs.* $(0.2 \rho \epsilon M_t^2 Re)$.

However, it is worth mentioning that the Grasso-Falconi model has been shown to perform better than the Chien model in the hypersonic regime (Grasso and Falconi, 1993). This improvement in performance with increased compressibility will be shown to hold for the results of the supersonic boundary layer presented in the next section.

3.3 Supersonic boundary-layer

Given that the flows of interest to this investigation cover a wide dynamic range of velocities, it is necessary to evaluate the performance of the turbulence models over a wide range of Mach numbers. Previous research in the area of gas-only flows in gas-metal atomization (Espina *et al.*, 1993) indicates that in the bulk of the flow the Mach number varies in a range from 0 to 4. Therefore, this section reviews the performance of the turbulence models evaluated in the previous section when used to model a supersonic boundary layer at $M_{\text{inf}} = 1.2$ and 4.0.

Figure 3.8 compares the streamwise velocity distributions predicted by the three selected models against the compressible law of the wall – (3.2.1). As was the case for the $M_{\text{inf}} = 0.2$ boundary layer, the Baldwin-Lomax and the Chien k - ϵ models predict the shape of the velocity distribution accurately, while the Grasso-Falconi model underpredicts the shear stress at the wall, leading to a low friction velocity value, which, in turn, increases the slope of the log region.

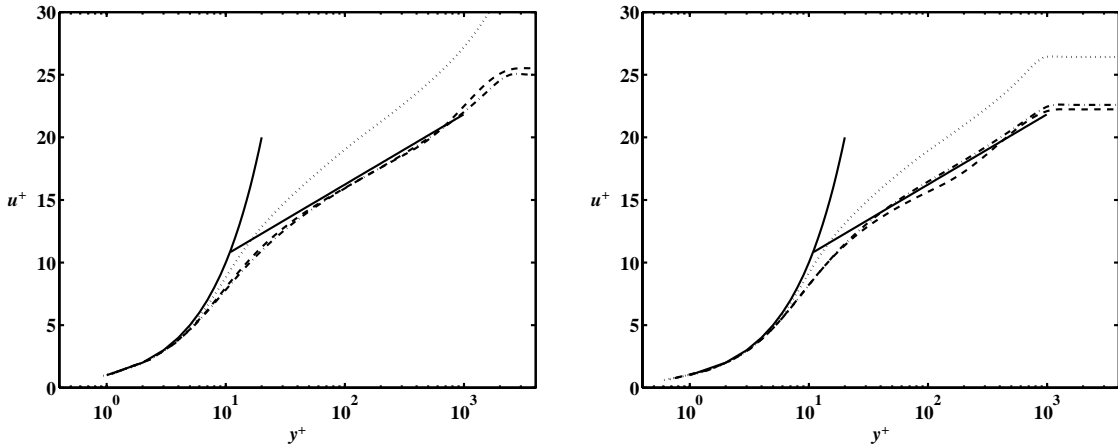


Figure 3.8: Effect of turbulence model on the streamwise velocity distribution of a boundary layer, $R_\theta = 14000$; LEFT: $M_{\text{inf}} = 1.2$; RIGHT: $M_{\text{inf}} = 4.0$. — : law of the wall; --- : Baldwin-Lomax model; -.-.- : Chien’s k - ϵ model; : Grasso-Falconi’s k - ϵ model.

The eddy-viscosity distribution, Figure 3.9, shows that the location of the switch between the inner and outer formulations of the Baldwin-Lomax model moves closer to the wall with increasing free-stream Mach number. From the switching point on, the eddy-viscosity tends to increase, leading to a maximum just under $y/\delta = 1$, and then decays outside the boundary layer. This is in contrast to the $k-\epsilon$ models, which yield rapid decays in the eddy-viscosity distribution inside the boundary layer leading to vanishing μ_t by $y/\delta = 1$. It is apparent from Figure 3.9 that with increasing free-stream Mach number, the eddy-viscosity predictions of the Baldwin-Lomax model are in better agreement with the predictions of the Chien $k-\epsilon$ model.

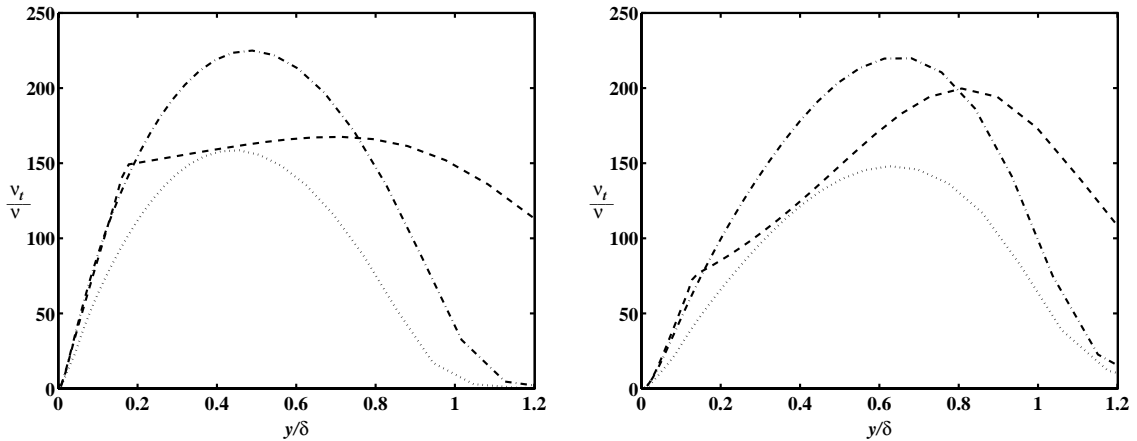


Figure 3.9: Effect of turbulence model on the eddy-viscosity distribution of a boundary layer, $R_\theta = 14000$; LEFT: $M_{\text{inf}} = 1.2$; RIGHT: $M_{\text{inf}} = 4.0$. --- : Baldwin-Lomax model; -.- : Chien's $k-\epsilon$ model; : Grasso-Falconi's $k-\epsilon$ model.

From Figure 3.9, it can also be seen that at these supersonic free-stream velocities, the predictions obtained by the Chien and Grasso-Falconi models are in less disagreement than they appeared to be for the subsonic case. It is noticeable that the peak in the Chien's eddy-viscosity distribution reaches a maximum in the neighborhood of $225 \nu_t/\nu$, which appears to be independent of M_{inf} . However, this peak moves away from the wall with increasing Mach number, leading to a

more rapid decay of the eddy-viscosity in the wake region of the boundary layer for increasing free-stream velocities.

The turbulent kinetic energy distributions predicted by the Chien and Grasso-Falconi models are also in better agreement at these supersonic free-stream velocities (see Figure 3.10) than they appeared to be at $M_{\text{inf}} = 0.2$. With the increase in speed, the Grasso-Falconi model starts yielding a peak close to the wall, although its magnitude is in disagreement with the Chien model prediction. Overall, there is a tendency for the turbulent kinetic energy, in both models, to decrease with increasing free-stream velocity. Finally, the turbulent dissipation rate (see Figure 3.11), predicted by the Grasso-Falconi model continues to be somewhat lower than the prediction of Chien true dissipation rate for $y^+ < 10$. However, the lack of “wall” dissipation continues to yield problems for $y^+ > 10$, and unphysically vanishing ϵ at the wall.

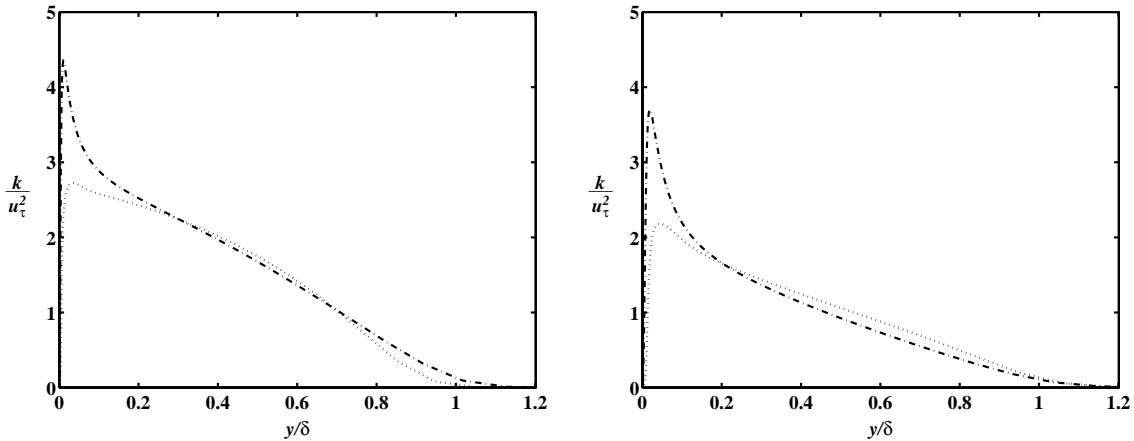


Figure 3.10: Effect of turbulence model on the turbulent kinetic energy distribution of a boundary layer, $R_\theta = 14000$; LEFT: $M_{\text{inf}} = 1.2$; RIGHT: $M_{\text{inf}} = 4.0$. - · - · : Chien’s k - ϵ model; · · · · · : Grasso-Falconi’s k - ϵ model.

As seen, many of the adverse patterns observed in the $M_{\text{inf}} = 0.2$ results obtained with the GF model were also seen in the results of the $M_{\text{inf}} = 1.2$ and 4.0 simulations. Everything considered, the present implementation of the Grasso-Falconi

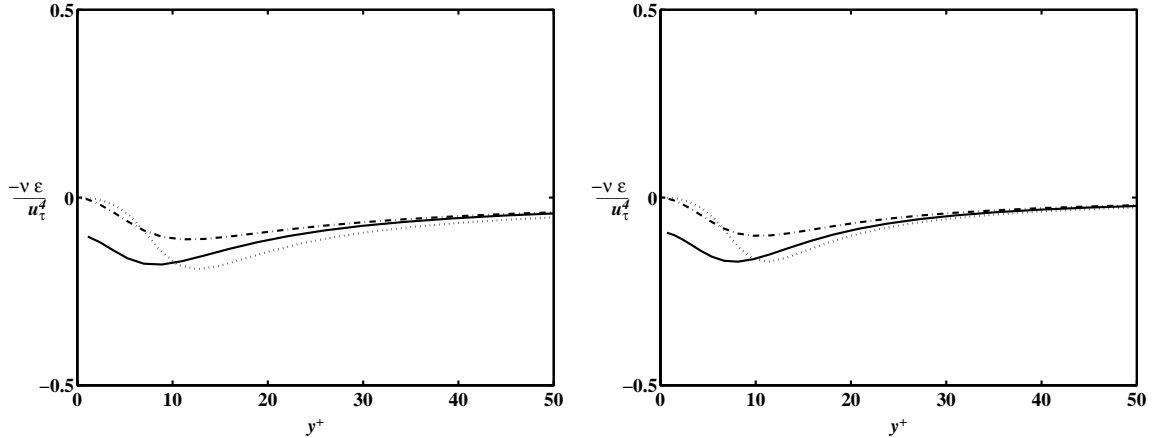


Figure 3.11: Effect of turbulence model on the near-wall turbulent kinetic energy dissipation rate distribution of a boundary layer, $R_\theta = 14000$; LEFT: $M_{\text{inf}} = 1.2$; RIGHT: $M_{\text{inf}} = 4.0$. - - - : Chien's k - ϵ model (ϵ only); — : Chien's k - ϵ model ($\epsilon + D$); ····· : Grasso-Falconi's k - ϵ model.

model continues to have trouble predicting the features of the flow in this range of Mach numbers. This led to the conclusion that the k - ϵ formulation of the Grasso-Falconi model is not sufficiently accurate for flows at $M \leq 4$. For these reasons, the model will not be used in the remainder of this investigation.

3.4 Summary

The strengths and limitations of the NPARC code when used to model compressible boundary layer flows have been assessed. Simulations demonstrated that the Baldwin-Lomax turbulence model (1978) yields reasonable streamwise velocity predictions despite a discontinuity in the first derivative of the eddy-viscosity.

The k - ϵ model by Grasso and Falconi (1993) yielded unsatisfactory results for boundary layers with free-stream Mach numbers in the 0.2 to 4.0 range. The problems seen with this model appear to be due to the lack of “wall” dissipation terms to balance the viscous dissipation of k at the wall. Due to its performance, the k - ϵ model by Grasso-Falconi will not be used in the remaining work of this

investigation.

With attention to discretization details, the k - ϵ model by Chien (1982) rendered results in agreement with DNS data for boundary layer flows. In the next chapter, the performance of both the Baldwin-Lomax and the Chien k - ϵ model will be further studied with the modeling of a compressible base flow.

Chapter 4

Supersonic Base Flow

Axisymmetric base flows have been extensively studied during the last four decades, primarily due to their importance in ballistic problems. In this type of flow, the need to achieve an understanding of the mechanisms that yield reduced pressures at the tails of bullets and missiles has led to theoretical (Mueller 1968, Sule and Mueller 1973, Mueller 1985), numerical (Mikhail *et al.* 1980, Sahu *et al.* 1985, Sahu 1989, Peace 1991, Tucker and Shyy 1993, Sahu 1994), and experimental (Herrin and Dutton 1994) investigations (reviews of the pertinent literature can be found in Mueller 1985, Tucker and Shyy 1993, and Herrin and Dutton 1994). In all cases, attempts have been made to determine ways to control the flow structure in the wake region such that drag due to base pressure is reduced and vehicle stability is increased.

The basic structure of the supersonic base flow is also at the heart of the close-coupled gas-metal atomizer. In an atomizer, control of the base pressure is of utmost importance given that this parameter controls the flow rate of the liquid metal to be processed. The ultimate goal of the materials industry is to produce metal powders of known particle-size distributions with the least amount of gas

and at the lowest jet stagnation pressure possible. Therefore, the results presented in this chapter deviate from the previous base flow research in that its motivation is to determine mechanisms with which to **control** the base drag.

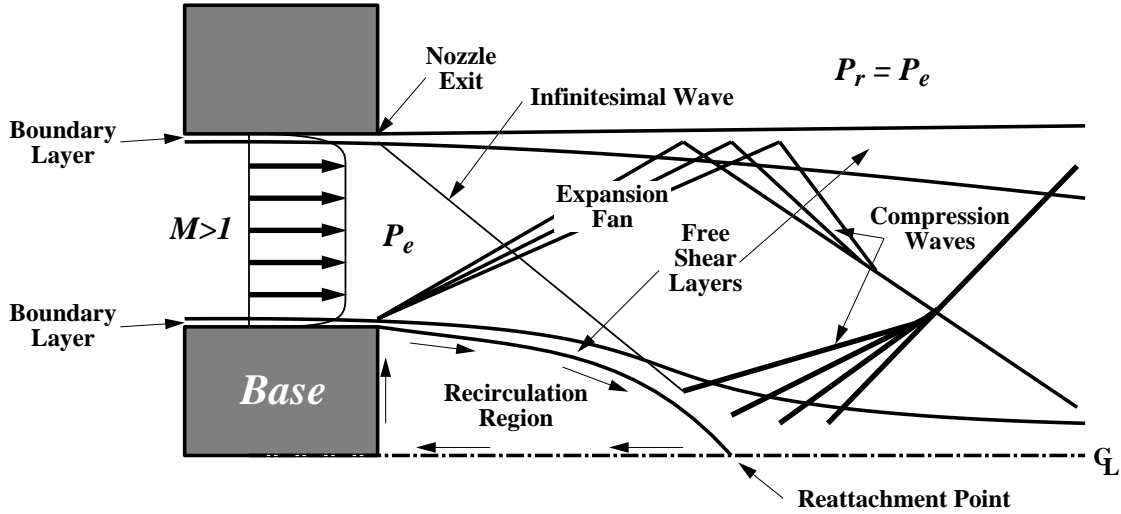


Figure 4.1: Schematic of the axisymmetric base flow produced by the flow of a supersonic annular jet over the end of a circular cylinder (labeled **Base** in the figure).

The base flow structure that results as a supersonic annular jet surrounds the end of a circular cylinder at **design** pressure ratio is schematically shown in Figure 4.1. When the flow emanating from the nozzle encounters the end corner of the cylinder, it undergoes an expansion process to satisfy the surface-angle change imposed by the termination of the cylinder. The flow separates and forms a free shear layer that propagates towards the axis of symmetry of the geometry. The resulting internal shear layer encapsulates a volume of low-speed fluid in the area downstream of the base of the cylinder. At the axis of symmetry, the flow is forced to compress through a series of compression waves to change its direction. The resulting outbound-propagating compression waves collapse into a curved shock wave that propagates away from the axis of symmetry. Meanwhile, the expansion waves generated in the initial expansion fan propagate towards the outer free shear layer of the jet from

which they reflect as compression waves. These waves then collapse into a single curved shock wave that propagates towards the axis of symmetry. Both resulting shock waves will continue to interact further downstream to form a complex jet structure.

Flows similar to the one described above have been studied theoretically and numerically in the past. Mueller (1968), Sule and Mueller (1973), and Mueller (1985) studied the effects of geometry and pressure ratio on base pressure for plug nozzles. Based on experimental data and theoretical considerations, they derived a model capable of predicting the pressure at the base in a number of geometries. Mikhail *et al.* (1980) presented the study of the base flow behind the AGARD 10-deg. nozzle with mass injection at the base. Their results were computed using a 30×39 mesh, which led to poor spatial resolution in the data. Sahu *et al.* (1985, and 1989) presented results for flows over a variety of boattail configurations (with and without mass injection) using a number of different numerical methods. Peace (1991) studied three variations of a circular-arc boattail with mass injection by solving the Navier-Stokes equations with the Baldwin-Lomax and Chien's $k-\epsilon$ turbulence models. These results, which took advantage of grid adaptation methods, revealed that the $k-\epsilon$ predictions are superior to those obtained using the Baldwin-Lomax model. He found good agreement between the numerical and experimental results for attached flow configurations, but both models had trouble predicting the physics of separated flow regions.

Recently, a detailed experimental description of the flow structure in the base area of a cylinder engulfed by a supersonic stream was given by Herrin and Dutton (1994). Their data are the first to contain detailed three-dimensional velocity and turbulence information in the base region obtained by non-intrusive meth-

ods. The availability of these data has spawned numerical investigations by Sahu *et al.* (1994) and Tucker *et al.* (1993) who performed almost identical studies of the flow structure in the base region.

In this chapter, we focus on the validation of numerical techniques to simulate the gas-only flow in gas-metal atomizers by simulating the complete flow field studied by Herrin and Dutton (1994). Although the aforementioned numerical investigations (Sahu *et al.* 1994, and Tucker *et al.* 1993) have studied this test case, they restricted their findings to the near-wake region and gave little detail of the outer jet region, which is of importance in atomization flows.

The results presented here document the differences between the predictions obtained using the zero-equation turbulence model by Baldwin-Lomax (1978) and the two-equation turbulence model by Chien (1982) (as implemented by Georgiadis *et al.*, 1994). Also discussed are a few modifications to the NPARC code (Cooper, 1989) dealing with the implementation of the Baldwin-Lomax model. In addition, this work analyzes the base flow structure that results when the annular gas jet is operated at off-design pressure ratios; emphasis is placed on under-expanded pressure ratios that encompass the predominant regime at which gas-metal atomizers are operated.

4.1 Physical domain and boundary conditions

The computational domain used (see Figure 4.2) follows the specifications of the supersonic tunnel used by Herrin and Dutton (1994) as described by Lilienthal *et al.* (1970) and Sauter and Dutton (1989). Although Herrin and Dutton's (1994) data provides the approaching velocity and turbulence intensity distributions near the edge of the circular cylinder, our interest in a physical description of the outer

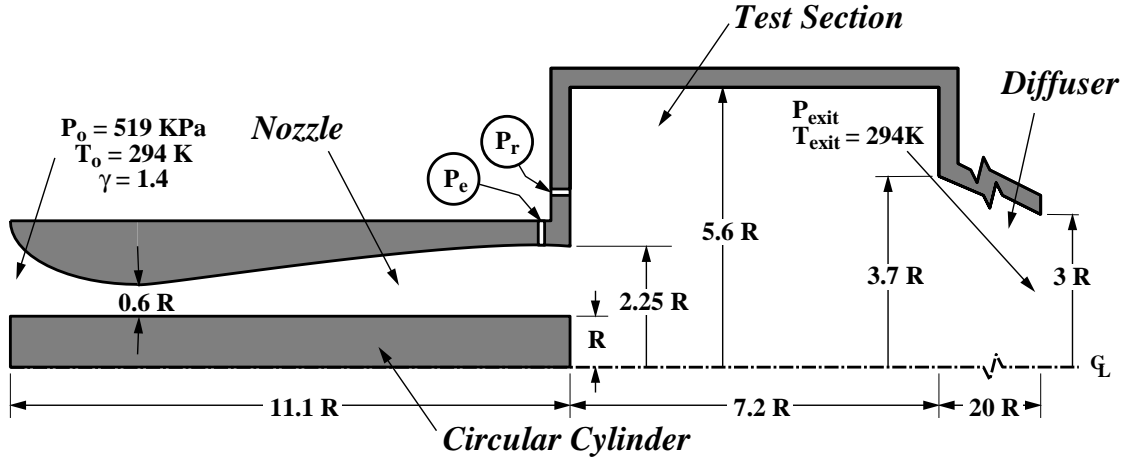


Figure 4.2: Schematic diagram of the computational domain used in the base flow problem.

shear layer of the flow encapsulating the base region prompted us to simulate nearly the entire wind tunnel including the nozzle, the test section, and the diffuser.

Taking the wind tunnel diffuser into consideration was of particular importance for this simulation. It was found that without its addition to the computational domain, instabilities arising in the subsonic portion of the exit boundary condition propagated upstream into the base flow area, distorting the desired solution. The additional length of the diffuser buffered the test section from the boundary conditions, dissipating any instability along its length.

The computational domain was segmented into three separate blocks: the nozzle (266×81 points in the axial and radial directions respectively), the test section (255×279), and the diffuser (338×125). Within each block, the mesh points were distributed using the SAGE grid adaptation program (Davies and Venkatapathy, 1992). At all solid boundaries, the first line of points parallel to the wall was forced to be located at $y^+ \simeq 1$ to obtain accurate resolution at the wall layer. The final adapted grid used in one of the tested flows is shown in Figure 4.3.

Characteristic type boundary conditions were used at the inlet of the nozzle (P_o ,

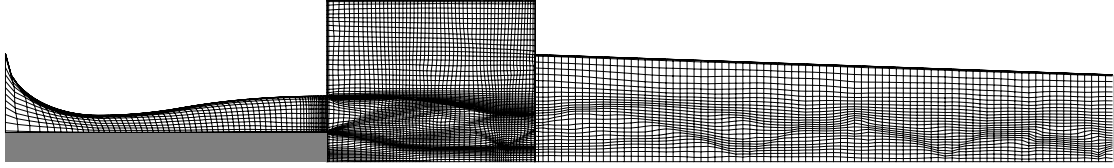


Figure 4.3: Computational mesh adapted for simulation of base flow at the design pressure ratio (only every fourth grid line is shown for clarity).

T_o specified) and at the outlet of the diffuser (P_{exit} , T_{exit} specified). The interface between the nozzle and the test section blocks as well as the interface between the test section and the diffuser blocks were interpolated explicitly. Axisymmetry was used at the axes of the test section and the diffuser blocks while all other boundaries were treated as adiabatic, no-slip walls.

4.2 The nozzle flow

As mentioned before, the need for a physical description of the outer edge of the nozzle exit profile prompted the simulation of the entire annular nozzle flow. This approach, which is different from previous numerical investigations (Sahu *et al.* 1994, Tucker *et al.* 1993), yielded an exit velocity and turbulence distributions which agree with the experimental data near the wall of the circular cylinder as seen in Figure 4.4.

The streamwise velocity distribution (Figure 4.4, top) reveals a fully developed turbulent profile at the exit of the nozzle that, although in agreement with the law of the wall, deviates from the experimental results. This discrepancy could be the result of an error in the estimation of the experimental friction velocity ($u_{\tau,exp} = 21.2 \text{ m/s}$), which could not be measured directly due to resolution constraints; its value was obtained following the method proposed by Sun and Childs (1973). The figure also includes the experimental data normalized by the numerical value for

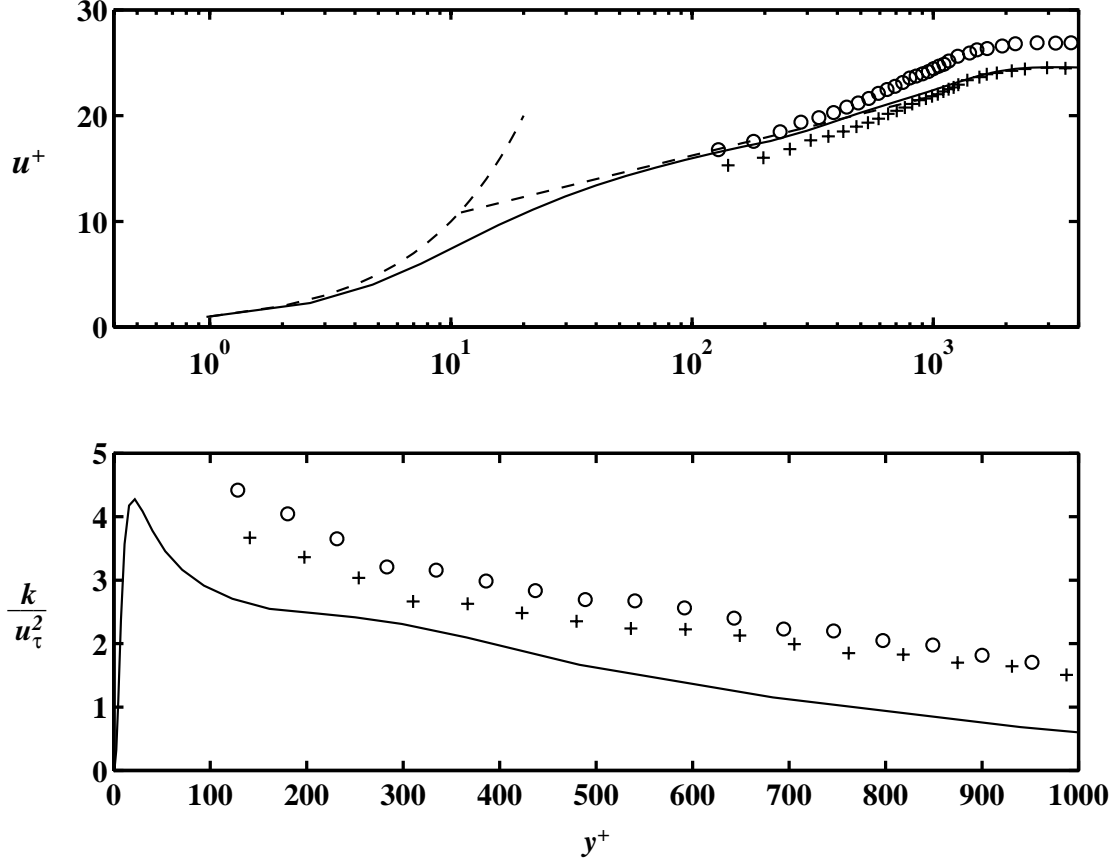


Figure 4.4: Annular nozzle profiles near the end-corner of the circular cylinder. (Top) streamwise velocity distribution, — : present work; --- : law of the wall; \circ : Herrin and Dutton’s data; + : **corrected** Herrin and Dutton’s data. (Bottom) turbulent kinetic energy distribution.

friction velocity ($u_{\tau,num} = 23.3 \text{ m/s}$) which improves the agreement between the two data sets in the wall layer.

The bottom part of Figure 4.4 compares the predicted turbulent kinetic energy at the exit of the nozzle with its measured counterpart. Given that experimentally it was not possible to measure the azimuthal turbulence component, $\overline{v_\theta'}$, inside the nozzle annular channel, the experimental turbulent kinetic energy shown was calculated as

$$k = \frac{1}{2}(\overline{u'^2} + 2\overline{v_r'^2}). \quad (4.2.1)$$

As seen in the figure, even though the shape of the computed kinetic energy function is in agreement with the experimental finding, its magnitude appears to be lower throughout the entire profile even when compared to the experimental data normalized by $u_{\tau,num}$. This difference may be due to modeling errors and/or larger than estimated $\overline{v_\theta'}$ contribution in the experimental data of Herrin and Dutton (1994). However, some of the features of the experimental data question its accuracy.

Near the wall ($y^+ < 100$), this annular boundary layer should have the same characteristics as the boundary layer over the flat plate. Consequently, the turbulent kinetic energy should peak at $y^+ \approx 20$ with a value of roughly $4u_\tau$ (see Figure 3.5, insert). The peak in the experimental turbulent kinetic energy cannot be determined from the data, given its lack of resolution near the wall; however, if it were extrapolated from the available data, it would be much larger than $4u_\tau$, or it would occur at $y^+ \gg 20$.

The experimental data was taken by pushing the circular cylinder outside the confines of the nozzle exit (Herrin, 1995). Based on inviscid theory, this should have no effect on the measurements, given that the hyperextended circular cylinder will remain within the “test diamond” region of the nozzle (Pankhurst and Holder, 1952). However, in a turbulent flow, the hyperextension of the circular cylinder will change the character of the flow in the base region, and this information may propagate upstream through the subsonic portion of the boundary layer. The observation that the experimental values of k cannot collapse on the accepted values supports the conjecture that the experimental measurements might be in

error.

4.3 Effects of turbulence modeling

The base flow structure resulting at the design pressure ratio (*i.e.*, $P_e = P_r$) was studied using both the Baldwin-Lomax and Chien's k - ϵ turbulence models. Figure 4.5 shows a comparison between the experimental base pressure measured by Herrin and Dutton (1994) and the numerical predictions of this and two other studies (Sahu 1994, Tucker and Shyy 1993). In the figure, it is seen that the Baldwin-Lomax model does not predict the distribution of pressure at the base of the cylinder with satisfactory accuracy. It underpredicts the correct pressure by more than 50%, and the shape of the distribution contains large swings in the pressure as a function of radial distance. The other numerical results are in better agreement with the experiment. Despite slight differences in their numerical algorithms, k - ϵ formulations, grid resolutions and distributions, and boundary conditions, the results are virtually the same.

The k - ϵ results underpredicted the value of base pressure by 6%, for $r/R > 0.4$, and overpredicted it by 22% at the center of the base. This result is not due to inadequate resolution, since it was confirmed by a higher resolution simulation (*i.e.*, $530 \times 161 + 509 \times 557 + 674 \times 249$) which yielded results that only differed from the normal resolution case for $r/R < 0.05$. Further examination of the high resolution data revealed that the resolution discrepancy was produced by a small counter-clockwise recirculation zone at the center of the base, which is not resolved at normal grid resolutions.

Even though the difference between the numerical and experimental predictions of averaged-base-pressure vanishes when the pressure is integrated ($\bar{P}_{b,exp} =$

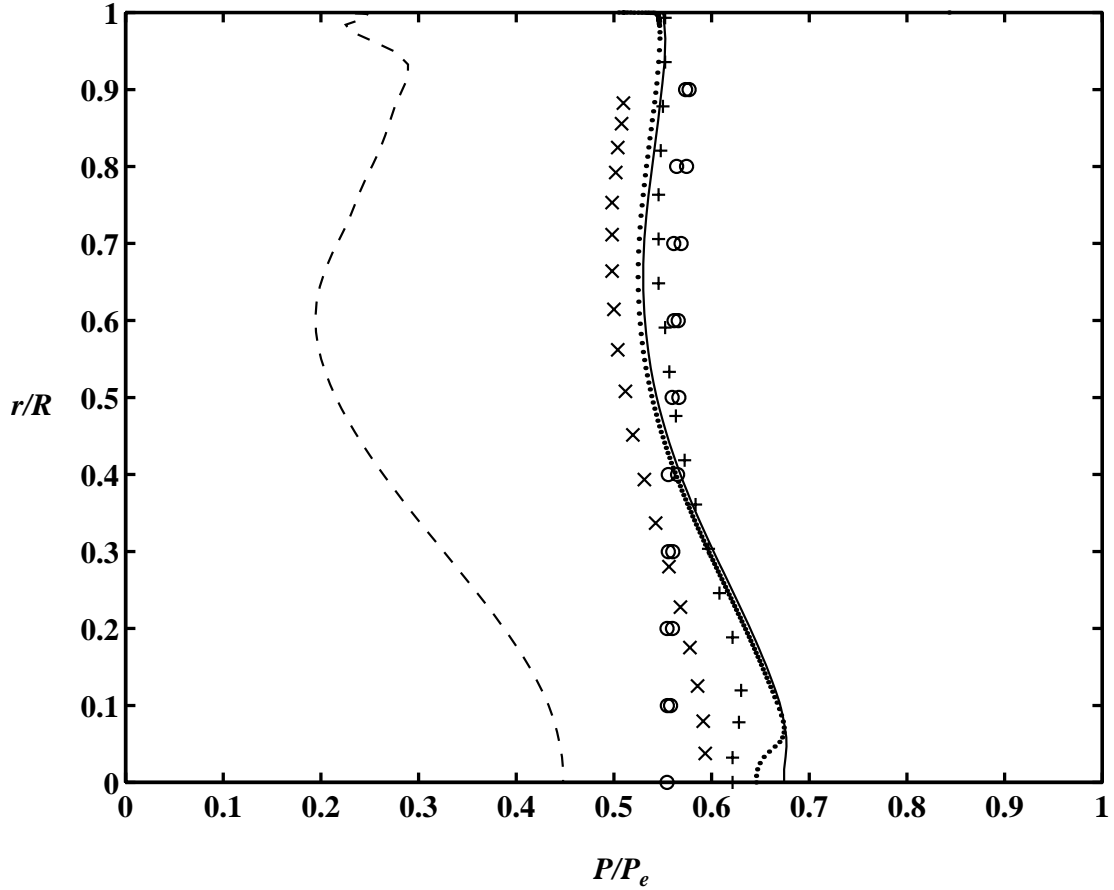


Figure 4.5: Base pressure distribution. — : Chien's $k-\epsilon$; \cdots : Chien's $k-\epsilon$, (high resolution); --- : original Baldwin-Lomax ; + : Sahu; \times : Tucker and Shyy; \circ : Herrin and Dutton.

18.366 kPa vs. $\bar{P}_{b,num} = 17.894 kPa$, or 2.6% difference), the error in the prediction of base pressure would be significant for a gas-metal atomization simulation, given that the metal flow is only affected by the pressure at the center of the base. In light of this, one may choose to obtain a value of averaged base pressure and use it to predict the drawing force that the liquid metal experiences during atomization.

Some understanding of the differences between the two turbulence model predictions can be achieved by comparing the overall flow structure in the base region. Figure 4.6 compares the Mach number distributions obtained using the Baldwin-

Lomax and Chien's k - ϵ models. As seen in the top half of the figure, the Baldwin-Lomax prediction shows a smaller and shorter recirculation region than the k - ϵ results (bottom half). This is due to a prediction of larger turbulence diffusion across the inner shear layer combined with a larger-than-expected growth of the shear layer. In fact, the Baldwin-Lomax results show a violent and unphysical recirculating flow at the base of the cylinder with the flow along the axis of symmetry becoming supersonic (in the upstream direction) close to the base ($x/R \approx 0.4$). It is this faster moving fluid, predicted by the Baldwin-Lomax results, that yields the lower values of pressure throughout the face of the cylinder. Furthermore, the deceleration of this reversed supersonic flow along the axis of symmetry is what yields the large spike in pressure near the center of the cylinder. In contrast, the inner shear layer of the k - ϵ simulation spreads at a slower rate and leads to a lower magnitude of the velocity in the recirculation region. Consequently, a smoother base pressure distribution is obtained.

A similar physical process appears to take place in the outer shear layer of the flow. As seen in the top part of Figure 4.6, the Baldwin-Lomax model predicts a large amount of diffusion in the outer shear layer, leading to an early spread of the jet. In contrast, the k - ϵ model prescribes a smaller amount of diffusion in this area and, therefore, the outer shear layer spreads only at about half the rate predicted by the Baldwin-Lomax model. Judging from Schlieren pictures of the experiment (Herrin and Dutton 1993, Sauter and Dutton 1989), the spread predicted by the k - ϵ model appears to be more physical than that estimated by the Baldwin-Lomax model.

Figure 4.7 shows more evidence of the large turbulent diffusion and the early shear layer growth in the Baldwin-Lomax simulation as well as its effects on the

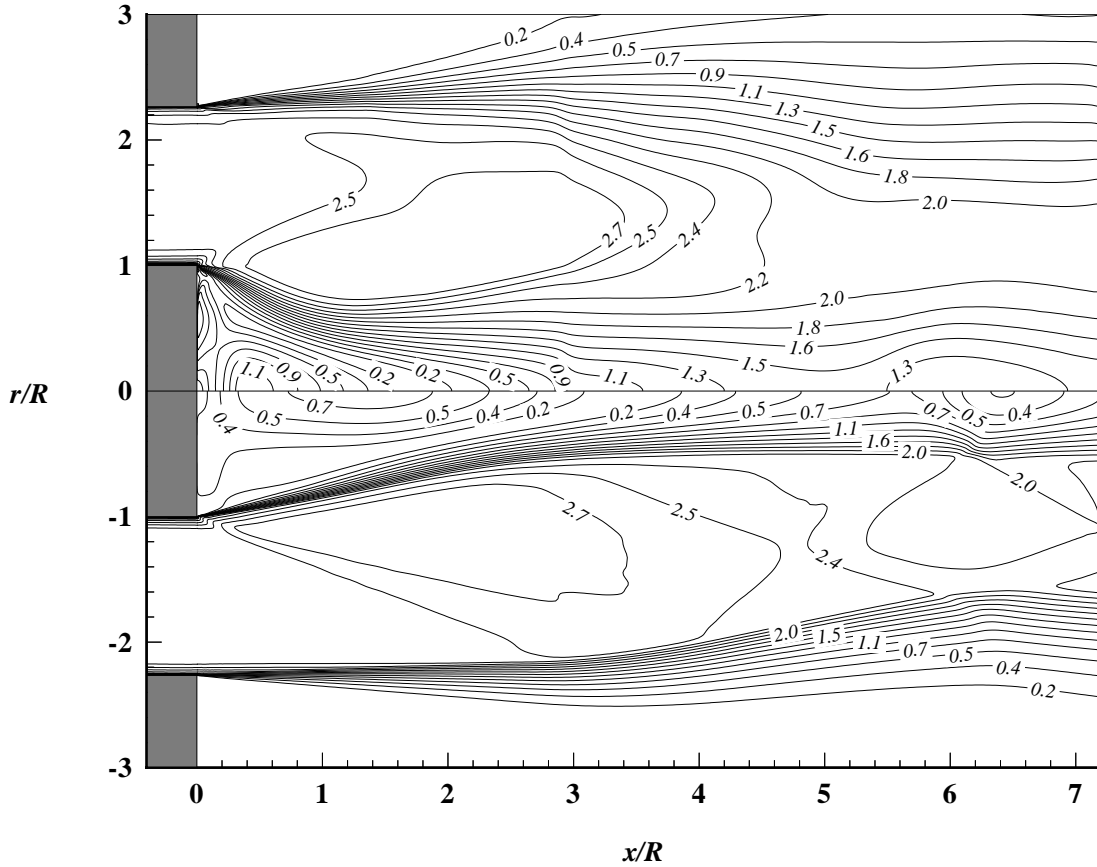


Figure 4.6: Mach number distribution in the wake of the circular cylinder. (Top half) original Baldwin-Lomax model. (Bottom half) Chien's $k-\epsilon$ model.

overall structure of the wake region. From the figure, it can be seen that the results obtained with the Baldwin-Lomax model exhibited an axial velocity distribution that peaks negatively very close to the base and then recovers too fast, producing an early reattachment at $x/R \approx 1.75$ (the location of the reattachment point is underpredicted by 34%). If the turbulence diffusion across the shear layer had not been overestimated, the recirculation region would have lower velocities and a slower shear layer growth. This would result in greater similarity between the shape of the recirculation region predicted by the simulation and that of the experiment.

The $k-\epsilon$ results appear to be in better agreement with the experimental data, but nonetheless, they (a) overpredict the magnitude of the velocity in the recir-

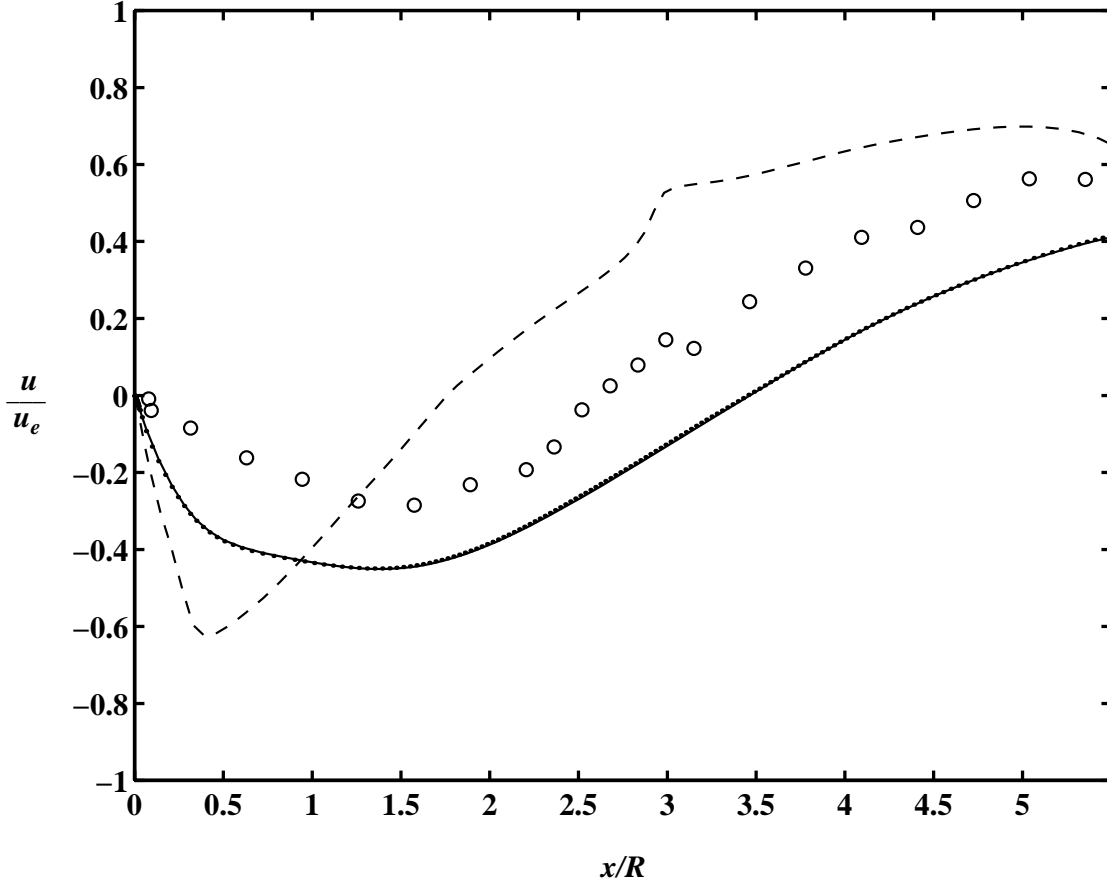


Figure 4.7: Mean axial velocity distribution in the test section ($u_e = 569 \text{ m/s}$). — : Chien's $k-\epsilon$; : Chien's $k-\epsilon$, (high resolution); --- : original Baldwin-Lomax; \circ : Herrin and Dutton.

culcation region at the base, (b) overpredict the location of reattachment point by 30%, and (c) underpredict the velocity recovery after the reattachment point. The overprediction in the magnitude of the velocity of the recirculating region is due to an overprediction in the amount of turbulence diffusion across the separated shear layer. Although similar, the turbulence diffusion is not as severe as that seen in Baldwin-Lomax model results. Combined with an underprediction in the growth of the shear layer, this appears to delay reattachment.

In the Chien $k-\epsilon$ model, the balance between the production and dissipation of turbulent dissipation, ϵ , is controlled by the magnitude of the $C_{\epsilon 1}$ and $C_{\epsilon 2}$

constants. As seen in chapter 2, the value of the C_{ϵ_2} constant was deduced from the decay of high-Reynolds-number grid turbulence by Hanjalic and Launder (1976). However, the value of C_{ϵ_1} was obtained by keeping the difference between C_{ϵ_1} and C_{ϵ_2} as prescribed by Jones and Launder (1972). This selection yields the production and dissipation of ϵ in near balance for wall bounded flows.

Recently, Yakhot *et al.* (1992) made use of renormalization group methods to develop explicitly a k - ϵ model that differs from Chien's in the addition of an extra production term to the ϵ equation. This extra term becomes significant in rapidly distorted flows. In their work, this extra production term is modeled as a modification to the turbulent dissipation production constant, C_{ϵ_1} , given as

$$C_{\epsilon_1}^* = C_{\epsilon_1} - \frac{\eta(1 - \eta/\eta_0)}{1 + \beta\eta^3} \quad (4.3.2)$$

where $\eta = k/\epsilon\sqrt{2S_{ij}S_{ij}}$, η_0 is a fixed point constant, and β is a constant determined from testing the model in well characterized flows (e.g., turbulent boundary layer).

The use of Yakhot's RNG model led to mixed results in the simulation of the base flow. However, the notion of reducing the production of ϵ due to the inherent lack of local isotropy in rapidly distorted flows (see Durbin and Speziale 1991), led to our use of a reduced value of C_{ϵ_1} in the standard Chien's k - ϵ model.

Figure 4.8 shows the effects of a 10% global reduction in the value of C_{ϵ_1} (*i.e.*, $C_{\epsilon_1} = 1.215$). As seen in the figure, the reduction in the production of turbulence dissipation yields a prediction of flow reattachment in agreement with the experimental findings. Furthermore, the velocity recovery after the reattachment point is in better agreement with the experiment than the prediction made by the original Chien model. Nonetheless, the prediction of the circulation velocity inside the separation region remains in disagreement with the experimental findings. This leads us to believe that there is an overprediction in the momentum transfer across

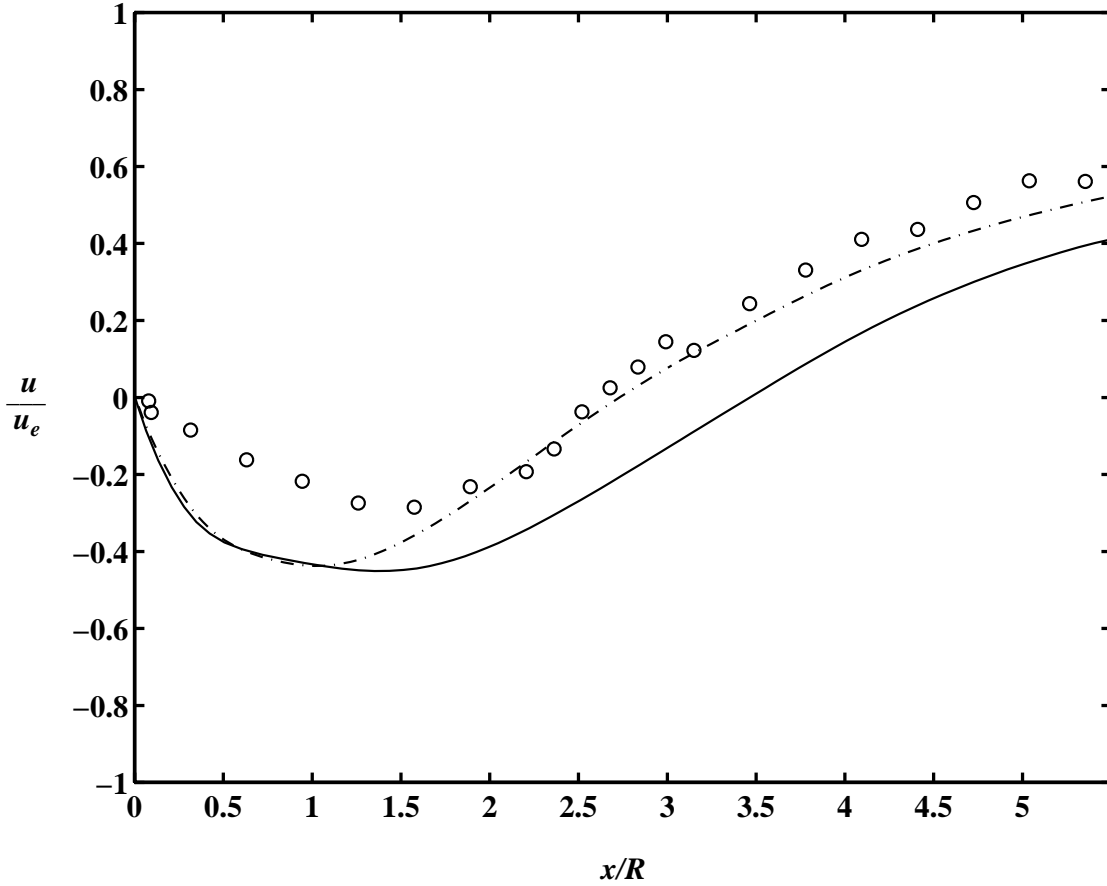


Figure 4.8: Effect of the reduction in turbulence dissipation production on the mean axial velocity distribution in the test section ($u_e = 569 \text{ m/s}$). — : Chien's $k-\epsilon$ model, $C_{\epsilon 1} = 1.35$ (original); - - - : Chien's $k-\epsilon$ model, $C_{\epsilon 1} = 1.215$ (10% reduction in the production of ϵ); \circ : Herrin and Dutton.

the inner shear layer which is over-driving the recirculation inside the bubble.

Figure 4.9 shows how the reduction in the production of turbulence dissipation has slightly degraded the prediction of base pressure distribution. However, the shape of the curve has remained unaffected by the reduction in $C_{\epsilon 1}$, given that the structure of the flow inside the recirculation region remains unchanged. As a result, the estimates of base pressure have improved near the center of the base but have degraded towards its edge. Nonetheless, the overall prediction of base pressure remains within acceptable values when compared to the findings of Tucker

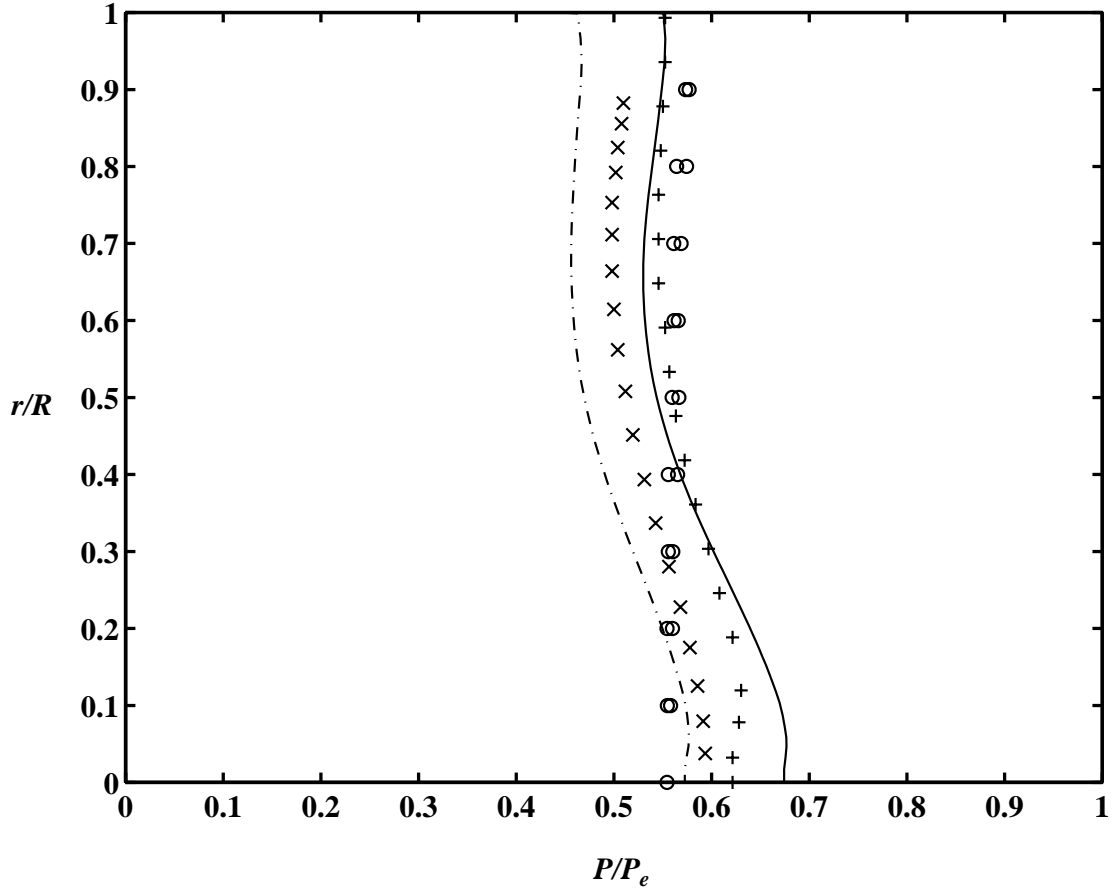


Figure 4.9: Effect of the reduction in turbulence dissipation production on the base pressure distribution. — : Chien's $k-\epsilon$ model, $C_{\epsilon 1} = 1.35$ (original model); - - - : Chien's $k-\epsilon$ model, $C_{\epsilon 1} = 1.215$ (10% reduction in the production of ϵ); + : Sahu; \times : Tucker and Shyy; \circ : Herrin and Dutton.

and Shyy (1993) and Sahu (1994).

Figure 4.10 reveals the full effects of the reduction in the production of turbulence dissipation in the topography of the base flow. As seen in the image, the main effect manifests itself as an increase in the shear layer spreading rate. For the inner shear layer, this increase helps the reattachment point to move to its correct location and as expected, the increase in the outer shear layer spreading rate increases the overall jet diameter. However, the jet diameter does not grow enough to push it outside of the bounds set by the experimental Schlieren images (Herrin, 1993).

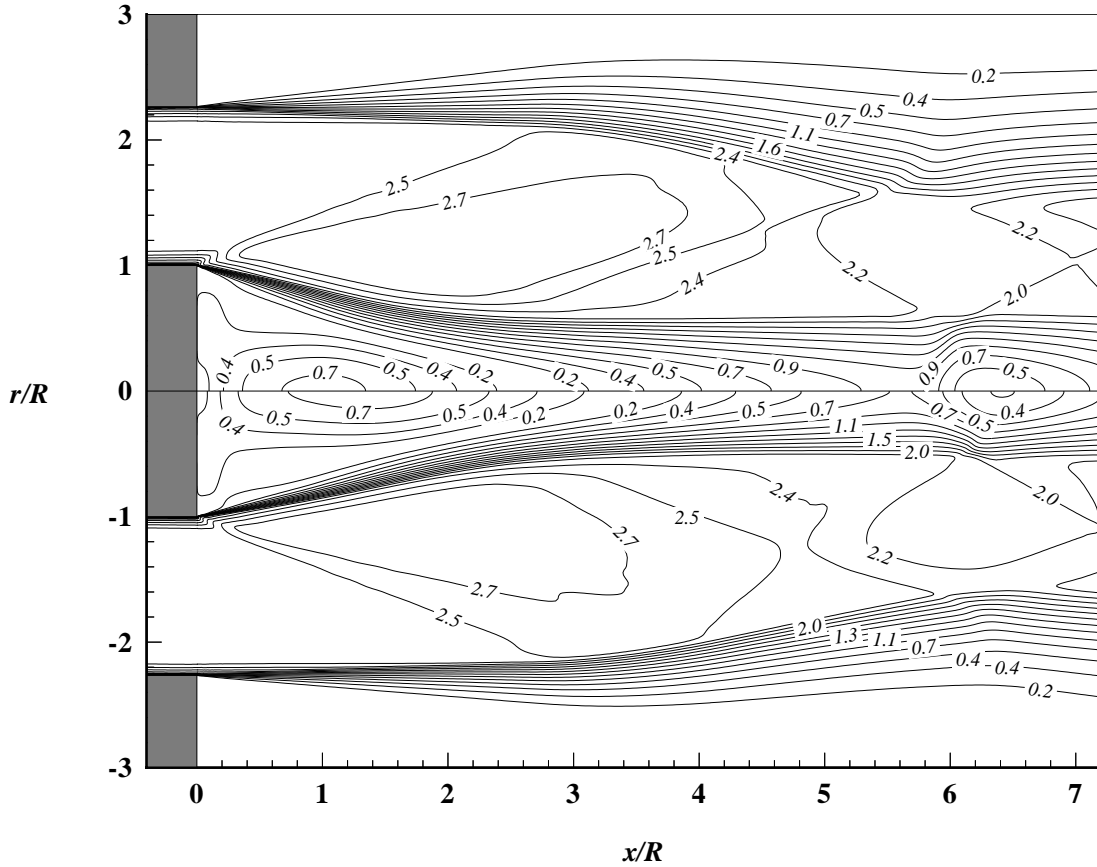


Figure 4.10: Effect of the reduction in turbulence dissipation production on the Mach number distribution in the wake of the circular cylinder. [Top half] Chien's $k-\epsilon$ model, $C_{\epsilon 1} = 1.215$ (10% reduction in the production of ϵ); [Bottom half] Chien's $k-\epsilon$ model, $C_{\epsilon 1} = 1.35$ (original model).

4.4 Effects of pressure ratio

Given the fundamental interest of this investigation in gas-metal atomization flows, numerical experiments were conducted to determine the effects of jet pressure ratio on the structure of the flow field at the base of the cylinder. Using the same number of grid points, simulations were conducted at pressure ratios, P_e/P_r , of 0.96 (5% overexpanded), 1.01 (\simeq design), and 1.07 (5% underexpanded). For all simulations, Chien's $k-\epsilon$ model was used.

Figure 4.11 compares the base pressure distributions for jets at the three pressure

ratios considered. From the figure, it can be seen that the shape of the base pressure distribution appears to be independent of the jet pressure ratio, being higher at the center of the base and flatter towards its edge. As expected, the magnitude of the base pressure is inversely proportional to the jet pressure ratio. However, this behavior was found to be nonlinear given that a 5% change in jet pressure ratio yielded a larger change in base pressure for the underexpanded jet than for the overexpanded jet.

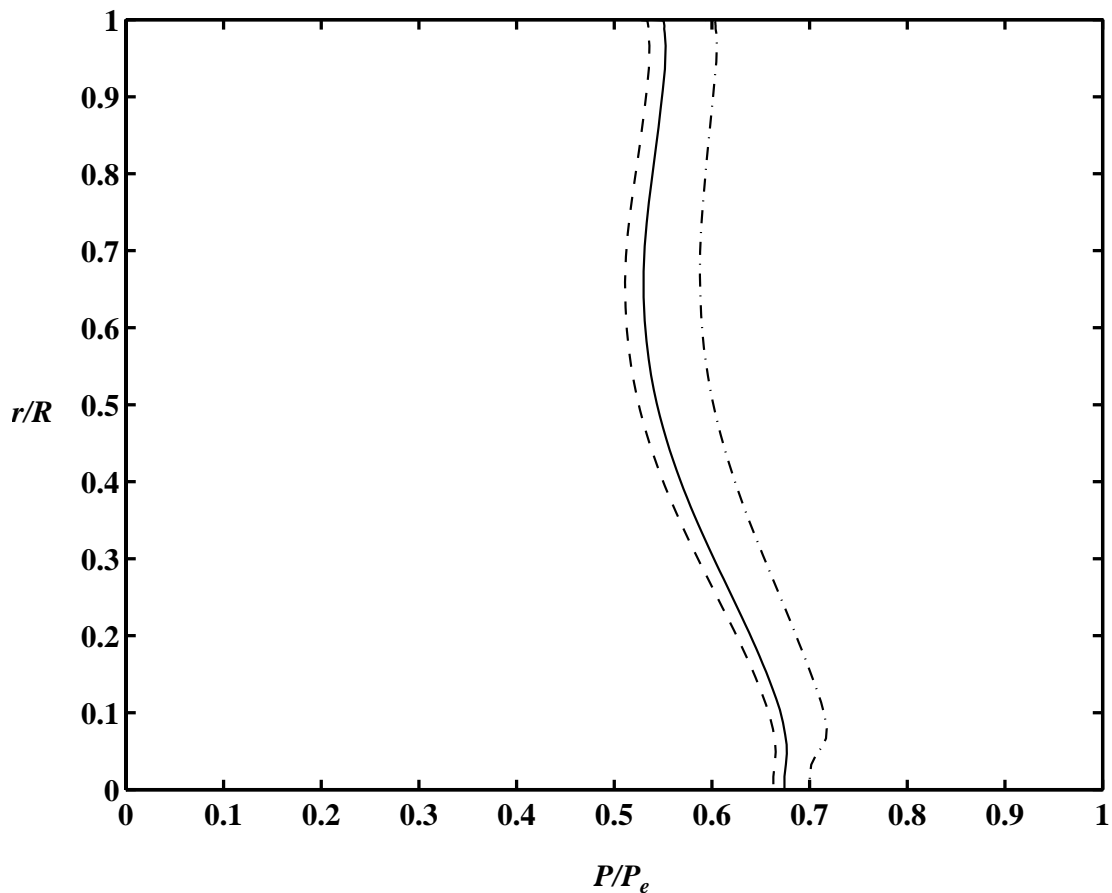


Figure 4.11: Effect of jet pressure ratio on base pressure distribution. - · - · : Over-expanded, $P_e/P_r = 0.96$; — : Design, $P_e/P_r = 1.01$; - - - : Underexpanded, $P_e/P_r = 1.07$.

Even more interesting is the comparison between the flow field structures obtained for the different jet-pressure ratios. Figure 4.12 shows static pressure and Mach

number distributions for the three jets. The Mach number distributions appear to be very similar in character at all pressure ratios, with an inner shear layer that attaches to the axis of symmetry near $x/R \approx 3.5$ (with overprediction of about 30%). The outer shear layer follows the contours of the pressure diamonds with limited spreading (about R thickness) at distances of $x/R = 7$.

The pressure distributions illustrate many of the flow structures schematically described in Figure 4.1. For the overexpanded jet (top diagram in Figure 4.12), a weak shock wave is seen emerging from the outer lip of the nozzle. This shock wave crosses the expansion fan emerging at the end-corner of the circular cylinder and with it, encapsulates the recirculation region at the base of the cylinder. Something very similar is observed in the underexpanded jet (bottom diagram in Figure 4.12), although the shock wave is replaced by an expansion wave that emanates from the outer lip of the nozzle. In the design jet (center diagram in Figure 4.12), there is neither a shock nor an expansion wave originating at the outer lip of the nozzle (the lines observed in this region are due to noise in the contouring algorithm used to plot the data) and therefore, there is no encapsulation of the base flow region by wave structures. The volume of the recirculation region appears to be directly proportional to the jet pressure ratio.

Further downstream, the jet structures appear to be very similar. The expansion waves emanating from the end-corner of the cylinder are reflected as compression waves by the outer shear layer. They interact with the compression waves created in the reattachment zone at the axis of symmetry and lead to two shock waves from different families which then initiate a dual diamond structure similar to that seen in annular supersonic jets.

For all three pressure ratios studied, some of the structures associated with the

inner shear layer remain for distances of up to $x/R = 9$ (see Figure 4.13). This continuation of the inner shear layer prevents the downward propagating shock wave from reaching the axis of symmetry, reflecting it at $x/R \approx 6.2$ and $r/R \approx 0.5$. This process totally bypasses the formation of the Mach reflection reported in other base flow investigations (Mueller, 1973). Meanwhile, the upward propagating shock wave reflects from the outer shear layer at $x/R \approx 6.4$ resulting in an expansion fan that is absorbed by the continuation of the inner shear layer in the area from $x/R \approx 8.0$ to 9.2. From this location on, the jet loses its dual diamond structure associated with its annular formation and instead, exhibits a single barrel-shock chain similar to that seen in regular supersonic jets.

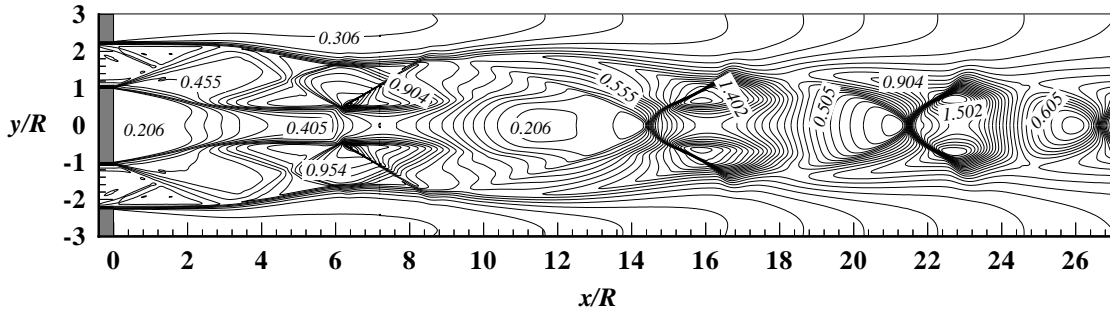


Figure 4.13: Density distribution in the wake of a circular cylinder at design pressure ratio (ρ/ρ_{ref} , $\rho_{ref} = 1.293 \text{ kg/m}^3$).

Figure 4.14 shows the effects of pressure ratio on the axial velocity distribution of the jet. For $x/R < 2$, the velocity distribution remains almost unchanged, peaking negatively at $x/R \approx 1.5$. However, for larger axial distances, the length of the jet structures is directly proportional to the pressure ratio.

The reattachment point moves upstream in the underexpanded jet and downstream in the overexpanded jet. This behavior results from the strength of the expansion fan at the end-corner of the cylinder, which deflects the flow in the underexpanded jet at a sharper angle towards the axis of symmetry than it does in

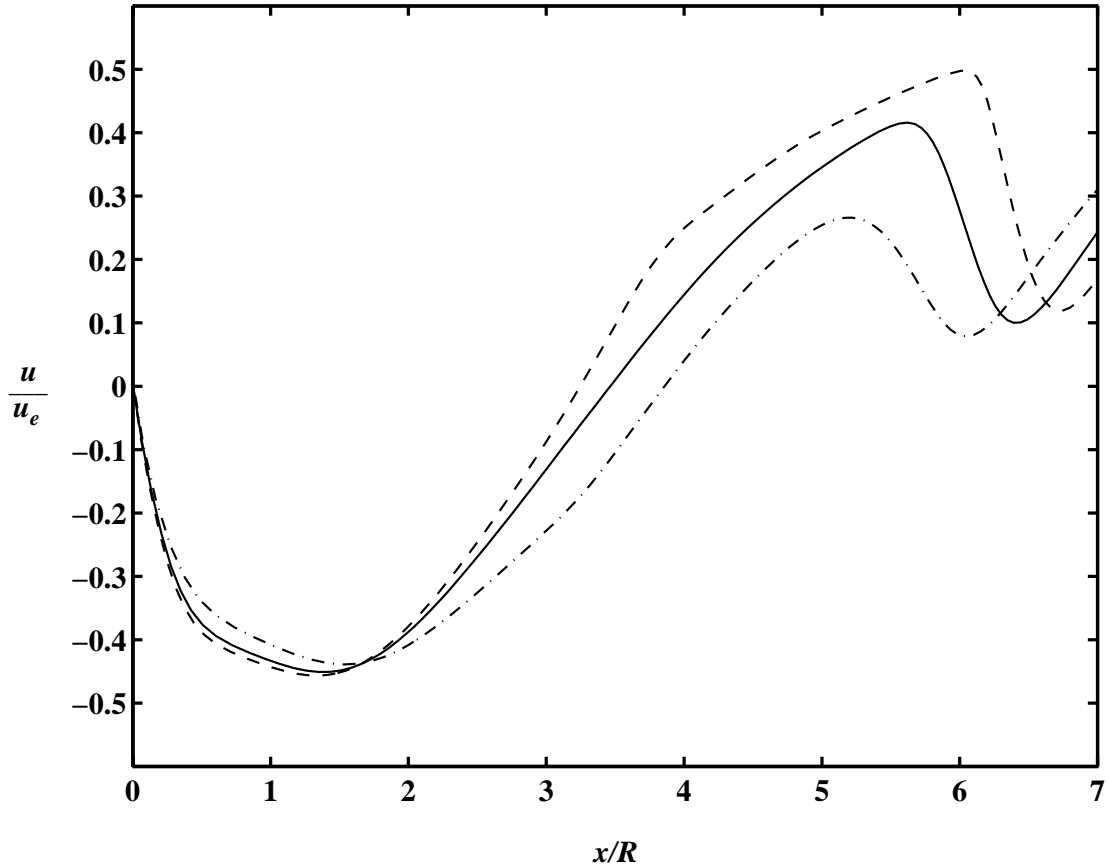


Figure 4.14: Effect of jet pressure ratio on mean axial velocity distribution in the test section ($u_e = 569 \text{ m/s}$). $- \cdot - \cdot -$: Overexpanded, $P_e/P_r = 0.96$; $—$: Design, $P_e/P_r = 1.01$; $- - -$: Underexpanded, $P_e/P_r = 1.07$.

the overexpanded jet. The fact that the magnitude of the change in the location of reattachment is almost the same for both off-design jets indicates that the relationship between pressure ratio and reattachment location is linear for this range of pressure ratios.

At larger axial distances ($5 < x/R < 7$), the axial velocity peaks for the first time. The deceleration that follows tends towards the discontinuity associated with a Mach reflection as the pressure ratio is increased. In fact, the peak in axial velocity only attains a Mach number of 0.5 for the overexpanded jet, while it reaches $M = 0.9$ for the underexpanded case. Further increases in the pressure

ratio force the inner shear layer closer to the axis of symmetry, resulting in the formation of a Mach reflection.

4.5 Summary

The base flow results seen in this chapter are in acceptable agreement with the experimental data and results from previous numerical investigations. Local values of base pressure were found to differ from their experimental counterparts by as much as 22%. However, the averaged value of base pressure was found to be in agreement with the experiment. The location of the reattachment point was overpredicted by 30% due to a smaller than expected growth of the inner shear layer.

The magnitude of the base pressure was found to be inversely proportional to the jet pressure ratio, even though the function appears to be nonlinear. The axial locations of jet structures were found to be directly proportional to the jet pressure ratio. However, the location of the reattachment point was found to follow the inverse behavior. This effect was shown to be associated with the strength of the expansion process at the end-corner of the circular cylinder which deflects the inner shear layer at sharper angles for higher pressure ratios.

Improvements to the numerical prediction were attained by reducing the production of turbulence dissipation by 10% from the values prescribed by Chien. At this level of turbulence dissipation, the numerical prediction of the reattachment location matched that from the experiments. There was a small degradation in the prediction of the base pressure distribution and an increase in the shear layer spreading rates, but overall, the agreement with the experimental findings was improved by the 10% reduction in $C_{\epsilon 1}$.

The results indicate that there are four distinct flow regimes that these base flows undergo as a function of jet pressure ratio. At low pressure ratios in the overexpanded regime, the jet exhibits an annular structure which leads to an open base region with a pressure close to that of the receiving chamber. At pressure ratios near the design condition, the inner shear layer reaches the axis of symmetry closing the base region. However, a subsonic core remains and this perpetuates the annular wave structure of the jet. At higher pressure ratios, the core of the jet attains supersonic velocities and leads to the formation of a Mach reflection downstream of the reattachment point. This Mach reflection changes the character of the jet from annular to circular. Further increases in the jet pressure ratio lead to the replacement of the Mach reflection by a simple reflection at the axis of symmetry.

The methodology used to obtain the previously shown results should enable the use of similar numerical methodology for the simulation of the gas-only flow fields in close-coupled gas-metal atomizers that have geometries similar to that studied here.

Chapter 5

Close-Coupled, Gas-Metal Atomizer Gas-Only Flow

Given the difficulty in controlling the flow of a molten metal stream at 1900 K, efforts in the control of gas-metal atomization have been primarily focused on controlling the gas flow. The following is a study of the gas-only flow produced by a **generic** close-coupled gas-metal atomizer. By “generic”, it is implied that the geometry of the atomization nozzle assembly was selected to be representative of numerous designs used by other researchers and industry. The operational parameters are based on those typically used for the production of metal powder (Ridder and Biancaniello 1988, Ayers and Anderson 1985). Figure 5.1 schematically shows the geometry considered here, and Table I contains a summary of the operational parameters with their typical associated ranges.

It is a well established fact that the geometry shown in Figure 5.1 produces a low pressure region at the base of the liquid-delivery tube, P_{dt} , often referred to as “aspiration”. It can be shown that this aspiration pressure is the controlling factor in the establishment of the liquid metal flow rate, and therefore, its control has been the subject of numerous investigations (see Chapter 1). Couper and Singer

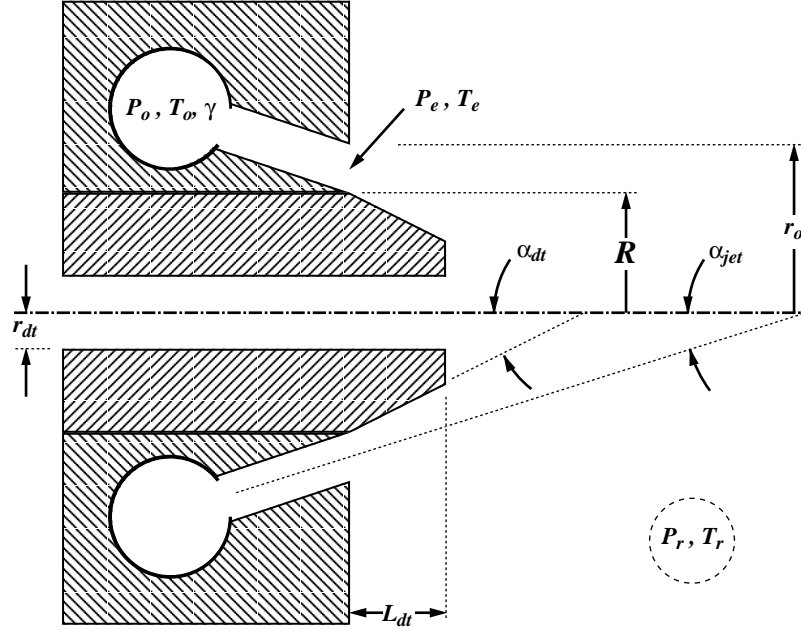


Figure 5.1: Schematic diagram of annular jet, close-coupled atomization nozzle assembly studied in this investigation (geometry rotated 90° ccw from its normal operational orientation).

(1985) and Ayers and Anderson (1985) reported that their atomizer produced the finest powder when the jet pressure ratio was set to the value that yielded the maximum aspiration (*i.e.*, the lowest P_{dt}). This finding has led to the conventional operation of atomizers at this maximum aspiration condition. Figure 5.2 shows the gas-only flow that results when the atomizer in Figure 5.1 operates at the maximum aspiration condition.

In what follows, section 1 describes the physical domain and boundary conditions used to numerically study the gas-only flow in our selected atomizer. Section 2 describes the influence of the production of turbulence dissipation on the topology of the gas-only flow near the maximum aspiration condition. In section 3, we study, both numerically and experimentally, the functionality of the aspiration pressure on gas jet pressure ratio and its relation to the resulting jet topology. Section 4 studies, in a similar manner, the effects of jet temperature ratio on the topology

Parameter	Symbol	Operational Range	Baseline
liquid-delivery tube radius	R		4.825 mm
outer annular channel radius	r_o/R		1.0632
annular channel angle	α_{jet}	$0^\circ \rightarrow 27.5^\circ$	22.5°
liquid-delivery tube face angle	α_{dt}	$0^\circ \rightarrow 27.5^\circ$	22.5°
liquid-delivery tube extension	L_{dt}/R	$0 \rightarrow 0.6$	0.6
liquid-delivery tube inner radius	r_{dt}/R	$0.21 \rightarrow 0.31$	0.31
gas		Ar, He, or N ₂	Ar
receiving chamber pressure	P_r		1 atm
gas jet pressure ratio	P_e/P_r	$3.8 \rightarrow 53.5$	33
receiving chamber temperature	T_r		293 K
gas jet temperature ratio	T_e/T_r	$0.65 \rightarrow 1.31$	0.65

Table I: Parameter ranges used during the operation of the gas-metal atomizer in Figure 5.1.

of the atomization gas-only flow field, while section 5 describes the effects of mass injection at the base of the liquid-delivery tube hinting to the effects that the metal flow may have on the gas flow. Finally, section 6 summarizes the findings reported in this chapter and suggests elements of importance in the design of close-coupled gas-metal atomizers.

5.1 Physical domain and boundary conditions

The computational domain used in this investigation (see Figure 5.3) follows the specifications of the close-coupled atomizer used by Ridder and Biancianiello (1988). However, it changes their discrete jet geometry to an annular jet version with the same total cross-sectional area. The computational domain was segmented into three separate blocks: block 1 is the annular channel (discretized using 42×41 points in the axial and radial directions respectively), block 2 is the volume over the liquid-delivery tube (a ring-shaped volume extending radially outward from the liquid-delivery tube external diameter and bound in the axial direction by the

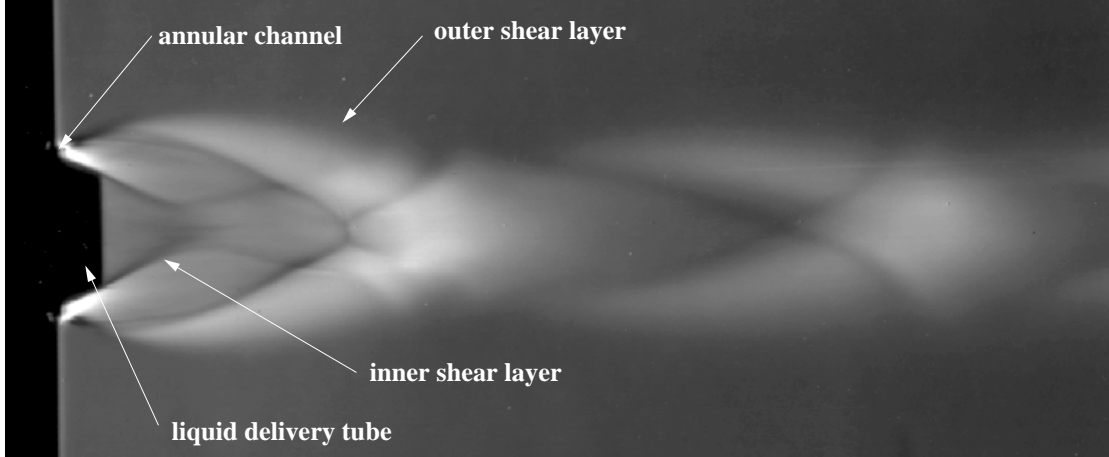


Figure 5.2: Schlieren image of the gas-only flow in a close-coupled gas-metal atomizer operating at baseline settings (flow from left to right).

liquid-delivery tube end; 57×161 grid points were used), and block 3 is the volume after the axial end of the liquid-delivery tube (289×215). Blocks 2 and 3 extend radially to a distance of $10R$ (see Figure 5.3), while block 3 extends axially to a distance of $14.7R$ from the exit plane of the annular channel. Within each block, the mesh points were distributed using the SAGE grid adaptation program (Davies and Venkatapathy, 1992). At all solid boundaries, the first line of points parallel to the wall was forced to be located at $y^+ \simeq 1$ to obtain accurate resolution at the wall layer. As an example, Figures 5.4 and 5.5 show one of the final adapted grids used.

Characteristic-type boundary conditions were used at the inlet of the annular channel (P_o , T_o specified) and at the free boundaries of blocks 2 and 3 (P_r , T_r specified). The block 1 \rightleftharpoons block 2 interface as well as the block 2 \rightleftharpoons block 3 interface were interpolated explicitly. Axisymmetry was used at the axis of the third block while all other boundaries were treated as adiabatic, non-slip walls.

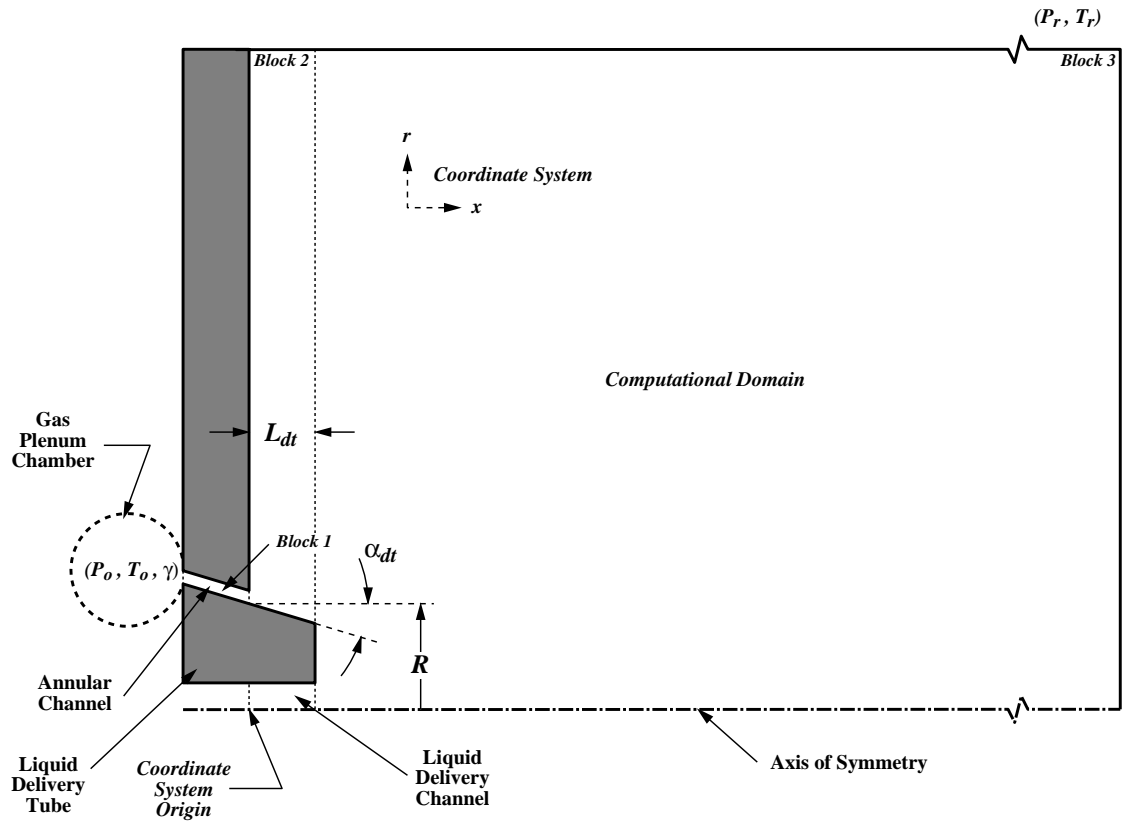


Figure 5.3: Schematic diagram of the computational domain used to model the gas-only flow in a close-coupled atomizer.

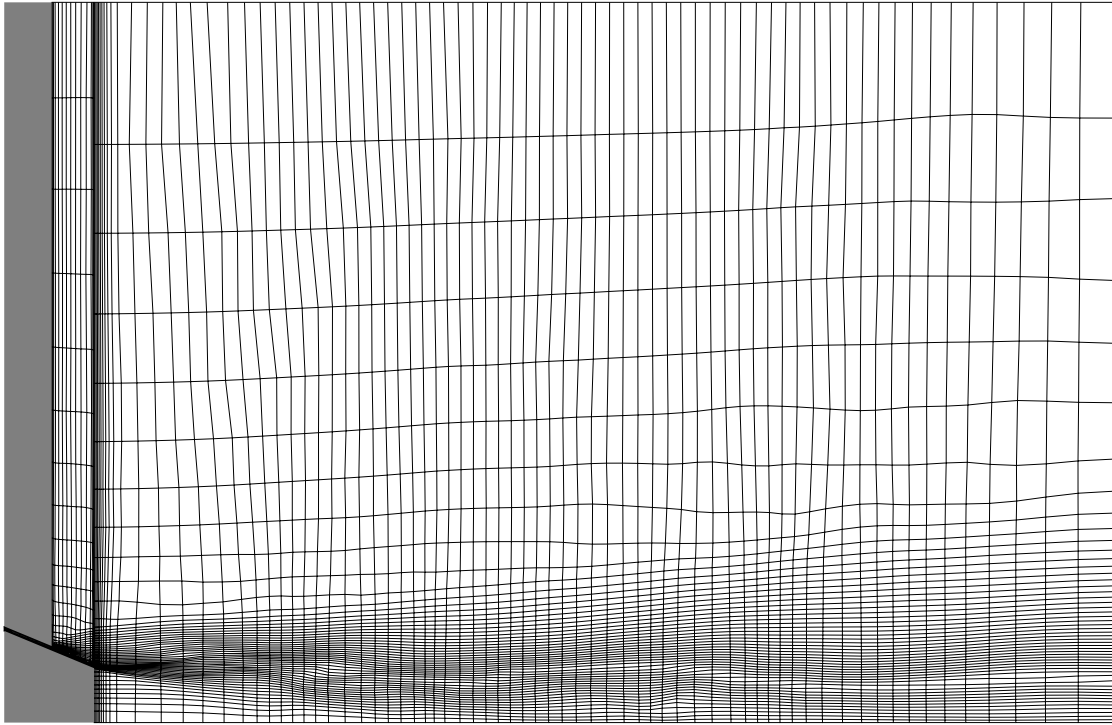


Figure 5.4: Typical computational mesh adapted for simulation of gas-only flow in a close-coupled gas-metal atomizer (only every fourth grid line is shown for clarity).

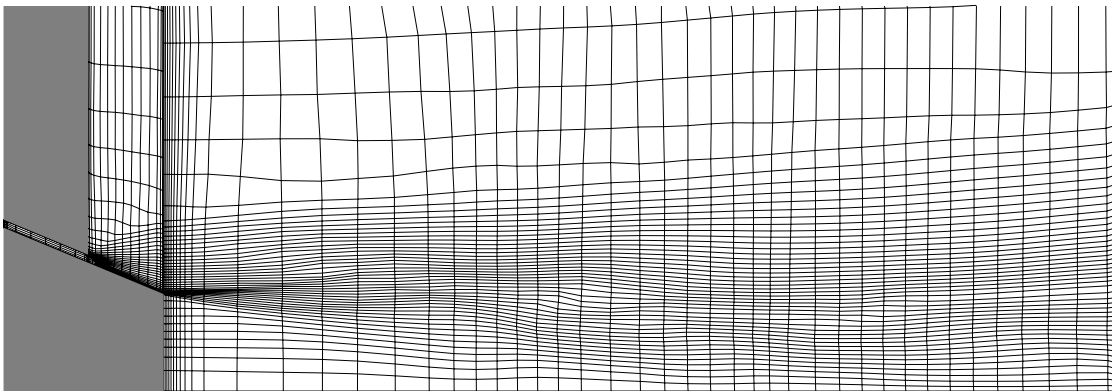


Figure 5.5: Detail of the base region of the computational mesh (only every fourth grid line is shown for clarity).

5.2 Effects of turbulence dissipation production

As seen in the previous chapter, the Chien k - ϵ model has difficulty predicting the structure of the base flow region; the model over-estimates the production of turbulence kinetic energy dissipation rate leading to an underprediction in the turbulence kinetic energy, and thus, an underprediction of the eddy-viscosity. This typically results in an underprediction of the growth rate of the shear layers and an overprediction in the location of the reattachment point. Furthermore, it was shown that an *ad hoc* 10% reduction in the production of turbulence dissipation, \mathcal{P}_ϵ , yields results that are in good agreement with the experimental findings. In this section, we set out to determine the appropriate level of reduction in the production of turbulence dissipation for atomization flows with the selected geometry.

Of interest to this study is the near jet field of the gas-only flow extending up to $8R$ in the axial direction from the exit plane of the annular channel. For the pressure ratios considered here, this area bounds the base flow region which controls the aspiration pressure. Figure 5.6 shows a Schlieren image of the gas-only flow in this area. From it, we can see that the flow contains the same features as the base flow described in Chapter 4 for underexpanded pressure ratios (see Figures 4.1 and 4.12, **bottom**). A noticeable difference between this flow and the base flow in Chapter 4 is the formation of a Mach reflection at $x/R \simeq 3.75$ that results from the considerably higher pressure ratio of approximately 33.

To determine the proper level of turbulence dissipation rate production, three values of the model constant, $C_{\epsilon 1}$, were tested: the one used in the original Chien's k - ϵ model (1982) ($C_{\epsilon 1} = 1.35$), one with a 10% global reduction in \mathcal{P}_ϵ ($C_{\epsilon 1} = 1.215$), and one with a 20% global reduction in \mathcal{P}_ϵ ($C_{\epsilon 1} = 1.08$). Figure 5.7 shows the

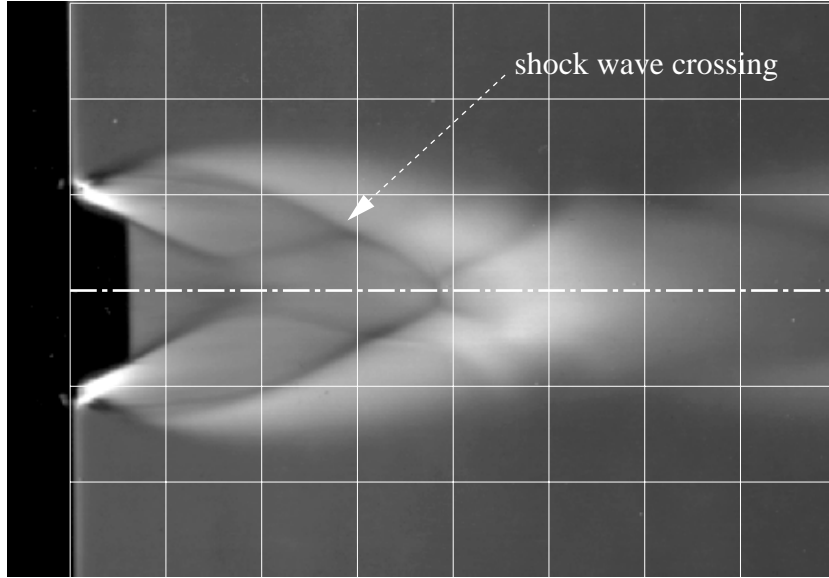


Figure 5.6: Schlieren image of the gas-only flow (base region detail) produced by the selected close-coupled atomization nozzle assembly when operated at baseline settings. Mesh with unit element R^2 , superimposed for dimensional reference.

density distributions obtained in these simulations.

The results yielded by the original Chien $k-\epsilon$ model (Figure 5.7, **top**) exhibited an instability of the outer shear layer which originated at the end of the annular channel and was amplified as the flow progressed downstream – see irregularities in the $\rho/\rho_r = 1$ contour. This instability, which could be either numerical or due to the inflection point in the mean velocity profile, was not followed accurately in time. Other stable features of the solution appeared to be in gross error: first, the real atomizer flow (Figure 5.6) exhibits a crossing between the two initial shock waves at $x/R \simeq 2.8$, $r/R \simeq 0.6$; in the numerical result, this crossing occurs at $x, R \simeq 2.2$, $r/R \simeq 1.0$. This produces a shorter than expected first barrel-shock structure² which, in turn, leads to a larger number of barrel-shocks in the length of the jet than there are in the real flow. Second, in the real atomization jet, the

²A “barrel-shock” is a repetitive barrel-shaped flow structure initiated by an expansion fan and terminated by an oblique shock wave. The resulting flow pattern is often seen in supersonic jets as a series of diamonds (John 1984).

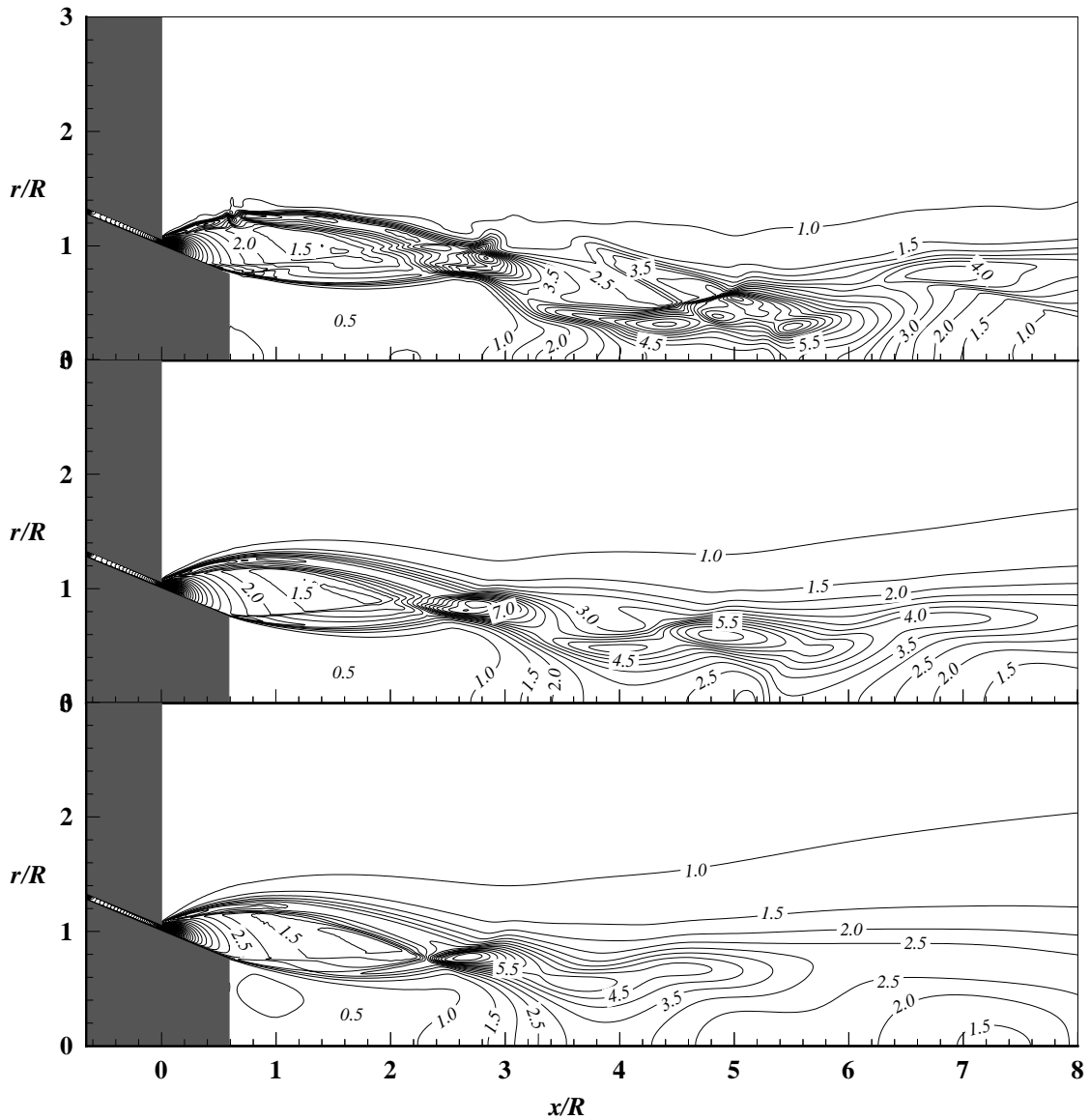


Figure 5.7: Effect of the turbulence dissipation production level on the density distribution of the gas-only atomization flow (baseline settings): $\rho^* = \rho/\rho_r$, $\rho_r = 1.66 \text{ kg/m}^3$; $\Delta\rho^* = 0.5$. **Top:** original Chien's $k\text{-}\epsilon$ model ($C_{\epsilon 1} = 1.35$); **Center:** 10% global reduction in \mathcal{P}_{ϵ} ($C_{\epsilon 1} = 1.215$); **Bottom:** 20% global reduction in \mathcal{P}_{ϵ} ($C_{\epsilon 1} = 1.08$).

inner shear layer projects inward, towards the axis of symmetry, to a maximum radial distance of 0.3; in the numerical result, it only deflects to a distance of 0.6. This leads to differently shaped base flow regions, the real one having an hourglass shape whereas the numerical one looks like a slightly pinched cylinder. Third, the numerical results led to an unphysical supersonic recirculating region (— in Figure 5.8, $M_{max} = 1.79$) that extended to $x/R = 4.00$, and in turn, to a positive pressure at the center of the liquid-delivery tube face (— in Figure 5.9) which is in gross disagreement with the experimental findings even for the average pressure (— in Figure 5.9).

Figure 5.7 (**center**) shows the results obtained with a 10% global reduction in the production of turbulence dissipation. At this level of \mathcal{P}_e , the results yielded a stable outer shear layer and a crossing between the two initial shock waves at $x/R \simeq 2.0$, $r/R \simeq 0.9$. The inner shear layer projected inward, towards the axis of symmetry, to a maximum radial distance of 0.6. However, the shape of the separation region is in better agreement with the experiment than the one predicted by the original Chien k - ϵ model case. For this 10% reduction case, the numerical results led to a fully subsonic recirculating region (--- in Figure 5.8, $M_{max} = 0.99$) that extended to $x/R = 3.69$. This slower separation region produced a base pressure distribution (--- in Figure 5.9) in better agreement with the experimental findings (\circ in Figure 5.9) than the original Chien k - ϵ model estimation. However, the high Mach number continued to contribute to a significant discrepancy in the base pressure between the experiments and the numerical prediction.

Encouraged by the results obtained at 10% reduction levels, we proceeded to simulate the flow with a 20% global reduction in the production of the turbulence dissipation rate. The results obtained at this level (Figure 5.7, **bottom**) yielded

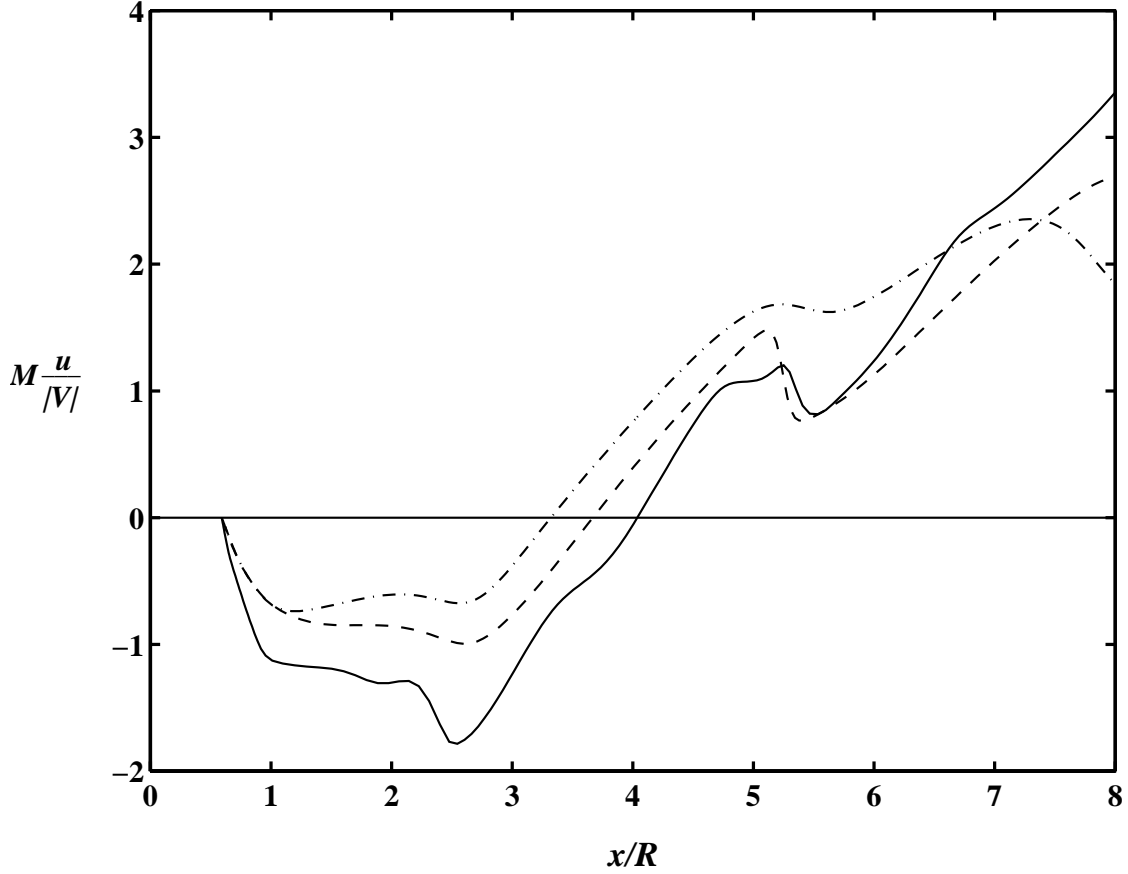


Figure 5.8: Effect of turbulence dissipation production level on axial Mach number distribution of the gas-only atomization flow (baseline settings). — : original Chien’s k - ϵ model ($C_{\epsilon 1} = 1.35$); --- : 10% global reduction in \mathcal{P}_ϵ ($C_{\epsilon 1} = 1.215$); -·-· : 20% global reduction in \mathcal{P}_ϵ ($C_{\epsilon 1} = 1.08$).

the crossing between the two initial shock waves at $x/R \simeq 2.3$, $r/R \simeq 0.8$ and exhibited no stability problems. The inner shear layer projected inward, towards the axis of symmetry, to a maximum radial distance of 0.5, but the shape of the separation region moved away from the hourglass shape seen in the experiment. The recirculating region (-·-· in Figure 5.8) had a length of $x/R \simeq 3.31$ with a maximum Mach number of 0.66. The base pressure distribution (-·-· in Figure 5.9) is in excellent agreement with the experimental findings (■ in Figure 5.9). However, this level of production of turbulence dissipation leads to excessively high levels of eddy viscosity that further leads to the earlier than expected dissipation

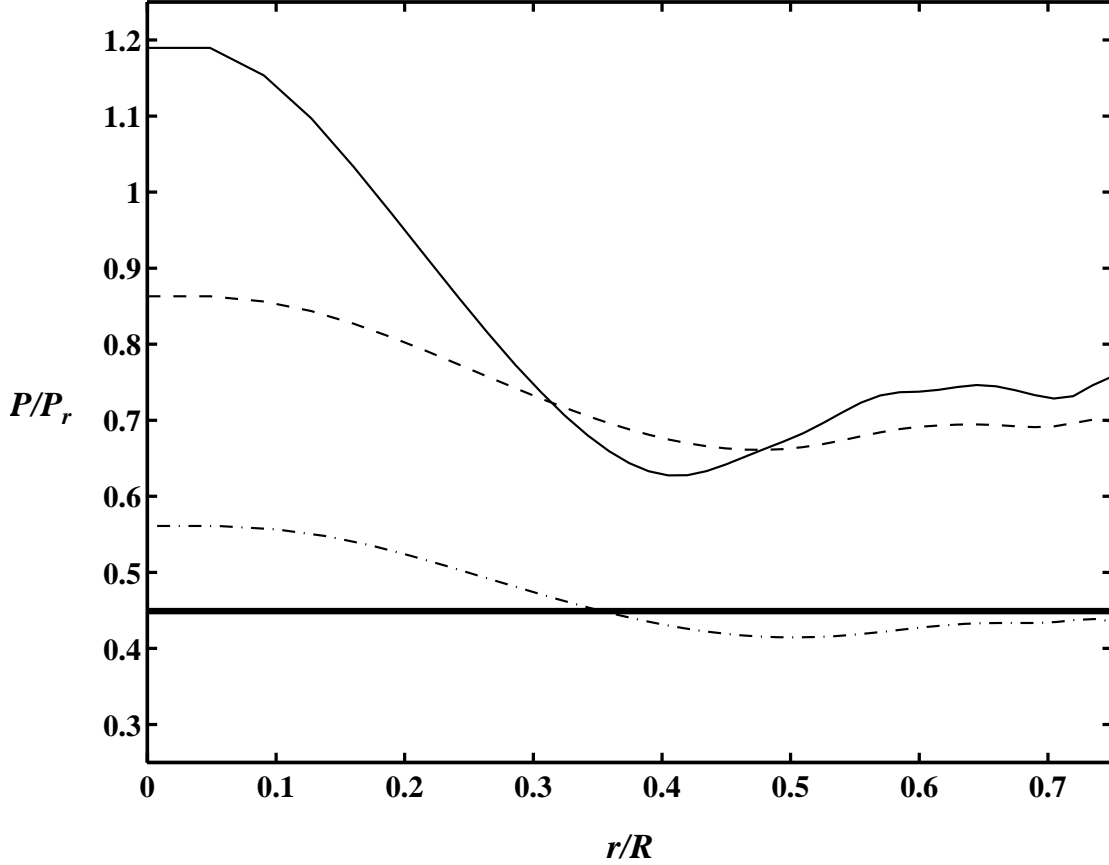


Figure 5.9: Effect of turbulence dissipation production level on base pressure distribution of the gas-only atomization flow (baseline settings). — : original Chien's k - ϵ model ($C_{\epsilon 1} = 1.35$); --- : 10% global reduction in \mathcal{P}_ϵ ($C_{\epsilon 1} = 1.215$); -.-.- : 20% global reduction in \mathcal{P}_ϵ ($C_{\epsilon 1} = 1.08$); **—** : experimental data (averaged value only), $P_{r_{exp}} = 98.574 \text{ kPa}$.

of the jet. In fact, at this 20% reduction level, the outer shear layer grows too fast ($x/R|_{num} \simeq 8$, $r/R|_{num} \simeq 2$ vs. $x/R|_{exp} \simeq 8$, $r/R|_{exp} \simeq 1.25$) and no shock waves are seen downstream from $x/R \simeq 3$.

In addition to the previously described simulations, two additional simulations were performed, using Yakhot *et al.* (1992) RNG k - ϵ model, and an *ad hoc* zonal variation in turbulence dissipation production given by,

$$C_{\epsilon 1} = \begin{cases} 1.215 & \text{for } x/R \leq 2R \\ 1.35 & \text{for } x/R > 2R \end{cases} \quad (5.2.1)$$

The RNG k - ϵ model proved to be more destabilizing than the original Chien k - ϵ model, increasing the local value of $C_{\epsilon 1}$ above the 1.35 threshold. The instability problem persisted even when the value of $C_{\epsilon 1}$ was prevented from rising above 1.35. The zonal variation of $C_{\epsilon 1}$ led to results very similar to those seen for the global 10% reduction case. However, it proved to be computationally 50% more expensive due to the implementation of the zonal variation as “*if*” statements. This prevented the vectorization of the RHS of the turbulence equations.

Based on all of the previous findings, the results presented hereafter were obtained with a global 10% reduction in the production of turbulence dissipation. The flow predictions obtained this way have a number of differences when compared with the real atomization flow. However, it is our belief that these estimates are as good as can be obtained using a k - ϵ turbulence model, and that they predict the trends with accuracy sufficient to allow for the parametrical study of the gas-only atomization flows.

5.3 Effects of jet pressure ratio

Some of the parameters listed in Table I are typically fixed by the design of the atomization nozzle assembly: R , r_o/R , α_{jet} , and α_{dt} . Others can be changed prior to the initiation of the atomization process: L_{dt}/R , r_{dt}/R , and the gas specie. However, a number of parameters can be changed *in situ*, providing the ability to modify the atomization process output based on some product quality measurement: P_r , P_e/P_r , T_r , and T_e/T_r . In this section, we study the effects of both jet pressure and temperature ratios on the topology of the gas-only atomization flow produced by the geometry shown in Figure 5.1. Such knowledge can be of assistance in the design of atomizers and in the development of control strategies

for them.

Figure 5.10 shows the aspiration behavior exhibited by the selected atomizer as a function of the jet pressure ratio. These results, which are typical of this type of atomizer (Ayers and Anderson 1985, Ting and Grant 1986, Ridder and Biancaniello 1988, Anderson *et al.* 1989), were recorded in the experimental facility used by Espina (1991). At each point, the experimental uncertainty of the data is no larger than the size of the symbols used in the plot.

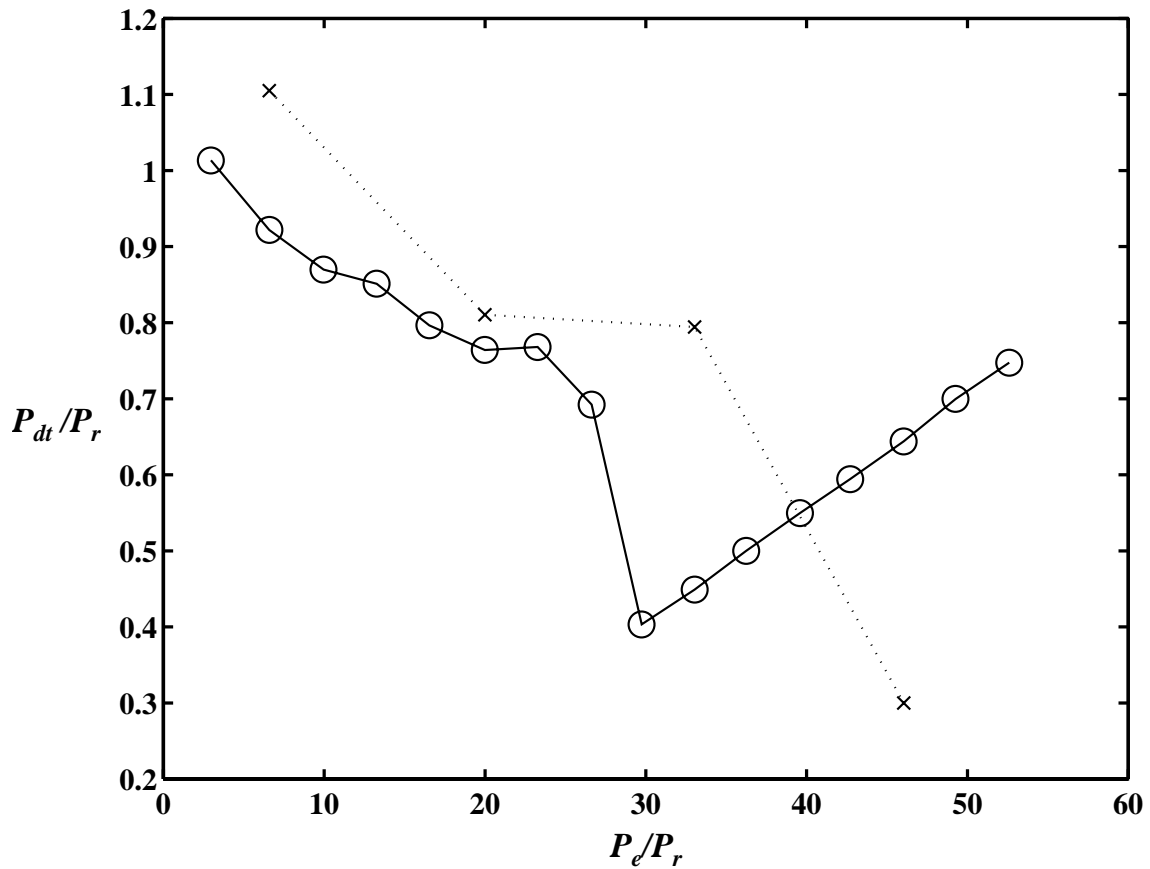


Figure 5.10: Effect of jet pressure ratio, P_e/P_r , on aspiration pressure, P_{dt}/P_r , for the selected close-coupled atomization nozzle assembly (baseline settings except as noted). \circ : experimental data, $P_{r_{exp}} = 98.574 \text{ kPa}$; \times : numerical results.

At low pressure ratios, $P_e/P_r < 5$, the liquid-delivery tube experiences a high aspiration pressure, $P_{dt}/P_r > 1$, that can lead to a “blow-back” condition (*i.e.*,

gas flowing into the liquid-delivery tube and bubbling through the liquid metal in the crucible, generally leading to a freeze-off). For mid-range pressure ratios, $5 < P_e/P_r < 25$, the liquid-delivery tube records ever decreasing aspiration pressures that plateau near $P_e/P_r \simeq 20$. For a narrow range of pressure ratios thereafter, $25 < P_e/P_r < 30$, the aspiration pressure decreases rapidly, leading to its minimum value, or maximum aspiration condition. Further increases in jet pressure ratio lead to linear increases in aspiration pressure, eventually leading to a second blow-back regime.

Numerically, we chose to model four jets at pressure ratios of $P_e/P_r = 6.6, 20, 33,$ and 46 . As seen in Figure 5.10, the simulations had severe difficulties in predicting the correct values of aspiration pressure while the trends are predicted fairly well; this was an expected result, given similar problems observed in the base flow simulations. However, Figure 5.11 shows that there is general agreement between the numerical and experimental jet structures over the entire pressure ratio range.

At $P_e/P_r \simeq 6.6$ (upper-left corner in Figures 5.11, 5.12, and 5.13), the annular portion of the jet displays three barrel-shocks before its transformation into a single jet at $x/R \simeq 2.05$. In the first of these barrel-shocks, the flow attains its maximum Mach number of 5.4. Upon its separation from the face of the liquid-delivery tube, the annular flow encapsulates a conically shaped region at the base of the liquid-delivery tube. This encapsulated flow draws momentum from the main flow across the inner shear layer, leading to relatively fast recirculating velocities inside of it ($\psi_{min} \simeq -0.035$). When this fast moving flow stagnates at the face of the liquid-delivery tube, the numerical prediction of aspiration pressure yields a 20% overprediction over the experimental data.

After its transformation into a single jet, the atomization flow continues down-

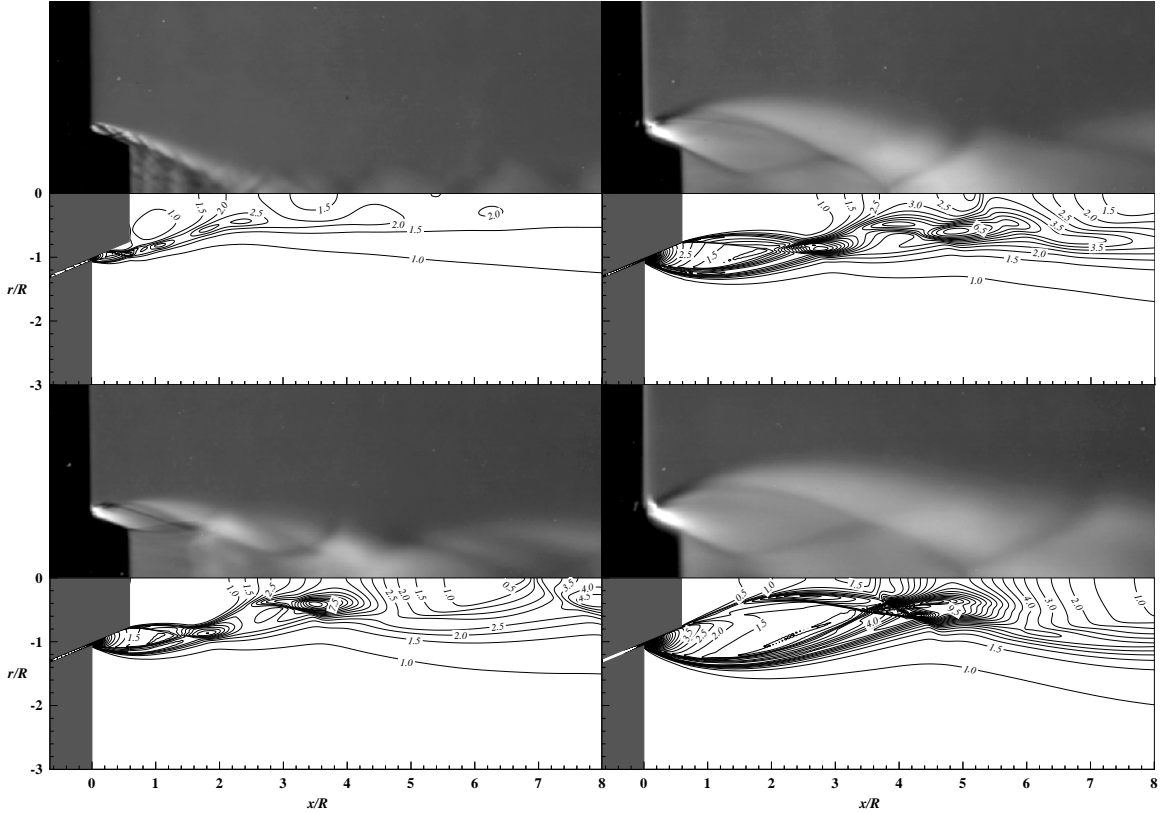


Figure 5.11: Effects of jet pressure ratio on the topology of gas-only atomization flows (baseline settings except as noted): experimental Schlieren pictures (upper images), numerical density distributions (lower images). TOP LEFT: $P_e/P_r \simeq 6.6$; BOTTOM LEFT: $P_e/P_r \simeq 20$; TOP RIGHT: $P_e/P_r \simeq 33$; BOTTOM RIGHT: $P_e/P_r \simeq 46$.

stream as a supersonic jet for as long as $x/R = 8$, displaying three additional barrel-shocks along that distance. The outer shear layer entrains little surrounding fluid and the jet shows little spreading, attaining a maximum radius of only $1.2R$ by $x/R = 8$.

For a pressure ratio of 20, (lower-left corner in Figures 5.11, 5.12, and 5.13) the annular portion of the flow contains two barrel-shocks: a complete one followed by the initial portion of a second one. The middle of the initial barrel-shock pinches the separation streamline giving it an hourglass shape. The flow reattaches at $x/R \simeq 2.80$ after the second barrel-shock intersects with the axis of symmetry. The

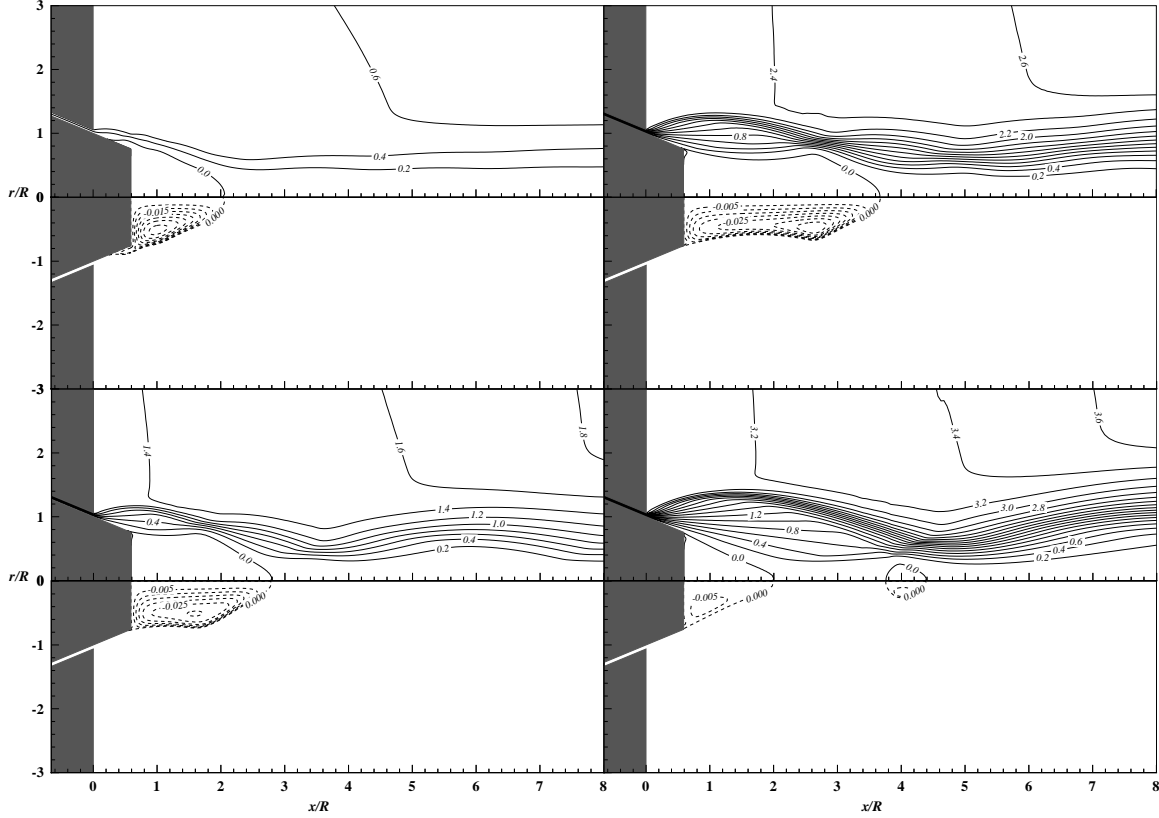


Figure 5.12: Effects of jet pressure ratio on the axisymmetric stream function distribution of gas-only atomization flows (baseline settings except as noted): $\psi^* = \psi / (\rho_r a_r R)$, $a_r = 319 \text{ m/s}$, $\Delta\psi^* = 0.2$ (upper images), $\Delta\psi^* = 0.005$ (lower images). TOP LEFT: $P_e/P_r \simeq 6.6$; BOTTOM LEFT: $P_e/P_r \simeq 20$; TOP RIGHT: $P_e/P_r \simeq 33$; BOTTOM RIGHT: $P_e/P_r \simeq 46$.

fluid trapped inside the separation region is driven at a lower velocity ($\psi_{min} \simeq -0.030$) than that seen in the $P_e/P_r \simeq 6.6$ jet. The slower circulation leads to the best estimate of aspiration pressure observed (6% overprediction). At this pressure ratio, the outer shear layer draws about twice as much fluid from its surroundings as the $P_e/P_r \simeq 6.6$ jet. The high entrainment, combined with a jet mass flow rate that is three times larger than the mass of the $P_e/P_r \simeq 6.6$ jet, yields a thicker jet with $\left. \frac{r_{max}}{R} \right|_{(x/R=8)} \simeq 1.5$.

At this pressure ratio of 20, the numerical results predict a maximum Mach number of 8.7 in the center of the first annular barrel-shock. This Mach number

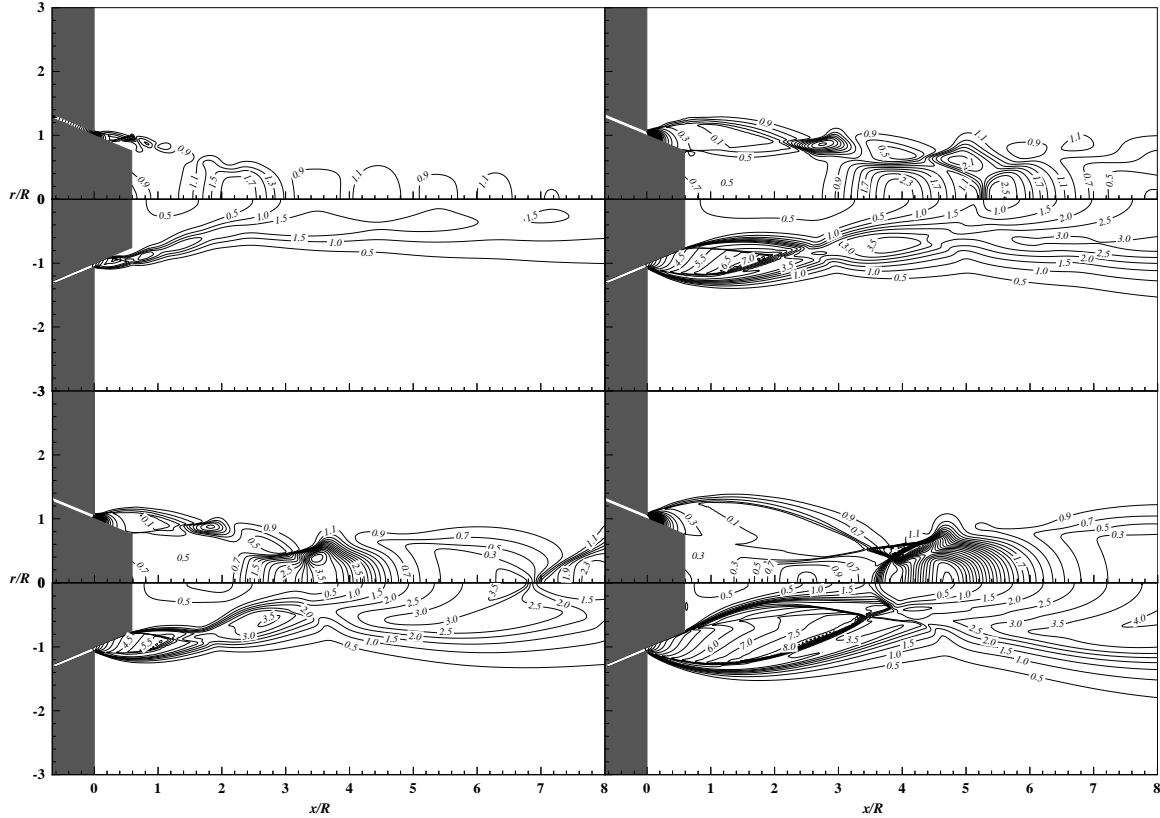


Figure 5.13: Effects of jet pressure ratio on static pressure and Mach number distributions of gas-only atomization flows (baseline settings except as noted): $P^* = P/P_r$, $\Delta P^* = 0.2$ (upper images), $\Delta M = 0.5$ (lower images). TOP LEFT: $P_e/P_r \simeq 6.6$; BOTTOM LEFT: $P_e/P_r \simeq 20$; TOP RIGHT: $P_e/P_r \simeq 33$; BOTTOM RIGHT: $P_e/P_r \simeq 46$.

value should be viewed as inaccurate given that the mathematical formulation may fail at hypersonic speeds. However, in what follows, we will continue to report the maximum Mach number as a means of comparison between the jets at the various pressure ratios.

The baseline jet, $P_e/P_r \simeq 33$ (upper-right corner in Figures 5.11, 5.12, and 5.13), also shows a complete barrel-shock followed by a partial one in the annular portion of the flow, $x/R < 3.65$. Inside the initial barrel-shock, the numerical simulation predicts a maximum Mach number of 10.9; although inaccurate for the reasons previously stated, this value is 25% larger than the maximum Mach number seen

in the $P_e/P_r \simeq 20$ jet.

For this jet, the arrangement of the annular barrel-shocks places the “fat” portion of the initial one (*i.e.*, the middle portion of it) near the middle of the separation bubble leading to a longer and narrower separation region than those seen before. The larger surface area of the separation bubble, combined with its pronounced pinching in the middle, provides for higher momentum flux into the separation region. This leads to higher circulation speeds inside the bubble inducing a large aspiration pressure (76% overprediction).

At this pressure ratio ($P_e/P_r \simeq 33$), the annular wave structure persists beyond the reattachment point, changing to a single jet wave structure at $x/R \simeq 5.2$. When the annular wave structure finally meets the axis of symmetry, it forms a Mach reflection. For this pressure ratio, the flow entrainment is reduced a bit when compared to that seen in the $P_e/P_r \simeq 20$ jet. The lower entrainment yields a jet with a $\frac{r_{max}}{R}|_{(x/R=8)} \simeq 1.7$ even though the jet carries 65% more mass than its lower pressure ratio counterpart, with a maximum Mach number of 10.9.

The structure of the high pressure ratio jet, $P_e/P_r \simeq 46$, is different in many ways from its lower pressure ratio partners. At this pressure ratio, the annular flow only contains one barrel-shock with the “fat” portion of it forcing the inner shear layer very close to the axis of symmetry. This leads to a very short, conically-shaped separation bubble ($x/R < 2$) with a small surface area that allows for little momentum flux across the inner shear layer. As a result, the speed of the fluid inside the bubble is very low and this yields a low prediction in aspiration pressure (53% underprediction of the experimental value). Inside the initial barrel-shock, the flow reaches its maximum Mach number of 12.3.

Not seen in the lower pressure ratio cases is the formation of a second recirculation

bubble centered around $x/R \simeq 4$. This secondary recirculation is caused by a strong Mach reflection, at $x/R \simeq 3.6$, which decelerates the flow moving along the axis of symmetry. A bit downstream, the projection of this Mach reflection crosses the two shock waves emanating from the outer and inner shear layers, leading to the formation of a triple shock wave.

At this pressure ratio, the entrainment increases, drawing as much surrounding fluid as the $P_e/P_r \simeq 20$ jet. The additional entrainment, combined with a 28% increase in mass flow from the $P_e/P_r \simeq 33$ jet levels, leads to a $\left. \frac{r_{max}}{R} \right|_{(x/R=8)} \simeq 2.0$. However, at this distance, the jet spreading rate is still under the strong local influence of the barrel-shock structures, and this radius is a function of the inviscid flow structure as much as it is a function of the flow entrainment.

A yet not mentioned detail of these jets is the flow separation that occurs over the outer surface of the liquid-delivery tube for some conditions. This separation, which is a function of jet pressure ratio and liquid-delivery tube extension, has been experimentally shown (Ridder *et al.* 1992) to draw liquid metal from the face of the liquid-delivery tube into its outer surface, where it is exposed to the very cold expanding gas of the annular wall jet. The extreme temperature difference between the metal and the gas promotes the solidification and accumulation of metal, leading to a shape alteration of the liquid-delivery tube. Typically, this sequence of events induces a freeze-off that prematurely ends the atomization process and often leaves behind expensive super alloy to be reprocessed. Therefore, this separation is of detrimental consequence to the process of gas-metal atomization and should be avoided at all cost.

Figure 5.14 shows the skin friction coefficient, C_f , over the surface of the liquid-delivery tube as a function of advanced surface distance, $s = x/\cos(\alpha_{dt})$, for the

four studied jet pressure ratios. For all pressure ratios, the friction coefficient increases early in the length of the liquid-delivery tube due to the flow acceleration caused by the expansion fans emanating from the end lip of the annular channel (see Figure 5.15). From there on, the friction coefficient decays smoothly as the wall jet boundary layer loses momentum to friction.

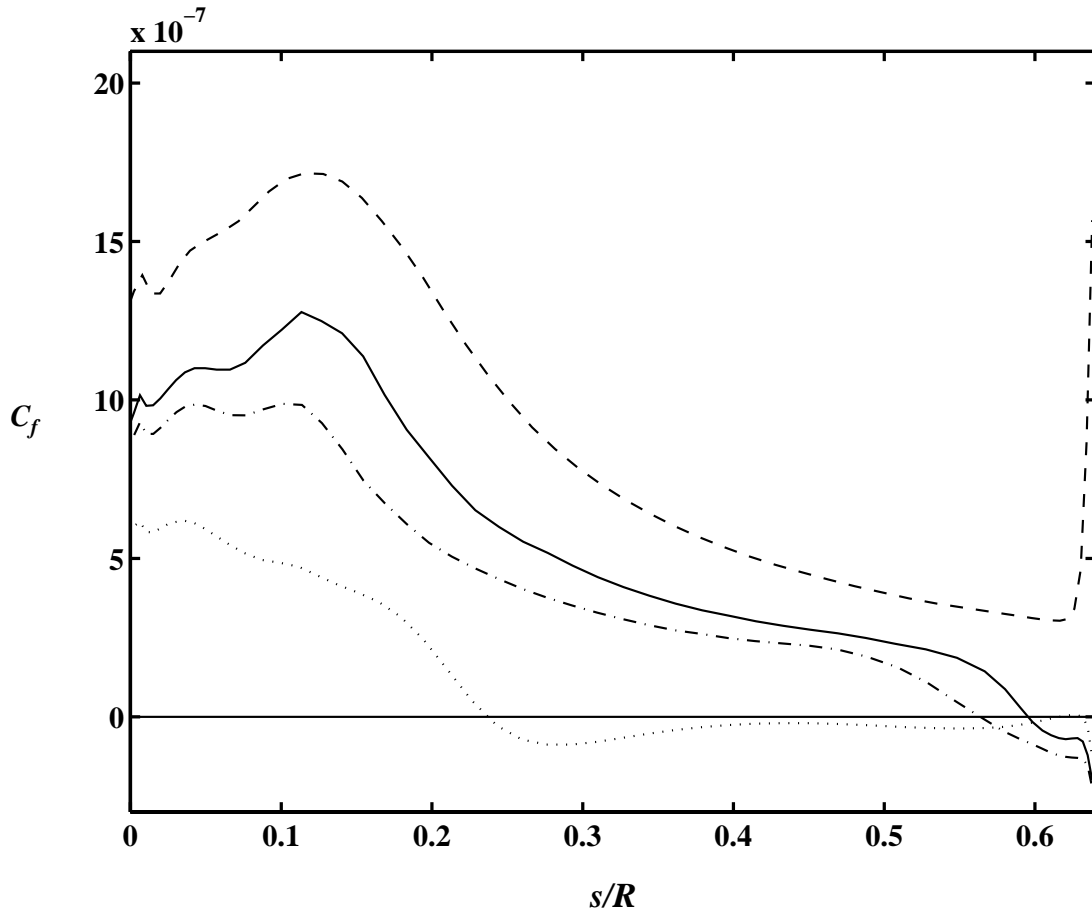


Figure 5.14: Effect of jet pressure ratio on flow separation over the liquid-delivery tube (baseline settings except as noted): $C_f = 2\tau_w/\rho_r a_r^2$. \cdots : $P_e/P_r \simeq 6.6$; $-\cdot-$: $P_e/P_r \simeq 20$; $—$: $P_e/P_r \simeq 33$; $---$: $P_e/P_r \simeq 46$.

For a low pressure ratio, $P_e/P_r \simeq 6.6$, the simulation predicts that the flow will separate at the early distance of $s/R \simeq 0.24$. This separation is likely to induce drawing of the liquid metal over the surface of the liquid-delivery tube which could lead to a freeze-off. For intermediate pressure ratios, $P_e/P_r \sim 20$ and

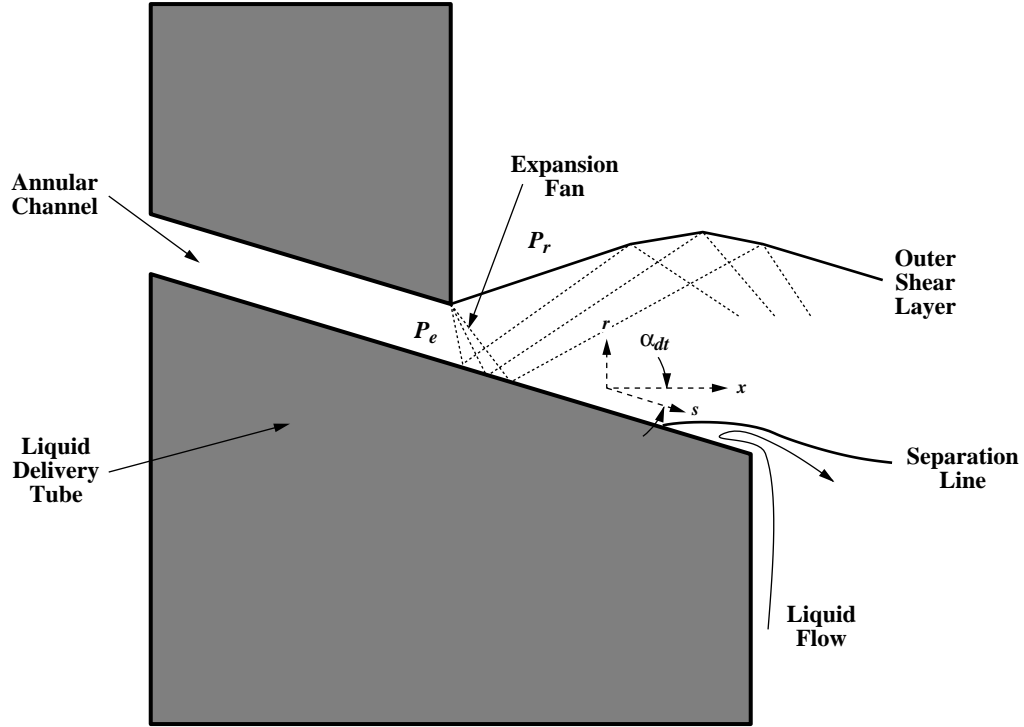


Figure 5.15: Schematic diagram of the separation phenomenon at the end of the liquid-delivery tube.

33, the separation takes place in the neighborhood of $s/R \simeq 0.6$ and the friction coefficient becomes substantially negative, enhancing the drawing of liquid metal up the surface of the liquid-delivery tube and possibly leading to a freeze-off even faster than the flow at $P_e/P_r \simeq 6.6$. If an atomizer is intended to operate in this pressure ratio range, it would be advisable to limit the length of the liquid-delivery tube, L_{dt}/R , to no more than the separation distance predicted by the simulations.

At the high pressure ratio, $P_e/P_r \simeq 46$, the friction coefficient, C_f , never becomes negative before the end of the liquid-delivery tube. Near the end of the liquid-delivery tube, the friction coefficient increases rapidly due to the second expansion fan that forms at the end of the liquid-delivery tube. This second expansion process is instrumental in the determination of the aspiration pressure at these high pressure ratio values.

The observed behavior leads to the following phenomenological model of the aspiration phenomenon that describes the behavior experimentally, shown in Figure 5.10. For mid-range pressure ratios, $P_e/P_r < 20$ (**decreasing P_{dt}/P_r range**), the flow over the liquid-delivery tube separates early on but reattaches before the end of the wall jet. The decrease in aspiration pressure with increasing jet pressure ratio is the result of an ever larger expansion level due to the increasing underexpansion of the wall jet. At pressure ratios between 20 and 25 (**plateau in P_{dt}/P_r range**), the flow separates but never reattaches, leading to an aspiration pressure level that is controlled by the dynamics of the flow in the hourglass shaped separation bubble. For higher pressure ratios, $P_e/P_r > 25$ (**increasing P_{dt}/P_r range**), the flow never separates from the face of the liquid-delivery tube and a second expansion fan forms at its end. This second expansion controls both the shape of the separation region and the aspiration pressure. The higher the pressure ratio goes, the higher the pressure before the second expansion process will be. Given that the turning angle at the end of the liquid-delivery tube is constant, the second expansion process will yield ever smaller separation regions with ever increasing aspiration pressures.

5.4 Effects of jet temperature ratio

In some metal powder production facilities, the gas supply is preheated³ in an attempt to decrease the thermal shock that the ceramic liquid-delivery tube experiences as a consequence of its contact with the hot liquid metal and the cold gas wall jet. The practice of gas preheating, although expensive and difficult to implement, has also been justified on the basis that it increases the energy available

³Gas stagnation temperatures as high as 700 K are typical in industrial atomization facilities.

in the gas to disrupt the metal liquid. Therefore, it can lead to the formation of finer powders. In this section, we examine, numerically, the effects of jet stagnation temperature by comparing the baseline atomization flow (see Table I) with a similar flow at a stagnation temperature twice as high.

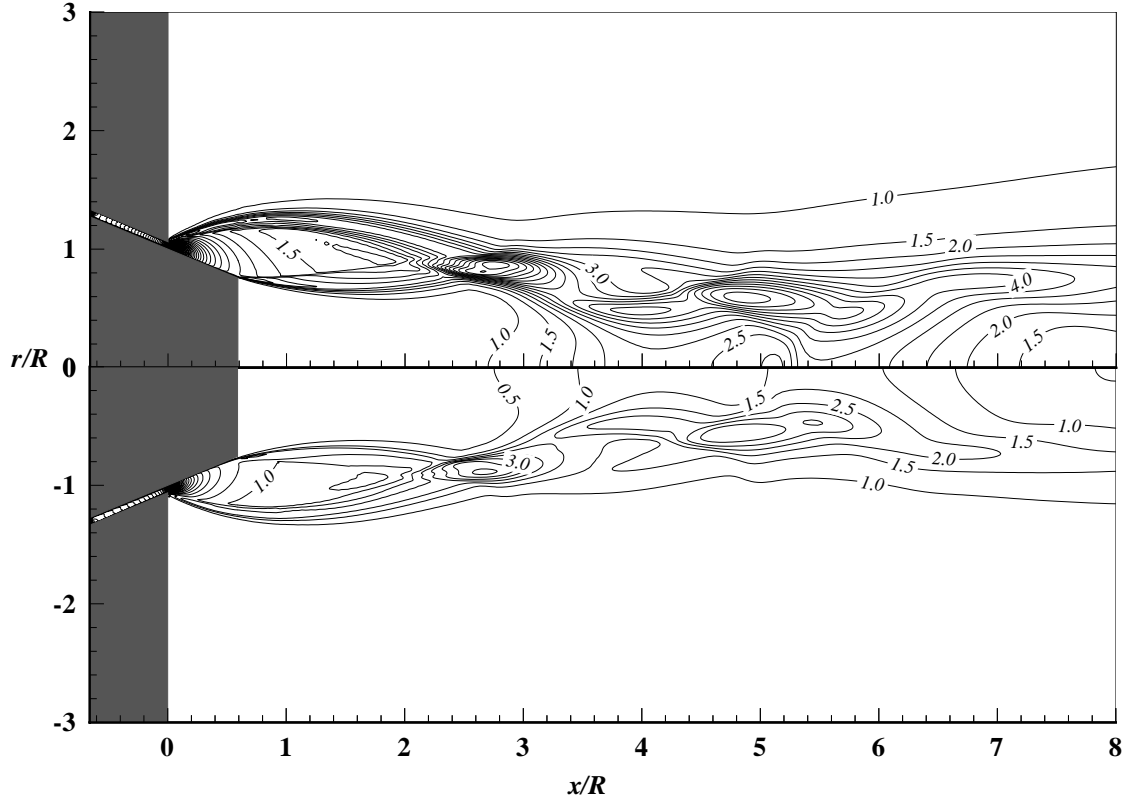


Figure 5.16: Effects of jet temperature ratio on the density distribution of gas-only atomization flows (baseline settings except as noted): $\Delta\rho^* = 0.5$. TOP: $T_e/T_r = 0.65$; BOTTOM: $T_e/T_r = 1.31$.

Figure 5.16 compares the density distributions of the **cold** (*i.e.*, baseline flow, $T_e/T_r=0.65$) and **hot** (*i.e.*, $T_e/T_r=1.31$) gas-only atomization flows. As expected, the basic structure of the jet remains unchanged, given that it is controlled by the inviscid portion of the flow, which is only a function of the pressure ratio. The density of the hot flow has changed in a manner inversely proportional to the change in temperature (*i.e.*, $\rho_{hot}/\rho_{cold} = T_{cold}/T_{hot} = 1/2$). However, given that

the Mach number distribution remains unchanged and that the speed of sound scales with the square root of the stagnation temperature, the speed of the fluid has increased only proportional to the square root of the temperature increase (*i.e.*, $|V|_{hot}/|V|_{cold} = \sqrt{T_{hot}/T_{cold}} = \sqrt{2/1}$). This leads to a net loss of momentum in the flow field of 29% (*i.e.*, $1 - \sqrt{2}/2$), probably reducing the ability of the hot flow to disrupt the liquid metal effectively. The loss in momentum can be graphically seen in Figure 5.17, where the streamlines of both flows are seen to have the same shape. However, the number of streamlines has been reduced by 27% with the doubling in stagnation temperature. The hot jet appears to entrain about 33% more fluid than the cold jet, even though it carries 29% less mass than its cold counterpart. The increased entrainment is not sufficient to boost the jet spreading rate of the hot flow, whose diameter is 32% smaller by $x/R \simeq 8$ than that of the cold jet.

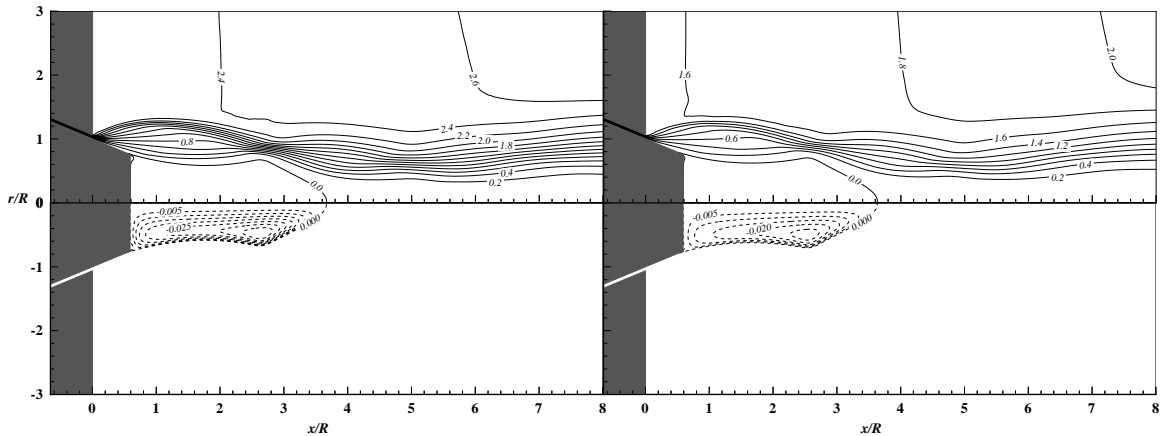


Figure 5.17: Effects of jet temperature ratio on the axisymmetric stream function distribution of gas-only atomization flows (baseline settings except as noted): $\Delta\psi^* = 0.2$ (upper images), $\Delta\psi^* = 0.005$ (lower images). LEFT: $T_e/T_r = 0.65$; RIGHT: $T_e/T_r = 1.31$.

The higher temperature does appear to delay the separation of the wall jet over the liquid-delivery tube. Figure 5.18 shows how the hot gas flow does not experi-

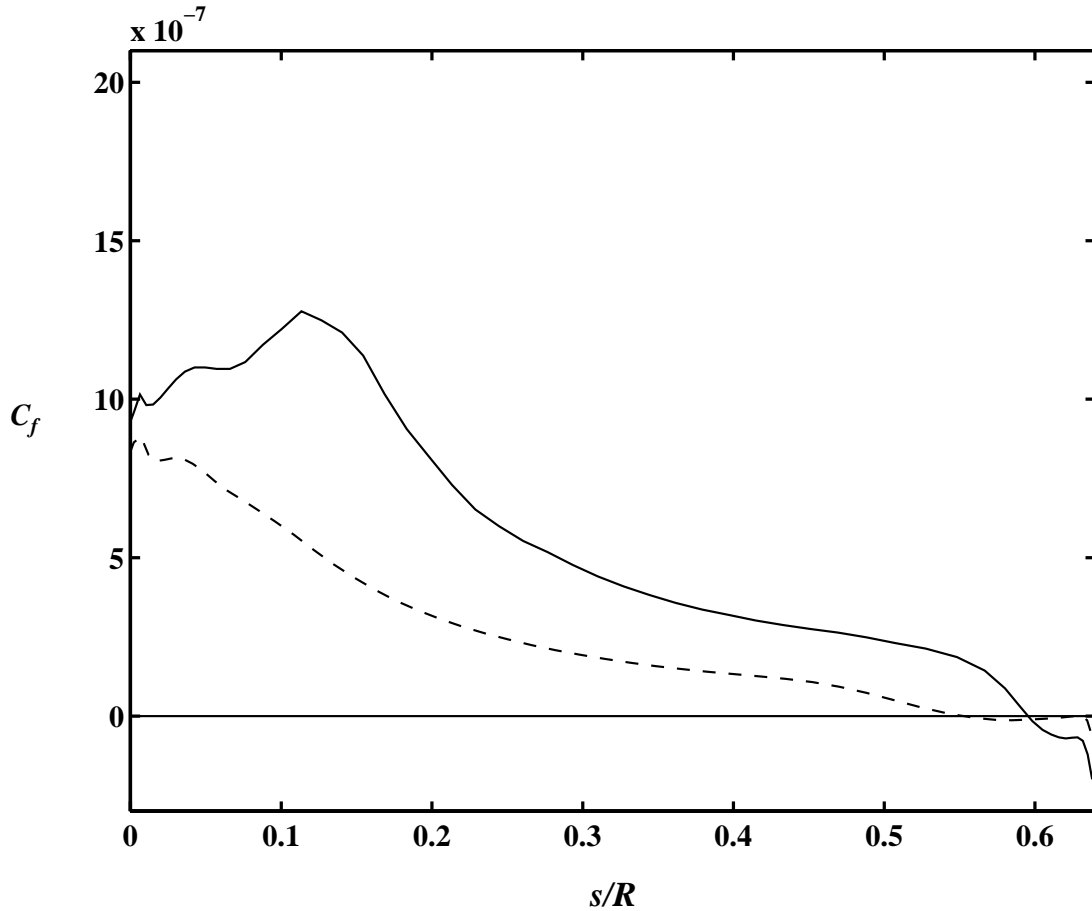


Figure 5.18: Effect of jet temperature ratio on flow separation over the liquid-delivery tube (baseline settings except as noted): $C_f = 2\tau_w/\rho_r a_r^2$. — : $T_e/T_r = 0.65$; --- : $T_e/T_r = 1.31$.

ence the increase in skin friction velocity early in the length of the liquid-delivery tube that the cold jet displayed. Overall, the hot wall jet, with its lower momentum, imposes less drag on the surface of the liquid-delivery tube than the cold jet, however, its lower momentum leads to earlier separation than in the cold jet.

In addition, the higher stagnation temperature does improve the thermal conditions over the surface of the liquid-delivery tube. As seen in Figure 5.19, doubling the stagnation temperature yields an almost constant doubling of the temperature over the liquid-delivery tube. Given the disparity in temperatures inside and outside of the ceramic liquid-delivery tube, this wall temperature increase could

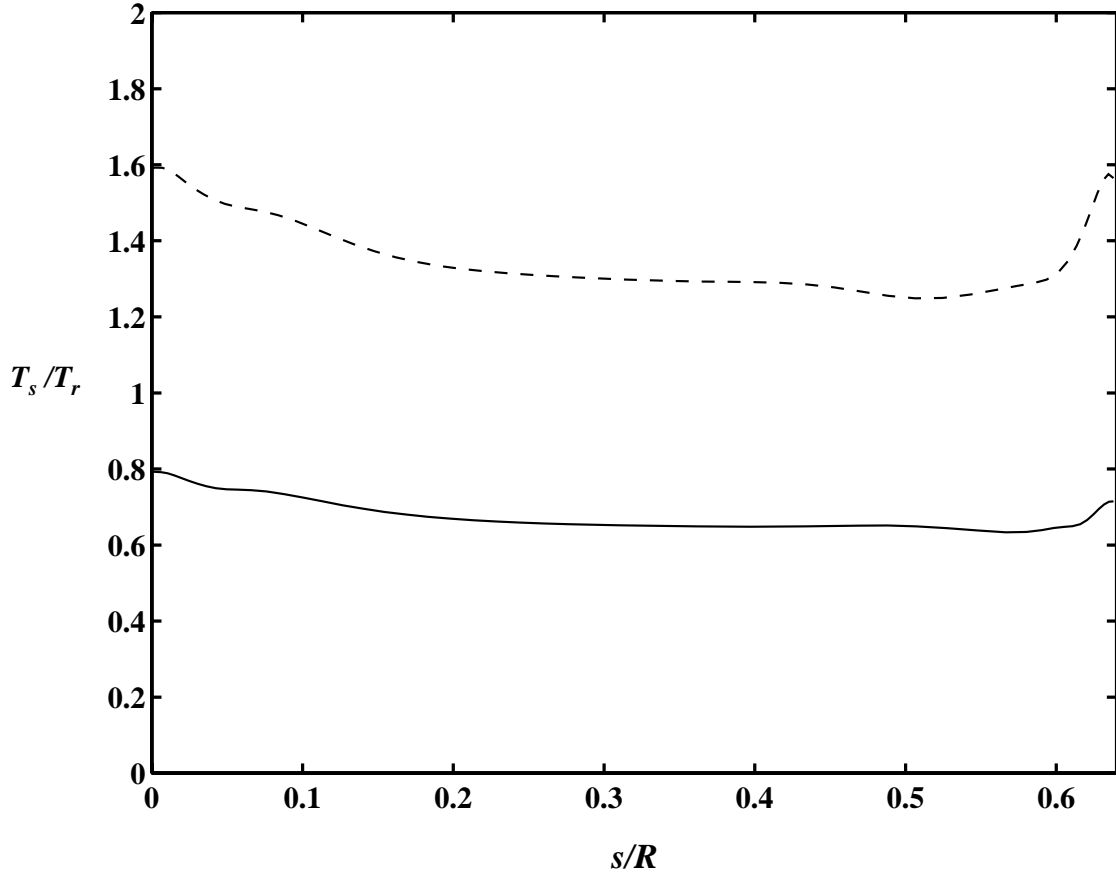


Figure 5.19: Effect of jet temperature ratio on the liquid-delivery tube surface temperature (baseline settings except as noted). — : $T_e/T_r = 0.65$; --- : $T_e/T_r = 1.31$.

improve the structural integrity for some ceramic materials with good erosion properties but deficient thermal shock properties (properties often encountered among the materials used to manufacture liquid-delivery tubes).

5.5 Effects of base mass injection

The physics of liquid disruption are not well understood and this renders the numerical simulation of the full gas-metal atomization phenomenon all but impossible at present. However, the introduction of the dense liquid metal at the base of the liquid-delivery tube will undoubtedly change the character of the gas-only

atomization flows described in the previous section. In this section, we set out to investigate the effects that the liquid metal flow may have on the atomization flow by modeling the baseline gas-only flow with mass injection at the base of the liquid-delivery tube; this mass injection takes the form of a hot gas stream (*i.e.*, $T = T_{metal} \simeq 1650 \text{ K}$) introduced through the liquid delivery channel (see Figure 5.3). Two injection rates are studied: $\dot{m}_{dt}/\dot{m}_{jet} = 0.0013$ (momentum flux matched flow), and $\dot{m}_{dt}/\dot{m}_{jet} = 0.0041$ (pressure driven flow).

Nickel based super alloys have liquid densities that are about 4500 times larger than the density of argon at standard conditions. This disparity in density makes it impossible to investigate liquid injection effects using argon as a surrogate fluid. However, observing that the liquid is drawn into the atomization process at a very low velocity ($\bar{u}_{liq} \simeq 1.2 \text{ m/s}$), it is possible to investigate the injection effects using a gas injection velocity that yields the same momentum-flux as the liquid. For the baseline flow, this injection rate that yields such conditions is $\dot{m}_{dt}/\dot{m}_{jet} = 0.0013$; its effects on the gas-only flow field are shown at the center of Figure 5.20.

The mass injection pushes the upstream portion of the separation bubble downstream, moving the stagnation point away from the base of the liquid-delivery tube to an axial distance of $x/R \simeq 0.8$. In contrast, the mass addition has little effect on the surrounding annular jet flow, which forces the end of the separation bubble to be located at just about the same place as in the baseline flow. The resulting reduction in the surface area of the separation bubble leads to the deceleration of the flow inside of it due to a reduction in the area available for momentum transfer across the inner shear layer. The additional fluid is rapidly entrained by the inner shear layer (before $x/R \simeq 1$) and thereafter, the flow remains all but unaffected by the mass injection.

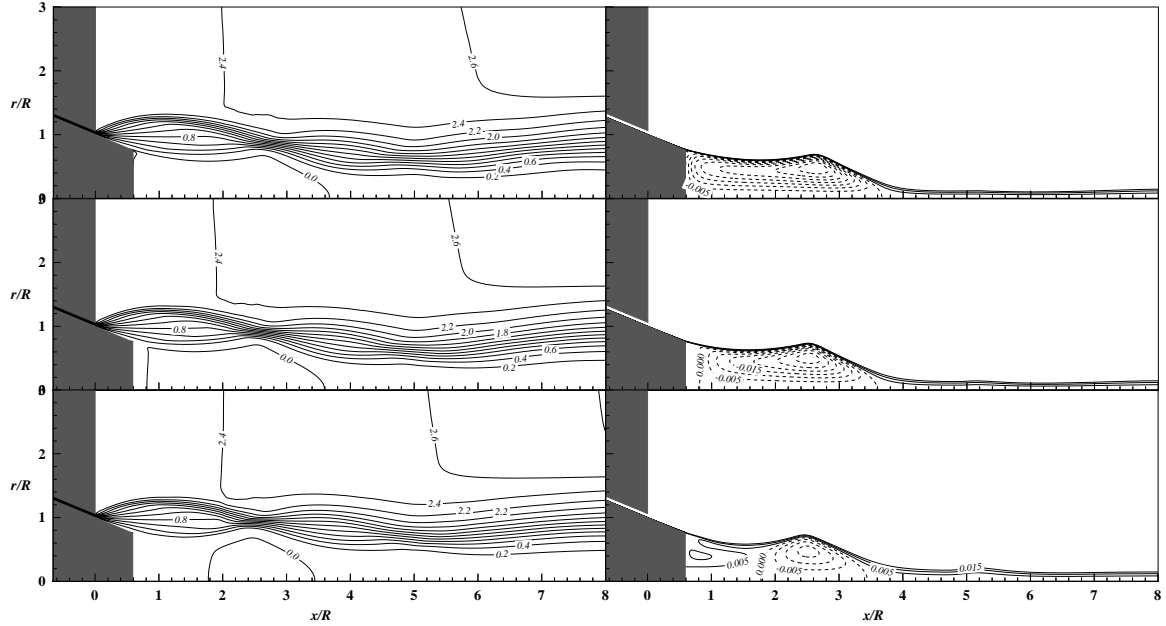


Figure 5.20: Effects of liquid-delivery tube mass injection on the axisymmetric stream function distribution of gas-only atomization flows (baseline settings except as noted): $\Delta\psi^* = 0.2$ (left images), $\Delta\psi^* = 0.005$ (right images). TOP: $\dot{m}_{dt}/\dot{m}_{jet} = 0$; CENTER: $\dot{m}_{dt}/\dot{m}_{jet} = 0.13\%$; BOTTOM: $\dot{m}_{dt}/\dot{m}_{jet} = 0.41\%$.

The impact of a mass injection rate three times larger was also tested. The results of this simulation are shown at the bottom of Figure 5.20. At this rate of injection, the separation point at the near-side of the separation bubble moves further downstream to an axial location of $x/R \simeq 1.8$. The resulting separation bubble is smaller than that seen at the lower injection rate and this leads to even slower recirculation velocities inside it. As before, the inviscid flow of the annular jet continues to dominate the shape and location of the far-side of the bubble which remains undisturbed. The streamline labeled $\psi^* = 0.005$ (Figure 5.20 bottom right) shows that at this injection rate, the injected flow has enough momentum to form a hot jet, of radius r_{dt} , which propagates from the end of the liquid-delivery tube to the separation point. At this location, the hot jet is drawn into the inner shear layer by its lower pressure. It is then absorbed into the main flow stream.

The flow bounded by the $\psi^* = 0$ and $\psi^* = 0.005$ streamlines has a mushroom-like shape that is similar to that seen before in high-speed movies of the liquid flow during atomization (Ridder *et al.* 1992). This may indicate that a recirculation bubble, similar to the one seen here, may remain present during gas-metal atomization. The existence of the hot jet leads to the formation of a toroidal-shaped recirculation region centered at $x/R \simeq 0.8$, $r/R \simeq 0.4$. This recirculation region contains very slow moving fluid and its circulation is counter-clockwise, opposite in direction to that in the separation bubble. Finally, neither injection rate appeared to modify the gas wall jet flow over the liquid-delivery tube in any significant way.

5.6 Summary

An evaluation of the results yielded by Chien's $k-\epsilon$ model for the baseline atomization gas-only flow (see Table I) led us to the conclusion that the model underpredicts the production of turbulence dissipation rate in this flow. Upon modeling the flow using reduced values of the $C_{\epsilon 1}$ parameter, we concluded that a 10% reduction in the production of turbulence dissipation yields the predictions in best agreement with the real flow. Other attempts at improving the quality of the numerical results by means of local variations of $C_{\epsilon 1}$ and by the use of Yakhot *et al.* (1992) RNG model proved less satisfactory.

Using a 10% reduced value of $C_{\epsilon 1}$, simulations were carried out to determine the effects of jet pressure ratio on the topology of the gas-only atomization flow. Four pressure ratios were selected – $P_e/P_r = 6.6, 20, 33, 46$. These results showed that the numerical method had problems predicting the experimental value for aspiration pressure. However, the resulting jet structure was shown to be in good qualitative agreement with experimental Schlieren pictures.

The $P_e/P_r = 6.6$ results yielded a 20% overprediction in aspiration pressure. The flow was shown to be supersonic well past the transformation length from annular to single jet. The shape of the separation region at the base of the liquid-delivery tube was shown to have a conical shape predicting a reattachment point at $x/R \simeq 2.05$. At $P_e/P_r = 20$, results yielded the best prediction of aspiration pressure with an overprediction of only 6% over the experimental value. It was seen that the annular jet flow places the “fat” portion of the first barrel-shock over the separation bubble, forcing the separation streamline into an hourglass shape. The reattachment point was predicted to be located at $x/R \simeq 2.8$. The $P_e/P_r = 33$ jet overpredicted the aspiration pressure by as much as 76%. The separation bubble became more elongated, forcing the reattachment point to $x/R \simeq 3.65$. A Mach reflection was shown to form at the interaction between the annular wave structure and the axis of symmetry; from that point on, the flow attains a wave structure similar to that seen in single supersonic jets. At $P_e/P_r = 46$, the “fat” portion of the first annular barrel-shock comes very close to the axis of symmetry, forcing a reduction in the length of the separation region ($x/R \simeq 2.0$). The resulting conical separation region allows for little momentum transfer from the inner shear layer, leading to a 53% underprediction in the aspiration pressure. Downstream from the reattachment point, the flow encounters a strong Mach reflection that leads to the formation of a small recirculation region centered around $x/R \simeq 4.0$. The interaction between the tail of the Mach reflection and the two shock waves produced at the first barrel-shock leads to the formation of a triple-shock structure.

The results showed that the wall jet flowing over the liquid-delivery tube separated for a certain set of conditions leading to a possible freeze-off condition. At low pressure ratios, the flow separates early in the length of the liquid-delivery tube

but reattaches before its end. This would prevent the drawing of liquid metal into the surface of the liquid-delivery tube. At intermediate pressure ratios, the flow separates and never reattaches, leading to the possibility of freeze-off. For large pressure ratios, the flow never separates and forms an expansion fan at the end of the liquid-delivery tube. The separation behavior here described, in conjunction with the observed jet structure, leads to a phenomenological model which describes the observed experimental aspiration behavior.

The effects of gas heating were studied by simulating the gas-only atomization flow that results when the jet temperature ratio is doubled (*i.e.*, $T_e/T_r = 1.31$). The hot jet was shown to have less momentum than the cold flow, which suggests that heating may be detrimental to the formation of fine metal powder. The additional heat was shown to have the effect of enhancing the chances for separation over the surface of the liquid-delivery tube. In addition, it was shown that doubling the jet temperature ratio leads to a doubling of the wall gas jet which may improve conditions to avoid thermal shock of the liquid-delivery tube material.

The effects that the liquid flow may have over the gas-only flow during atomization were studied by modeling the gas-only flow with hot gas mass injection at the base of the liquid-delivery tube. Two rates of injection were tested: one matching the momentum flux of the liquid, and the other having a mass flow three times as large as the first. The momentum-matched injection flow was shown to have little effect over the topology of the main gas-only flow, aside from moving the separation bubble a bit downstream. The high mass-injection flow led to further movement of the separation bubble downstream. Furthermore, the injected flow took the form of a jet projecting out of the base of the liquid-delivery tube. It then blossomed into a mushroom-shaped structure similar to that seen in the liquid

metal via high-speed movies of the atomization process.

Chapter 6

Conclusions

The objective of this investigation was to conduct a numerical study of the compressible gas-only flows used in gas-metal atomizers. To achieve this goal, studies were conducted in flows progressively similar to the atomizer flow to develop the necessary methodology needed. The following is a summary of the findings of this investigation and some conclusions drawn from it.

Both subsonic and supersonic two-dimensional boundary layers were used to assess the performance of three eddy-viscosity turbulence models [Baldwin-Lomax (1972), Chien (1982), and Grasso-Falconi (1993)] in conjunction with the NPARC code. Simulations demonstrated deficiencies in the NPARC implementation of the Baldwin-Lomax turbulence model, which yield discontinuous eddy viscosity distributions in wall bounded flows. With the addition of the wake model proposed by Baldwin and Lomax (1972) and a trapezoidal filter, the performance of the model improved.

The $k-\epsilon$ model by Grasso-Falconi (1993) yielded unsatisfactory results for boundary layers over a wide range of free stream Mach numbers. The problems seen with

this model appear to be due to large values of turbulent dissipation near the wall and the dissipative nature of additional compressibility terms. With attention to discretization details, the k - ϵ model by Chien gave results in agreement with DNS data for boundary layer flows and with experiments involving base flows.

Results obtained for the supersonic base flow were in acceptable agreement with the experimental data and results from previous numerical investigations. Local values of base pressure were found to differ from their experimental counterparts by as much as 22%. The location of the reattachment point was overpredicted by 30% due to a smaller than expected growth of the inner shear layer.

The magnitude of the base pressure was found to be inversely proportional to the jet pressure ratio, even though the function appears to be nonlinear. The axial locations of jet structures were found to be directly proportional to the jet pressure ratio. However, the location of the reattachment point follows the inverse behavior. This effect is associated with the strength of the expansion process at the end-corner of the circular cylinder which deflects the inner shear layer at sharper angles for higher pressure ratios.

Improvements of the numerical prediction for the base flow were attained by reducing the production of turbulence dissipation by 10% from the values prescribed by Chien. At this level of turbulence dissipation, the numerical prediction of the reattachment location matched that of the experiments. Although there was a small degradation in the prediction of the base pressure distribution and an increase in the shear layer spreading rates, the overall agreement with the experimental findings was improved by the reduction in turbulence dissipation production.

The methodology used to obtain the base flow results was then applied to model

the gas-only flow fields in close-coupled gas-metal atomizers; these devices generate flow fields similar to the base flow. An evaluation of the results yielded by Chien's $k-\epsilon$ model for the baseline gas-only atomization flow (see Table I) led us to the conclusion that the model underpredicts the production of turbulence dissipation in the flow. Upon modeling the flow using reduced values of the $C_{\epsilon 1}$ parameter, we concluded that a 10% reduction in the production of turbulence dissipation yields predictions that are in best agreement with the real flow. Other attempts at improving the quality of the numerical results by means of local variations of $C_{\epsilon 1}$ and by the use of Yakhot *et al.* (1992) RNG model proved less satisfactory.

Using a 10% reduced value of $C_{\epsilon 1}$, simulations were carried out to determine the effects of jet pressure ratio on the topology of the gas-only atomization flow. Four jet pressure ratios were selected, $P_e/P_r = 6.6., 20, 33, 46$. These results showed that the numerical method had problems predicting the experimental value for aspiration pressure. However, the resulting jet structure was shown to be in good qualitative agreement with experimental Schlieren pictures.

Even though Couper and Singer (1985), and Ayers and Anderson (1985) reported that the finest powder in their atomizers was produced at the maximum aspiration condition, experimental evidence suggests otherwise. Industrial facilities that produce nickel-based super-alloys report that the particle size distribution of their powder tends to decrease with increasing gas-metal ratio, although the effect is not linear. This suggests that the total availability of gas-momentum in the flow field may be more important to the dynamics of liquid disruption than the structure of the gas-only flow. Therefore, we suggest that the design of an atomization nozzle assembly which maximizes gas momentum prior to the interaction with the liquid metal, may be advantageous; an example of one such design has been suggested

by Mates and Settles (1996) which uses the curvature of the liquid-delivery tube to maximize gas expansion. Furthermore, we suggest that operating this device at high pressure ratios in the increasing P_{dt}/P_r range may further enhance the production of fine powders by increasing the gas-metal ratio and decreasing the volume of the separation region. This reduction of the separation region volume leads to steeper angles of interaction between the gas and metal streams. Furthermore, the operation of the atomizer in the increasing P_{dt}/P_r range has been shown to guarantee against gas separation at the end of the liquid-delivery tube, avoiding the costly possibility of a freeze-off. Finally, the structure of the gas flow and the aspiration phenomenon in the increasing P_{dt}/P_r range have been shown to scale linearly, enabling the application of simpler atomization control strategies.

The results also showed that the wall jet flowing over the liquid-delivery tube separated for a certain set of conditions leading to a possible freeze-off condition. Given the severe consequence of flow separation over the liquid-delivery tube for the atomization process, it is advisable to make use of liquid-delivery tube lengths that are shorter than that which will yield flow separation at the desired pressure ratio. The separation behavior seen, in conjunction with the observed jet structure, lead to a phenomenological model which describes the observed experimental aspiration behavior.

The effects of gas heating were studied to determine the effects of this industrial practice on the gas-only atomization flow. Hot jets were shown to have less momentum than their cold counterparts which suggests that heating may be detrimental to the formation of fine metal powder. The additional heat was shown to have the effect of enhancing the chances for separation over the surface of the liquid-delivery tube. In addition, it was shown that increasing the jet temperature ratio leads to

a proportional increase in the wall gas jet which may improve conditions to avoid thermal shock of the liquid-delivery tube material. In our opinion, the practice of gas-heating should be avoided unless the need to preserve the structural integrity of the liquid-delivery tube material requires it.

The effects that the liquid flow may have on the gas-only flow during atomization were studied by modeling the gas-only flow with hot gas mass injection at the base of the liquid-delivery tube. Two rates of injection were tested: one matching the momentum flux of the liquid, and the other having a mass flow three times as large as the first. The mass injected flow took the form of a jet projecting out of the base of the liquid-delivery tube which then blossomed into a mushroom-shaped structure similar to that seen in the liquid metal via high-speed movies of the atomization process.

Bibliography

- Anderson, I. E., Morton, H., and Figliola, R. S., 1989 “Fluid Flow Effects in Gas Atomization Processing,” *Physical Chemistry of Powder Metals: Production and Processing* (ed. W. M. Small), TMS, 229–249.
- Ando, T., Tsao, C., Wahlroos, J., and Grant, N. J., 1990 “Analysis and Control of Gas Atomization Rate,” *Int. J. of Powder Met.*, **26** (4), 311–318.
- Ayers, J. D., and Anderson, I. E., 1985 “Very Fine Metal Powders,” *J. of Metals*, **37** (8), 16–21.
- Baldwin, B. S., and Barth, T. J., 1990 “A One-Equation Turbulent Transport Model for High Reynolds Number Wall-Bounded Flows,” *NASA TM-102847*.
- Baldwin, B. S., and Lomax, H., 1978 “Thin Layer Approximation and Algebraic Model for Separated Turbulent Flows,” *AIAA Paper*, 78–257.
- Beam, R., and Warming, R. F., 1976 “An Implicit Finite Difference Algorithm for Hyperbolic Systems in Conservation Law Form,” *J. Comp. Phys.*, **22** (1), 87–110.
- Beddow, J. K., 1978 *The Production of Metal Powders by Atomization*, Heyden & Sons, Ltd.
- Boettinger, W. J., Bendersky, L., and Early, J. G., 1986 “An Analysis of the Microstructure of Rapidly Solidified Al-8 Wt. Pct. Fe Powder,” *Met. Trans. A*, **17** (1), 781–790.
- Brown, S. W., 1992 “A Shear Reversal Nozzle for Efficient Gas Atomization,” *Oak Ridge Y-12 Plant, Y-2460*.

- Cebeci, T., 1970 "Calculation of Compressible Turbulent Boundary-Layers with Heat and Mass Transfer," *AIAA Paper*, 70-741.
- Chien K.-Y., 1982 "Predictions of Channel and Boundary-Layer Flows with a Low-Reynolds-Number Turbulence Model," *AIAA J.*, **20** (1), 33-38.
- Conway, J. J., and Lizzi, P. E., 1993 "Improved Gas Atomization of Nickel-Base Super-alloys Through Computational Fluid Dynamics (CFD) Modeling," *P/M in Aerospace, Defense and Demanding Applications - 1993* (ed. F. H. Froes), MPIF, 93-100.
- Cooper, G. K., and Sirbaugh, J. R., 1989 "PARC Code: Theory and Usage," *Arnold Engineering Development Center, AEDC-TR-89-15*.
- Couper, M. J., and Singer, F., 1985 "Rapidly Solidified Aluminum Alloy Powder Produced by Optimization of the Gas Atomization Technique," *Rapidly Quenched Metals* (ed. S. Steeb and H. Warlimont), Amsterdam, Netherlands, 1737.
- Davies, C. B. and Venkatapathy, E., 1992 "Application of a Solution Adaptive Grid Scheme to Complex Three-Dimensional Flows," *AIAA J.*, **30** (9), 2227-2233.
- Durbin, P. A. and Speziale, C. G., 1991 "Local Anisotropy in Strained Turbulence at High Reynolds Numbers," *ASME J. Fluids Eng.*, **113** (4), 707-708.
- Erlebacher, G., Hussaini, M. Y., Kreiss, O., and Sarkar, S., 1990 "The Analysis and Simulation of Compressible Turbulence," *NASA CR-181997*.
- Espina, P. I., Ridder, S. D., Biancaniello, F. S., and Mattingly, G. E., 1989 "Aerodynamic Analysis of the Aspiration Phenomena in a Close-Coupled Inert Gas Atomizer", *Characterization & Diagnostics of Ceramics & Metal Particulate Processing* (ed. E. J. Lavernia, H. Henein, and I. Anderson), TMS, 49-62.

- Espina, P. I., Piomelli, U., and Mattingly, G. E., 1993 “A Numerical Investigation of the Compressible Flow Field Produced in an Annular Jet, Close-Coupled, Gas Metal Atomizer,” *Computational and Numerical Techniques in Powder Metallurgy* (ed. D. Madam, I. Anderson, W. Frazier, P. Kumar, and M. McKimpson), TMS, 41–53.
- Figliola, R. S., and Anderson, I. E., 1993 “Characterization of High Pressure Gas Atomization Flow Fields,” *Computational and Numerical Techniques in Powder Metallurgy* (ed. D. Madam, I. Anderson, W. Frazier, P. Kumar, and M. McKimpson), TMS, 29–39.
- Georgiadis, N. J., Chitsomboon, T., and Zhu, J., 1994 “Modification of the Two-Equation Turbulence Model on NPARC to a Chien Low Reynolds Number k - ϵ Formulation,” *NASA TM-106710*.
- Gorski, J. J., Chakravarthy, S. R., and Goldberg, U. C., 1985 “High Accuracy TVD Schemes for the k - ϵ Equations of Turbulence,” *AIAA Paper*, 85–1665.
- Grasso, F., and Falconi, D., 1993 “High-Speed Turbulence Modeling of Shock-Wave/Boundary-Layer Interaction,” *AIAA J.*, **31** (7), 1199–1206.
- Grasso, F., 1997 Private communication.
- Hanjalic, K., and Launder, B. E., 1976 “Contribution Towards a Reynolds-Stress Closure for Low-Reynolds-Number Turbulence,” *J. Fluid Mech.*, **74**, 593–610.
- Hariprasad, S., and Sastry, S. M. L., 1995 “Processing Maps for Optimizing Gas Atomization and Spray Deposition,” *JOM*, **47** (10), 56–59.
- Herrin, J. L., and Dutton, J. C., 1993 “An Experimental Investigation of Supersonic Axisymmetric Base Flows Including the Effects of Afterbody Boattailing,” *UIIU ENG 93-4018*, Dept. of Mechanical and Industrial Engineering, Univ. of Illinois at Urbana-Champaign, Urbana, IL.

- Herrin, J. L., and Dutton, J. C., 1994 “Supersonic Base Flow Experiments in the Near Wake of a Cylindrical Afterbody,” *AIAA J.*, **32** (1), 77–83.
- Herrin, J. L., 1995, Private communication.
- Hirsch, C., 1990 *Numerical Computation of Internal and External Flows, Vol. 2: Computational Methods for Inviscid and Viscous Flows*, John Wiley & Sons.
- Jameson, A., Schmidt, W., and Turkel, E., 1981 “Numerical Solutions of the Euler Equations by Finite Volume Methods Using Runge-Kutta Time-Stepping Schemes,” *AIAA Paper*, 81–1259.
- John, J. E. A., 1984 *Gas Dynamics*, 2nd edition, Allyn and Bacon, Inc.
- Jones, W. P., and Launder, B. E., 1972 “The Prediction of Laminarization with a 2-Equation Model of Turbulence,” *Int. J. of Heat and Mass Transfer*, **15**, 301–314.
- Kuntz, D. W., and Payne, J. L., 1995 “Simulation of Powder Metal Fabrication with High Pressure Gas Atomization,” *Advances in Powder Metallurgy and Particulate Materials, Part 1: Powder Production and Characterization* (ed. M. Phillips and J. Porter), MPIF, 63–78.
- Lawley, A., 1985 “Powder Metallurgy and Rapid Solidification – Compelling Technologies,” *JOM*, **37** (8), 15.
- Lilienthal, P. F., Brink, D. F., and Addy, A. L., 1970 “Experimental Program for the Study of Supersonic and Transonic Axisymmetric Base-Pressure Problems,” Dept. of Mech. and Ind. Eng., Univ. of Illinois at Urbana-Champaign, Urbana, IL.
- Liu, H., Lavernia, E. J., Rangel, R. H., 1995 “An Analysis of Freeze-Up Phenomena During Gas Atomization of Metals,” *Int. J. of Heat and Mass Transfer*, **38** (12), 2183–2193.

- Liu, H., and Dandy, D. S., 1995 “Modeling of Liquid Metal Flow and Heat Transfer in Delivery Tube During Gas Atomization,” *Mat. Sci. Eng.*, **A197** (2), 199–208.
- Mates, S. P., and Settles, G. S., 1995 “A Flow Visualization Study of the Gas Dynamics of Liquid Metal Atomization Nozzles,” *Advances in Powder Metallurgy and Particulate Materials, Part 1: Powder Production and Characterization* (ed. M. Phillips and J. Porter), MPIF, 15–29.
- Mates, S. P., and Settles, G. S., 1996 “High-Speed Imaging of Liquid Metal Atomization by Two Different Close-Coupled Nozzles,” *Advances in Powder Metallurgy and Particulate Materials, Part 1: Atomization* (ed. T. Kadel and K. S. Narasimhan), MPIF, 67–80.
- Mi, J., Figliola, R. S., Anderson, I. E., 1996 “A Numerical Simulation of Gas Flow Field Effects on High Pressure Gas Atomization Due to Operating Pressure Variation,” *Mat. Sci. Eng.*, **A208** (1), 20–29.
- Mikhail, A. G., Hankey, W. L., and Shang, J. S., 1980 “Computation of a Supersonic Flow Past an Axisymmetric Nozzle Boattail with Jet Exhaust,” *AIAA J.*, **18** (8), 869–875.
- Miller, R. S., Miller, S. A., Savkar, S. D., and Mourer, D. P., 1996 “Two Phase Flow Model for the Close-Coupled Atomization of Metals,” *Int. J. of Powder Met.*, **32** (4), 341–352.
- Mueller, T. J., 1968 “Determination of the Turbulent Base Pressure in Supersonic Axisymmetric Flow,” *J. of Spacecraft and Rockets*, **5**, (1), 101–107.
- Mueller, T. J., 1985 “The Role of Flow Visualization in the Study of Afterbody and Base Flows: A Review,” *Experiments in Fluids*, **3**, 61–70.
- Nakahashi, K., and Deiwert, G. S., 1985 “A Self-Adaptive-Grid Method with Application to Airfoil Flow,” *AIAA Paper*, 85-1525.

- Nichols, R. H., 1990 "A Two-Equation Model for Compressible Flows," *AIAA Paper*, 90-0494.
- Pankhurst, R. C., and Holder, D. W., 1952 *Wind-Tunnel Technique*, Sir Isaac Pitman & Sons, Ltd., London, 105-112.
- Peace, A. J., 1991 "Turbulent Flow Predictions for Afterbody/Nozzle Geometries Including Base Effects," *J. of Propulsion and Power*, **7** (3), 396-403.
- Piomelli, U., 1992 "Numerical Solution of the Viscous Flow in an Atomization Die," *NIST/Industrial Consortium on Intelligent Processing of Rapidly Solidified Metal Powders by Inert Gas Atomization, First Annual Report, March 1, 1991 to February 29, 1992*, 15-25.
- Pulliam, T. H., and Steger, J. L., 1980 "Implicit Finite-Difference Simulation of Three-Dimensional Compressible Flows," *AIAA J.*, **18** (2), 159-167.
- Pulliam, T. H., and Chaussee, D. S., 1981 "A Diagonal Form of an Implicit Approximate Factorization Algorithm," *J. Comp. Phys.* **39**, 347-363.
- Pulliam, T. H. , 1984 "Euler and Thin Layer Navier-Stokes Codes: ARC2D, ARC3D," *Notes for Computational Fluid Dynamics User's Workshop, University of Tennessee Space Institute, Tullahoma, TN, UTSI Publication E02-4005-023-84*, 15.1-15.85.
- Ridder, S. D., and Biancaniello, F. S., 1988 "Process Control During High Pressure Atomization," *Mat. Sci. Eng.*, **98**, 47-51.
- Ridder, S. D., Osella, S. A., Espina, P. I., and Biancaniello, F. S., 1992 "Intelligent Control of Particle Size Distribution During Gas Atomization," *Int. J. of Powder Met.*, **28** (2), 133-138.
- Sahu, J., Nietubicz, C. J., and Steger, J. L., 1985 "Navier-Stokes Computations of Projectile Base Flow with and without Mass Injection," *AIAA J.*, **23** (9), 1348-1355.

- Sahu, J., and Danberg, J. E., 1986 “Navier-Stokes Computations of Transonic Flows with a Two-Equation Turbulence Model,” *AIAA J.*, **24** (11), 1744–1751.
- Sahu, J., 1989 “Three-Dimensional Base-Flow Calculation for a Projectile at Transonic Velocity,” *AIAA J.*, **27** (2), 138–139.
- Sahu, J., 1994 “Numerical Computations of Supersonic Base Flow With Special Emphasis on Turbulence Modeling,” *AIAA J.*, **32** (7), 1547–1549.
- Sarkar, S., and Balakrishnan, L., 1991 “Application of a Reynolds Stress Turbulence Model to the Compressible Shear Layer,” *AIAA J.*, **29** (5), 743–749.
- Sarkar, S., Erlebacher, G., Hussaini, M. Y., and Kreiss, H. O., 1991 “The Analysis and Modelling of Dilatation Terms in Compressible Turbulence,” *J. Fluid Mech.*, **227**, 473–493.
- Sarkar, S., 1992 “The Pressure-Dilatation Correlation in Compressible Flows,” *Phys. Fluids A*, 4 (12), 2674–2682.
- Sauter, J. M. and Dutton, J. C., 1989 “Design of an Axisymmetric Supersonic Wind Tunnel and Experimental Study of Supersonic, Power-Off Base Flow Phenomena,” *UILU ENG 89-4002*, Dept. of Mech. and Ind. Eng., Univ. of Illinois at Urbana-Champaign, Urbana, IL.
- Sirbaugh, J. R., Cooper, G. K., Smith, C. F., Jones, R. R., Towne, C. E., and Power, G. D., 1994 “A User’s Guide to NPARC, Version 2.0,” *The NPARC Alliance, NASA/AEDC*.
- Spalart, P. R., 1988 “Direct Simulation of a Turbulent Boundary Layer up to $Re_\theta = 1410$,” *J. Fluid Mech.*, **187**, 61–98.
- Spalding, D. B., 1967 “Heat Transfer from Turbulent Separated Flows,” *J. Fluid Mech.*, **27**, (1), 97–109.

- Speziale, C. G., and Sarkar, S., 1989 “A Preliminary Compressible Second-Order Closure Model for High Speed Flows,” *NASA CR-181875*.
- Speziale, C. G., Abid, R., and Anderson, E. C., 1992 “Critical Evaluation of Two-Equation Models for Near Wall Turbulence,” *AIAA J.*, **30** (2), 324–331.
- Sule, W. P., and Mueller, T. J., 1973 “Annular Truncated Plug Nozzle Flowfield and Base Pressure Characteristics,” *J. of Spacecraft and Rockets*, **10** (11), 689–695.
- Sun, C. C., and Childs, M. E., 1973 “A Modified Wall Wake Velocity Profile for Turbulent Compressible Boundary Layers,” *J. of Aircraft*, **10** (6), 381–383.
- Ting, E. Y., and Grant, N. J., 1986 “Metal Powder Production by Gas Atomization,” *Progress in Powder Metallurgy, MPIF*, **41**, 67–86.
- Tucker, P. K., and Shyy, W., 1993 “A Numerical Analysis of Supersonic Flow Over an Axisymmetric Afterbody,” *AIAA Paper 93-2347*.
- Ünal, A., 1989 “Gas Flow in Atomization Nozzles,” *Physical Chemistry of Powder Metals: Production and Processing* (ed. W. M. Small), TMS, 201–228.
- Vandromme, D., 1983 “Contribution à la Modelisation et la Prediction d’Ecoulements Turbulents a masse Volumique Variable,” Doctoral Dissertation, Université des Science et Techniques de Lille, Lille, France.
- White, F. M., 1991 *Viscous Fluid Flow*, 2nd edition, McGraw-Hill, Inc.
- Wilcox, D. C., 1991 “Progress in Hypersonic Turbulence Modeling,” *AIAA Paper*, 91-1795.
- Yakhot, V., Orszag, S. A., Thangam, S., Gatski, T. B., and Speziale, C. G. 1992 “Development of turbulence models for shear flows by a double expansion technique,” *Phys. Fluids A*, **4** (7), 1510–1520.
- Zeman, O., 1990 “Dilatation Dissipation: The Concept and Application in Modeling Compressible Mixing Layer,” *Phys. Fluids A*, **2** (2), 178–188.

CURRICULUM VITAE

Name: Pedro Iván Espina.

Permanent address: 10302 Royal Woods Ct., Gaithersbug, MD 20879.

Degree and date to be conferred: Ph.D., 1997.

Date of birth: October 29, 1964.

Place of birth: San Juan, Puerto Rico.

Secondary education: Colegio Nuestra Señora de la Merced, Hato Rey, Puerto Rico, May 1992.

Collegiate institutions attended:

<u>Institution</u>	<u>Dates Attended</u>	<u>Degree</u>	<u>Date of Degree</u>
Univ. of Puerto Rico, Mayagüez Campus Major: Mechanical Engineering	Aug., 1982, to May, 1987	B.S.	May, 1988
Univ. of Maryland, College Park Campus Major: Mechanical Engineering	Sept., 1987, to Dec., 1991	M.S.	Dec., 1991
Univ. of Maryland, College Park Campus Major: Mechanical Engineering	Jan., 1991, to Dec., 1997	Ph.D.	Dec., 1997

Professional Publications:

Biancaniello, F. S., Espina, P. I., Mattingly, G. E., and Ridder, S. D., 1989 "A Flow Visualization Study of Supersonic Inert Gas Metal Atomization," *Mat. Sci. Eng.*, **A119**, 159–166.

- Espina, P. I., Ridder, S. D., Biancaniello, F. S., and Mattingly, G. E., 1989 "Aerodynamic Analysis of the Aspiration Phenomena in a Close-Coupled Inert Gas Atomizer," *Characterization & Diagnostics of Ceramics & Metal Particulate Processing* (ed. E. J. Lavernia, H. Henein, and I. Anderson), TMS, 49–62.
- Ridder, S. D., Biancaniello, F. S., Espina, P. I., and Miller, S. A., 1989 "Laser Holographic Imaging of the Two Fluid Atomization Process," *Characterization & Diagnostics of Ceramics & Metal Particulate Processing* (ed. E. J. Lavernia, H. Henein, and I. Anderson), TMS, 73–86.
- Ridder, S. D., Espina, P. I., and Biancaniello, F. S., 1989 "Optimization of Inert Gas Atomization," *Physical Chemistry of Powder Metals Production and Processing* (ed. W. M. Small), TMS, 163–173.
- Biancaniello, F. S., Conway, J. J., Espina, P. I., Mattingly, G. E., and Ridder, S. D., 1990 "Particle Size Measurement of Inert Gas Atomized Powder," *Mat. Sci. Eng.*, **A124**, 9–14.
- Ridder, S. D., Osella, S. A., Espina, P. I., and Biancaniello, F. S., 1990 "Process Diagnostics, Modeling, and Control for Inert Gas Atomization," *Intelligent Processing of Materials* (ed. H. N. G. Wadley and W. E. Eckhart, Jr.), TMS, 41–53.
- Ridder, S. D., Osella, S. A., Espina, P. I., and Biancaniello, F. S., 1990 "Development of Adaptive Control Strategies For Inert Gas Atomization," *Intelligent Processing of Materials* (ed. H. P. Wang), ASME, 79–88.
- Osella, S. A., Ridder, S. D., Biancaniello, F. S., and Espina, P. I., 1991 "The Intelligent Control of an Inert Gas Atomization Process," *JOM*, **43**, 18–21.
- Ridder, S. D., Osella, S. A., Espina, P. I., and Biancaniello, F. S., 1991 "Advanced Sensors and Process Control for Gas Atomization," *Advances in Powder Metallurgy - 1991, Vol. 5, P/M Materials* (ed. L. F. Pease and R. J. Sansoucy), MPIF, 249–262.
- Espina, P. I., 1991 "An Investigation of the Compressible Flow in a Supersonic Inert Gas Metal Atomizer," *M.S. Thesis*, Univ. of Maryland, College Park, MD.
- Ridder, S. D., Osella, S. A., Espina, P. I., and Biancaniello, F. S., 1992 "Process Modeling and Control of Inert Gas Atomization," *Thermal Structures and Materials for High-Speed Flight, Vol. 140, Progress in Astronautics and Aeronautics* (ed. E. A. Thornton), AIAA, 499–521.
- Ridder, S. D., Osella, S. A., Espina, P. I., and Biancaniello, F. S., 1992 "Intelligent Control of Particle Size Distribution During Gas Atomization," *Inter. J. of Powder Met.*, **28**, 2, 133–147.

- Espina, P. I., Piomelli, U., and Mattingly, G. E., 1993 "A Numerical Investigation of the Compressible Flow Field Produced in an Annular Jet, Close-Coupled, Gas Metal Atomizer," *Computational and Numerical Techniques in Powder Metallurgy* (ed. D. S. Madan, I. E. Anderson, and W. E. Frazier) TMS, 41–53.
- Espina, P. I., Osella, S. A., Ridder, S. D., Biancaniello, F. S., and Mattingly, G. E., 1993 "The Evolution of Gas-Metal Atomization: From Discrete Jets to Annular Jets via Computational Fluid Mechanics," *P/M in Aerospace, Defense and Demanding Applications* (ed. F. H. Froes), MPIF, 101–107.
- Espina, P. I., Osella, S. A., Ridder, S. D., Biancaniello, F. S., and Mattingly, G. E., 1994 "A Hybrid Model of a Gas-Metal Atomizer and its Application to the Development of a Knowledge-Based Control System," *Proceedings of the 1994 Powder Metallurgy World Congress and Exhibition, PM'94, Vol. I* (ed. D. François), SF2M/EPMA, 349–352.
- Osella, S. A., Espina, P. I., Ridder, S. D., Biancaniello, F. S., and Mattingly, G. E., 1994 "Correlation of the Particle Size Distribution with Process Parameters for a Gas-Metal Atomizer," *Proceedings of the 1994 Powder Metallurgy World Congress and Exhibition, PM'94, Vol. I* (ed. D. François), SF2M/EPMA, 391–394.
- Espina, P. I., and Piomelli, U., 1997 "A Validation of the NPARC Code in Supersonic Base Flows," *AIAA Paper*, 97–0032.
- Wright, J. D., and Espina, P. I., 1997 "Flowmeter Calibration Facility for Heated Gas Mixtures," *to be presented at the 1997 NCSL Conference*, (Atlanta, GA, July, 1997).

Professional positions held:

Mechanical Engineer, Fluid Flow Group, National Institute of Standards and Technology, Gaithersburg, MD, 20899.